論文 / 著書情報
Article / Book Information

題目(和文)	制約付き凸最適化による ロバストな画像復元・合成に関する研究
Title(English)	A study of robust image restoration and fusion via constrained convex optimization
著者(和文)	武山彩織
Author(English)	Saori Takeyama
出典(和文)	学位:博士（工学）, 学位授与機関:東京工業大学, 報告番号:甲第11939号, 授与年月日:2021年3月26日, 学位の種別:課程博士, 審査員:熊澤 逸夫,小野 峻佑,山口 雅浩,山田 功,篠﨑 隆宏
Citation(English)	Degree:Doctor (Engineering), Conferring organization: Tokyo Institute of Technology, Report number:甲第11939号, Conferred date:2021/3/26, Degree Type:Course doctor, Examiner:,,,,
学位種別(和文)	博士論文
Type(English)	Doctoral Thesis

Tokyo Institute of Technology
School of Engineering
Department of Information and Communications Engineering

PhD thesis

A study of robust image restoration and fusion via constrained convex optimization

Supervisor Professor Itsuo Kumazawa
Co-supervisor Associate Professor Shunsuke Ono

January, 2021.

Department Information and Communications Engineering
Name Saori Takeyama

Contents

List of Figures

List of Tables

Chapter 1

Introduction

1.1 Background

Images are affected by some degradations and noises through an observation process, e.g., blur, down-sampling, and missing pixel. The noises are caused by an electric current, heat, imaging device, and so on, and capturing a noiseless image would be impossible. Therefore, image restoration is a key technique and actively studied such as denoising, deblurring, super-resolution, and compressed sensing (CS) reconstruction. Since the restoration problems assume various degradations and noises, they require a robust image restoration method.

Most image restoration methods are established based on optimization: a desirable image is characterized as a solution to some optimization problem, which consists of a regularization term and a data-fidelity term. The regularization term evaluates apriori knowledge about underlying properties on images, and the data-fidelity term keeps the consistency with a given observation. Thanks to the design, these methods get a reasonable result under ill-posed or ill-conditioned scenarios typical in image restoration. However, since the methods are not enough robust for degradations or noises, the results have over-smoothing or artifacts. This is caused by (i) not enough utilizing apriori knowledge on an image, (ii) not full consideration of outlier and modeling error.

Recently, high-resolution images, especially spatial one, is required by many application. The resolution of images depends on a sensor in an imaging device, and they have a trade-off between spatial and spectral resolution. Therefore, estimating higher-resolution images from observation is an essential task. Besides, since blur removes edge and detail information in an image, it is limited to restore an edge-preserving image from an only blur image. For these degradations, one effective approach is using a guide image that has a different characteristic. This technique is named image fusion and helps to robust estimation.

Based on the above discussion, we propose novel robust image restoration techniques via constrained convex optimization. Specifically, we propose a new regularization that effectively utilizes apriori knowledge on an image. The proposed regularization function evaluates two types of piecewise-smoothness on images, so it helps high-quality restoration. Then, for some image restoration and fusion problems, we formulate each con-

strained convex optimization problem considering the sparsity of outlier. The problem evaluates data-fidelity between an observation and a restored image by hard constraints, so one can set the hyperparameters with comparative ease. Finally, we solve the restoration problem by iterative proximal splitting methods. In the experiments, we demonstrate the performance of the proposed methods compared with existing methods for four image restoration and fusion problems: denoising, CS reconstruction, blur and noisy image fusion, and super-resolution.

1.2 Organization of this paper

The remainder of the paper is organized as follows.

Chapter 1 research background and the aim

Chapter 2 notation and mathematical ingredients

Chapter 3 robust image restoration methods for HS image denoising and CS reconstruction

Chapter 4 robust image fusion methods for blur and noisy image fusion and super-resolution

Chapter 5 conclusion of the paper

Chapter 2

Preliminaries

In this paper, let $\mathbb{R}$ be the set of real numbers. We shall use boldface lowercase and capital to represent vectors and matrices, respectively, and $:=$ to define something. We denote the transpose of a vector/matrix by $(\cdot)^\top$, and the Euclidean norm (the ℓ_2 norm) of a vector by $\|\cdot\|$. For notational convenience, we treat an image $\boldsymbol{\mathcal{U}} \in \mathbb{R}^{N_v \times N_h \times B}$ as a vector $\mathbf{u} \in \mathbb{R}^{NB}$ ($N := N_v N_h$ is the number of the pixels of each band, and B is the number of the bands) by stacking its columns on top of one another, i.e., the index of the component of the ith pixel in kth band is $i+(k-1)N$ (for $i = 1, \ldots, N$ and $k = 1, \ldots, B$).

In Tab. 2.1, we show the correspondence between the abbreviations used in this paper.

2.1 Proximal Tools

A function $f : \mathbb{R}^L \to (-\infty, \infty]$ is called *proper lower semicontinuous convex* if $\mathrm{dom}(f) := \{\mathbf{x} \in \mathbb{R}^L |\ f(\mathbf{x}) < \infty\} \neq \emptyset$, $\mathrm{lev}_{\leq \alpha}(f) := \{\mathbf{x} \in \mathbb{R}^L |\ f(\mathbf{x}) \leq \alpha\}$ is closed for every $\alpha \in \mathbb{R}$, and $f(\lambda \mathbf{x} + (1-\lambda)\mathbf{y}) \leq \lambda f(\mathbf{x}) + (1-\lambda) f(\mathbf{y})$ for every $\mathbf{x}, \mathbf{y} \in \mathbb{R}^L$ and $\lambda \in (0, 1)$, respectively. Let $\Gamma_0(\mathbb{R}^L)$ be the set of all proper lower semicontinuous convex functions on $\mathbb{R}^L$.

The proximity operator [16] plays a central role in convex optimization based on proximal splitting. The proximity operator of $f \in \Gamma_0(\mathbb{R}^L)$ with an index $\gamma > 0$ is defined by

$$\mathrm{prox}_{\gamma f}(\mathbf{x}) := \operatorname*{argmin}_{\mathbf{y}} f(\mathbf{y}) + \frac{1}{2\gamma}\|\mathbf{y} - \mathbf{x}\|^2.$$

We introduce the indicator function of a nonempty closed convex set $C \subset \mathbb{R}^L$, which is defined as follows:

$$\iota_C(\mathbf{x}) := \begin{cases} 0, & \text{if } \mathbf{x} \in C, \\ \infty, & \text{otherwise.} \end{cases}$$

Then, for any $\gamma > 0$, its proximity operator is given by

$$\mathrm{prox}_{\gamma \iota_C}(\mathbf{x}) = P_C(\mathbf{x}) := \operatorname*{argmin}_{\mathbf{y} \in C} \|\mathbf{x} - \mathbf{y}\|, \tag{2.1}$$

Table 2.1: Correspondence table between the abbreviations

abbreviations	formal name
ADMM	alternating direction method of multipliers
ASSTV	anisotropic spatio-spectral total variation
BCCB	block-circulant-with-circulant-blocks
CC	cross correlation
CHPAN	compressed hyperspectral pansharpening
CNMF	coupled non-negative matrix factorization
CS	compressed sensing
ERGAS	erreur relative globale adimensionnelle de synthèse
GFPCA	guided filter principal component analysis
GS	gram schmidt
GSA	gram schmidt adoptive
HR-HS image	hyperspectral image of high spatial and spectral resolution
HS	hyperspectral
HSSTV	hybrid spatio-spectral total variation
HTV	hyperspectral total variation
HySure	hyperspectral Stein's unbiased risk estimator
LLRGTV	local low-rank matrix recovery and global spatial-spectral total variation
LNWTV	local spatial neighborhood weighted spectral-spatial hyperspectral total variation
LR-HS image	hyperspectral image of high spectral resolution but low spatial resolution
LRM	low rank modeling
LRMR	low-rank matrix recovery
LRTV	total variation-regularized low-rank matrix factorization
MS	multispectral
MTF-GLP	modulation transfer function-generalized Laplacian pyramid
MTF-GLP-HPM	modulation transfer function-generalized Laplacian pyramid with high pass modulation
NRMSE	normalized root mean squared error
PAN	panchromatic
PCA	principal component analysis
PSNR	peak signal-to-noise ratio
RMSE	the root mean squared error
SAM	the spectral angle mapper
SFIM	smoothing filter-based intensity modulation
SSAHTV	spectral-spatial adaptive hyperspectral total variation
SSIM	signal similarity
SSTV	spatio-spectral total variation
TV	total variation

where $P_C(\mathbf{x})$ is the metric projection onto C.

In this paper, we use proximity operators of multiple functions, and we introduce them here. The proximity operators of the ℓ_1 norm and the mixed $\ell_{1,2}$ norm are reduced to simple soft-thresholding type operations: for $\gamma > 0$ and for $i = 1, \ldots, 4NB$, (i) in the case of the ℓ_1 norm,

$$[\mathrm{prox}_{\gamma\|\cdot\|_1}(\mathbf{x})]_i = \mathrm{sgn}(x_i) \max\{|x_i| - \gamma, 0\}, \tag{2.2}$$

where sgn is the sign function, and (ii) in the case of the mixed $\ell_{1,2}$ norm,

$$[\mathrm{prox}_{\gamma\|\cdot\|_{1,2}}(\mathbf{x})]_i = \max\left\{1 - \gamma \left(\sum_{j=0}^{3} x_{\tilde{i}+jNB}^2\right)^{-\frac{1}{2}}, 0\right\} x_i, \tag{2.3}$$

where $\tilde{i} := ((i-1) \mod NB) + 1$.

The proximity operators of the indicator functions of $\mathcal{B}^{\mathbf{v}}_{2,\varepsilon} := \{\mathbf{x} \in \mathbb{R}^{NB} | \|\mathbf{x} - \mathbf{v}\| \leq \varepsilon\}$, $\mathcal{B}_{1,\eta} := \{\mathbf{x} \in \mathbb{R}^{NB} | \|\mathbf{x}\|_1 \leq \eta\}$, and $[\underline{\mu}, \overline{\mu}]^{NB}$. Here, $\mathcal{B}^{\mathbf{v}}_{2,\varepsilon}$ is the $\mathbf{v}$-centered ℓ_2-ball with the radius ε, and $\mathcal{B}_{1,\eta}$ is the $\mathbf{0}$-centered ℓ_1-ball with the radius η. In (2.1), the proximity operator of the indicator functions equate the metric projections onto them. Specifically, the metric projection to $\mathcal{B}^{\mathbf{v}}_{2,\varepsilon}$ is given by

$$P_{\mathcal{B}^{\mathbf{v}}_{2,\varepsilon}}(\mathbf{x}) = \begin{cases} \mathbf{x}, & \text{if } \mathbf{x} \in \mathcal{B}^{\mathbf{v}}_{2,\varepsilon}, \\ \mathbf{v} + \frac{\varepsilon(\mathbf{x}-\mathbf{v})}{\|\mathbf{x}-\mathbf{v}\|}, & \text{otherwise}, \end{cases} \tag{2.4}$$

that onto $\mathcal{B}_{1,\eta}$ is given by

$$P_{\mathcal{B}_{1,\eta}} = \mathrm{sgn}(\mathbf{x}) \max(|\mathbf{x}| - \eta, 0), \tag{2.5}$$

and that onto $[\underline{\mu}, \overline{\mu}]^{NB}$ is given, for $i = 1, \ldots, NB$, by

$$[P_{[\underline{\mu},\overline{\mu}]^{NB}}(\mathbf{x})]_i = \min\{\max\{x_i, \underline{\mu}\}, \overline{\mu}\}. \tag{2.6}$$

2.2 ADMM

ADMM [1–4] is a popular proximal splitting method, and it can solve convex optimization problems of the form:

$$\min_{\mathbf{x},\mathbf{z}} f(\mathbf{x}) + g(\mathbf{z}) \text{ s.t. } \mathbf{z} = \mathbf{G}\mathbf{x}, \tag{2.7}$$

where $f \in \Gamma_0(\mathbb{R}^{L_1})$, $g \in \Gamma_0(\mathbb{R}^{L_2})$, and $\mathbf{G} \in \mathbb{R}^{L_2 \times L_1}$. Here, we assume that f is quadratic, g is *proximable*, i.e., the proximity operator of g is computable in an efficient manner, and $\mathbf{G}$ is a full-column rank matrix. For arbitrarily chosen $\mathbf{z}^{(0)}, \mathbf{d}^{(0)}$ and a step size $\gamma > 0$, ADMM iterates the following steps:

$$\begin{cases} \mathbf{x}^{(n+1)} = \underset{\mathbf{x}}{\mathrm{argmin}}\, f(\mathbf{x}) + \frac{1}{2\gamma}\|\mathbf{z}^{(n)} - \mathbf{G}\mathbf{x} - \mathbf{d}^{(n)}\|^2, \\ \mathbf{z}^{(n+1)} = \mathrm{prox}_{\gamma g}(\mathbf{G}\mathbf{x}^{(n+1)} + \mathbf{d}^{(n)}), \\ \mathbf{d}^{(n+1)} = \mathbf{d}^{(n)} + \mathbf{G}\mathbf{x}^{(n+1)} - \mathbf{z}^{(n+1)}, \end{cases} \tag{2.8}$$

The convergence property of ADMM is given as follows.

Theorem 1 (Convergence of ADMM [3]). *Consider Prob.* (2.7)*, and assume that* $\mathbf{G}^\top\mathbf{G}$ *is invertible and that a saddle point of its unaugmented Lagrangian* $\mathcal{L}_0(\mathbf{x},\mathbf{z},\mathbf{y}) := f(\mathbf{x}) + g(\mathbf{z}) - \langle \mathbf{d}, \mathbf{G}\mathbf{x}-\mathbf{z}\rangle$ *exists. A triplet* $(\hat{\mathbf{x}},\hat{\mathbf{z}},\hat{\mathbf{d}})$ *is a saddle point of an unaugmented Lagrangian* $\mathcal{L}_0$ *if and only if* $\mathcal{L}_0(\hat{\mathbf{x}},\hat{\mathbf{z}},\mathbf{d}) \le \mathcal{L}_0(\hat{\mathbf{x}},\hat{\mathbf{z}},\hat{\mathbf{d}}) \le \mathcal{L}_0(\mathbf{x},\mathbf{z},\hat{\mathbf{d}})$*, for any* $(\mathbf{x},\mathbf{z},\mathbf{d}) \in \mathbb{R}^{L_1}\times\mathbb{R}^{L_2}\times\mathbb{R}^{L_2}$*. Then the sequence* $(\mathbf{x}_n)_{n>0}$ *generated by* (2.8) *converges to an optimal solution to Prob.* (2.7)*.*

2.3 Primal-Dual Splitting Method

A primal-dual splitting method [17] is a popular splitting method like ADMM, and it can solve convex optimization problems of the form:

$$\min_{\mathbf{x}} g(\mathbf{x}) + h(\mathbf{L}\mathbf{x}) \tag{2.9}$$

where, $g \in \Gamma_0(\mathbb{R}^{L_1})$ and $h \in \Gamma_0(\mathbb{R}^{L_2}$ are *proximable* functions, and $\mathbf{L} \in \mathbb{R}^{L_2\times L_1}$ is a linear operator. For arbitrarily chosen $\mathbf{y}^{(0)}$ and step sizes $\gamma_1, \gamma_2 > 0$, the primal-dual splitting method iterates the following steps:

$$\left\lfloor \begin{array}{l} \mathbf{x}^{(n+1)} := \mathrm{prox}_{\gamma_1 g}(\mathbf{x}^{(n)} - \gamma_1(\mathbf{x}^{(n)} + \mathbf{L}^\top\mathbf{y}^{(n)})), \\ \mathbf{y}^{(n+1)} := \mathrm{prox}_{\gamma_2 h^*}(\mathbf{y}^{(n)} + \gamma_2\mathbf{L}(2\mathbf{x}^{(n+1)} - \mathbf{x}^{(n)})). \end{array} \right. \tag{2.10}$$

Here, h^* is the convex conjugate function of h, and the proximity operator can be computed, in [18, Theorem 14.3 (ii)] as follows:

$$\mathrm{prox}_{\gamma h^*}(\mathbf{x}) = \mathbf{x} - \gamma\,\mathrm{prox}_{\frac{1}{\gamma}h}\left(\frac{\mathbf{x}}{\gamma}\right). \tag{2.11}$$

For the convergence of (2.10), the step sizes γ_1 and γ_2 satisfy $\gamma_1\gamma_2\|\mathbf{L}\|_{op}^2 \le 1$, where $\|\cdot\|_{op}$ is the operator norm.

Chapter 3

Image Restoration

3.1 Hyperspectral Image Denoising

A hyperspectral (HS) image has 1D spectral information, including invisible light and narrow wavelength interval, in addition to 2D spatial information and thus can visualize unseen intrinsic characteristics of scene objects and environmental lighting. This makes HS imaging a key technique in many applications in various fields, e.g., earth observation, agriculture, and medical and biological imaging [19–21]. Observed HS images are often affected by noise because of the small amount of light in narrow wavelength and/or sensor failure. Thus, we need some robust methods for restoring desirable HS images from such degraded observations.

Most HS image restoration methods are based on optimization, which consists of a regularization term and a data-fidelity term. The regularization term evaluates apriori knowledge on HS images, and plays an essential role for robust HS image restoration. Regularization techniques for HS image restoration are roughly classified into two groups: total variation (TV)-based approach and low-rank modeling (LRM)-based one. TV models the total absolute magnitude of local differences to exploit the piecewise-smooth structures of an image. Many TV-based approaches [6,7,9,22] have been proposed for HS image restoration. Besides, LRM-based approaches [5,23] exploit the underlying low-rank structure in the spectral direction of an HS image. A popular example is the so-called Low-rank matrix recovery (LRMR) [5].

Many recent methods [9, 12, 13, 24–32] combine TV-based and LRM-based approaches, and in general, they perform better than approaches using either regularization. This is because TV-based approaches model the spatial structure of an HS image, whereas LRM-based approaches the spectral one. Naturally, the methods have to handle multiple regularization terms and a data-fidelity term(s) simultaneously in one objective function. So the methods must carefully control the hyperparameter(s) balancing these terms. Specifically, such hyperparameters are *interdependent*, which means that a suitable value of a hyperparameter varies depending on the multiple regularization terms used and the noise intensities on a given observation. Hence, the hyperparameter settings in such combined approaches are often troublesome tasks. Tab. 3.1 summarizes the features of the methods reviewed in this section.

Table 3.1: The feature of existing methods for HS image restoration.

Methods \ Feature	Spatial Correlation	Spectral Correlation	Convexity	Hyperparameters
HTV [6]	◯	×	**convex**	interdependent
SSAHTV [6]	◯	△	**convex**	interdependent
SSTV [7]	△	◯	**convex**	interdependent
ASSTV [22]	◯	◯	**convex**	interdependent
LRM [5, 23]	×	◯	nonconvex	**independent**
LNWTV + LRM [9, 24]	◯	◯	**convex**	interdependent
HTV + LRM [12]	◯	◯	nonconvex	interdependent
HTV + LRM [25, 26]	◯	◯	**convex**	interdependent
ASSTV + LRM [27, 32]	◯	◯	nonconvex	interdependent
SSTV + LRM [13, 28, 29]	◯	◯	**convex**	interdependent
SSTV + LRM [30, 31]	◯	◯	nonconvex	interdependent
proposed	◯	◯	**convex**	**independent**

Based on the above discussion, we propose a new constrained convex optimization approach to HS image restoration. Our proposed method restores a desirable HS image by solving a convex optimization problem involving a new TV-based regularization and hard constraints on data-fidelity. The regularization, named Hybrid Spatio-Spectral Total Variation (HSSTV), is designed to evaluate two types of local differences: direct local spatial differences and local spatio-spectral differences in a unified manner to effectively exploit both the underlying spatial and spectral structures of an HS image. Thanks to this design, HSSTV has a strong noise and artifact removal ability while avoiding oversmoothing and spectral distortion without combining LRM. Moreover, the constrained-type data-fidelity in the proposed method enables us to translate interdependent hyperparameters to the upper bounds of the degree of data-fidelity that can be determined based only on the noise intensity. As a result, the proposed method has no interdependent hyperparameter. We also develop an efficient algorithm for solving the optimization problem based on the well-known alternating direction method of multipliers (ADMM) [1, 3, 4].

3.1.1 Related Works

We elaborate on existing HS image denoising methods based on optimization.

TV-Based Methods

The methods proposed in [6, 7, 22] restore a desirable HS image by solving a convex optimization problem involving TV-based regularization. Let $\bar{\mathbf{u}} \in \mathbb{R}^{NB}$ be the desirable HS image, and the authors assume that an observation $\mathbf{v} \in \mathbb{R}^{NB}$ is modeled as follows:

$$\mathbf{v} = \bar{\mathbf{u}} + \mathbf{s} + \mathbf{n},$$

where $\mathbf{n}$ and $\mathbf{s}$ are an additive white Gaussian noise and a sparse noise, respectively. Here, the sparse noise corrupts only a few pixels in the HS image but heavily, e.g., impulse noise,

salt-and-pepper noise, and line noise. The observation and the restoration problem of the methods are given by the following forms:

$$\min_{\mathbf{u},\mathbf{s}} \|\mathbf{v}-\mathbf{u}-\mathbf{s}\|^2 + \lambda_1 \mathcal{R}_{\mathrm{TV}}(\mathbf{u}) + \lambda_2 \|\mathbf{s}\|_1, \tag{3.1}$$

where $\mathcal{R}_{\mathrm{TV}}$ is a regularization function based on TV, and λ_1 and λ_2 are hyperparameters. Here, The first and third terms evaluate data-fidelity on Gaussian and sparse noise, respectively. The hyperparameters λ_1 and λ_2 represent the priorities of each term. If we can choose suitable values of the hyperparameters, then this formulation yields high-quality restoration. However, the hyperparameters are interdependent, which means that suitable values of the hyperparameters vary depending on the used TV-based regularization term and the noise intensities on a given observation. Therefore, the settings of the hyperparameters are an essential but troublesome task.

In the following, we explain each TV. Let $\mathbf{D} = (\mathbf{D}_v^\top \mathbf{D}_h^\top)^\top \in \mathbb{R}^{2NB\times NB}$ be spatial differences operator with $\mathbf{D}_v$ and $\mathbf{D}_h$ being vertical and horizontal differences operator, respectively, and spectral differences operator are $\mathbf{D}_b \in \mathbb{R}^{NB\times NB}$. In [6, 7, 22], HTV, ASSTV, and SSTV are defined as follows:

$$\mathrm{HTV}(\mathbf{u}) := \|\mathbf{D}\mathbf{u}\|_{\mathrm{TV}}, \tag{3.2}$$

$$\mathrm{ASSTV}(\mathbf{u}) := \tau_v \|\mathbf{D}_v\mathbf{u}\|_1 + \tau_h \|\mathbf{D}_h\mathbf{u}\|_1 + \tau_b \|\mathbf{D}_b\mathbf{u}\|_1, \tag{3.3}$$

$$\mathrm{SSTV}(\mathbf{u}) := \|\mathbf{D}\mathbf{D}_b\mathbf{u}\|_1, \tag{3.4}$$

where $\|\cdot\|_{\mathrm{TV}}$ is a TV norm, which takes the ℓ_2 norm of spacial difference vectors for all band and then summing up for all spatial pixels, and τ_v, τ_h, and τ_b are the weight of the vertical, horizontal, and spectral differences. HTV evaluates direct spatial piecewise-smoothness and can be seen as a generalization of the standard color TV [33]. HTV does not consider spectral correlation, resulting in spatial oversmoothing. To consider the spectral correlation, the authors of [6] proposed SSAHTV. SSAHTV is a weighted HTV, and the weight is determined by spectral information. However, since SSAHTV does not directly evaluate spectral correlation, it still causes spatial oversmoothing. ASSTV evaluates direct spatial and spectral piecewise-smoothness (Fig. 3.1, blue line). The weights τ_v, τ_h, and τ_b in (3.3) balance the smoothness of vertical, horizontal, and spectral differences, respectively. Owing to the definition, ASSTV can evaluate spatial and spectral correlation, but it produces spectral oversmoothing even if we carefully adjust τ_v, τ_h, and τ_b. SSTV evaluate apriori knowledge on HS images using spatio-spectral piecewise-smoothness. It is derived by calculating spatial differences through spectral differences (Fig. 3.1, yellow line). SSTV can restore a desirable HS image without any weight, but it produces noise-like artifacts, especially when a given observation is contaminated by heavy noise and/or degradation.

LRM-Based Method

LRMR [5] is one of the popular LRM-based methods for HS image restoration, which evaluates the low rankness of an HS image in the spectral direction. To preserve the local details, LRMR restores a desirable HS image through patch-wise processing. Each

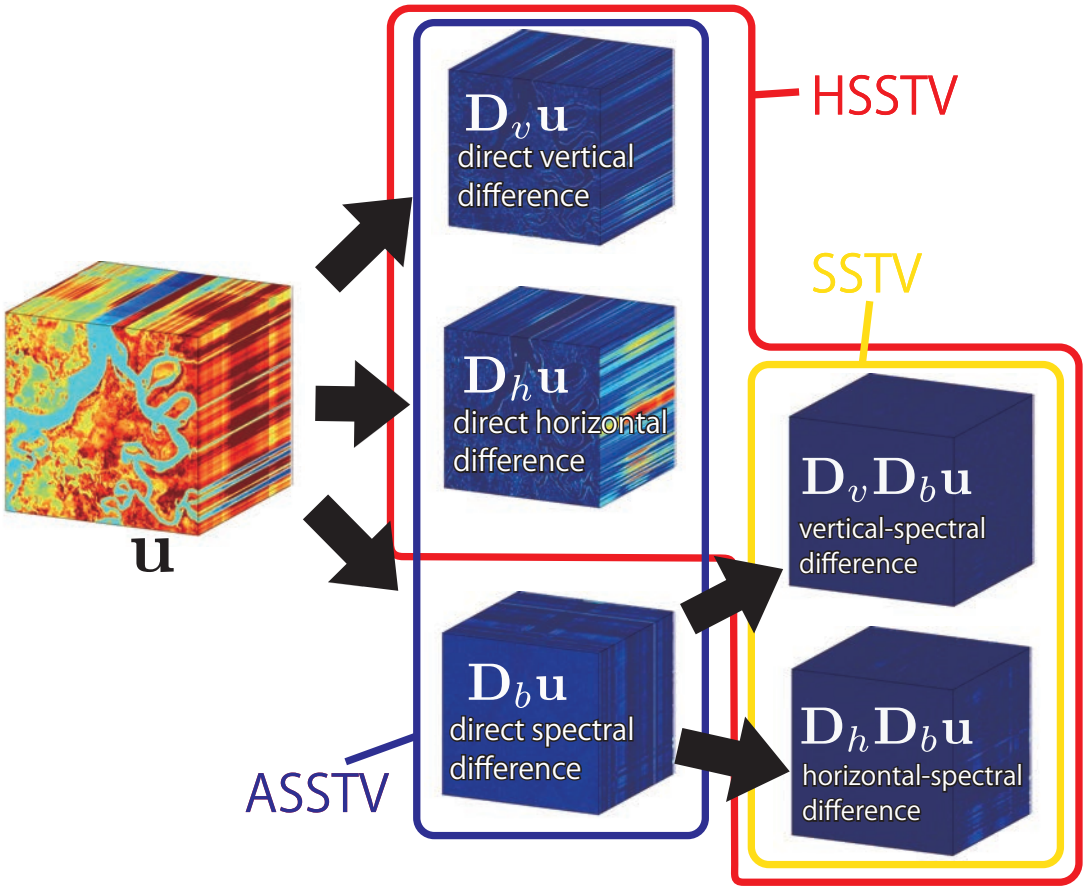

Figure 3.1: Calculation of local differences in SSTV, ASSTV, and our HSSTV. SSTV evaluates the ℓ_1 norm of spatio-spectral differences (yellow line). ASSTV evaluates the ℓ_1 norm of direct spatial and spectral differences (blue line). HSSTV evaluates the mixed $\ell_{1,p}$ norm of direct spatial and spatio-spectral differences (red line).

patch is a local cube of the size of $q \times q \times B$, and LRMR handles it as a matrix of size $q^2 \times B$ obtained by lexicographically arranging the spatial vectors in the patch cube in the row direction. The observation model is expressed like Section 3.1.1, and the restoration problem is formulated as follows:

$$\min_{\mathbf{U}_{i,j},\mathbf{S}_{i,j}} \|\mathbf{V}_{i,j} - \mathbf{U}_{i,j} - \mathbf{S}_{i,j}\|_F^2 \text{ s.t. } \operatorname{rank}(\mathbf{U}_{i,j}) \leq r, \ \operatorname{card}(\mathbf{S}_{i,j}) \leq k, \tag{3.5}$$

where $\mathbf{U}_{i,j}$, $\mathbf{V}_{i,j}$, and $\mathbf{S}_{i,j}$ represent the patches of a restored HS image, an observation, and a sparse noise, respectively, which are centered at (i,j) pixel. Then, the $\|\cdot\|_F$ is a Frobenius norm, $\operatorname{rank}(\cdot)$ represents a rank function, and $\operatorname{card}(\cdot)$ is a cardinality function. The method evaluates the low rankness of the estimated HS image and sparsity of the sparse noise by limiting the number of the rank of $\mathbf{U}_{i,j}$ and the cardinality of $\mathbf{S}_{i,j}$ using

r and k, respectively. Thanks to the design, LRMR achieves high-quality restoration for especially spectral information. Meanwhile, since LRMR does not fully consider spatial correlation, the result by LRMR tends to have spatial artifacts when an observation is corrupted by heavy noise and/or degradation. Besides, the rank and cardinality functions are nonconvex, and so it is a troublesome task to seek the global optimal solution of Prob. (3.5).

Combined Method

The methods [9,12,13,24–32,34] combine TV-based and LRM-based approaches. Since they can evaluate multiple types of apriori knowledge, i.e., piecewise-smoothness and low rankness, they can restore a more desirable HS image than the approaches only using TV-based or LRM-based regularization. Some methods [9, 13, 24–26, 28, 29, 32] approximate the rank and cardinality functions by their convex surrogates. As a result, the restoration problems are convex and can be solved by optimization methods based on proximal splitting.

However, the methods have to handle multiple regularization terms and/or a data-fidelity term(s) simultaneously in one objective function; they require to carefully control the hyperparameters balancing these terms. Since the hyperparameters rely on both the regularizations and the noise intensity on an observation, i.e., the hyperparameters are interdependent, the hyperparameter settings are often troublesome tasks.

3.1.2 Proposed method

Hybrid Spatio-Spectral Total Variation

First, we propose a new regularization technique for HS image restoration, named HSSTV. HSSTV simultaneously handles both direct local spatial differences and local spatio-spectral differences of an HS image. Then, HSSTV is defined by

$$\mathrm{HSSTV}(\mathbf{u}) := \|\mathbf{A}_\omega \mathbf{u}\|_{1,p} \text{ with } \mathbf{A}_\omega := \begin{pmatrix} \mathbf{D}\mathbf{D}_b \\ \omega \mathbf{D} \end{pmatrix}, \tag{3.6}$$

where $\|\cdot\|_{1,p}$ is the mixed $\ell_{1,p}$ norm, and $\omega \geq 0$. We assume $p = 1$ or 2, i.e., the ℓ_1 norm ($\|\cdot\|_{1,1} = \|\cdot\|_1$) or the mixed $\ell_{1,2}$ norm, respectively. We would like to mention that we can also see ℓ_1-HSSTV ($p = 1$) as anisotropic HSSTV and $\ell_{1,2}$-HSSTV ($p = 2$) as isotropic HSSTV.

In (3.6), $\mathbf{D}\mathbf{D}_b\mathbf{u}$ and $\mathbf{D}\mathbf{u}$ correspond to local spatio-spectral and direct local spatial differences, respectively, as shown in Fig. 3.1 (red lines). The weight ω adjusts the relative importance of direct spatial piecewise-smoothness to spatio-spectral piecewise-smoothness. HSSTV evaluates two kinds of smoothness by taking the ℓ_p norm ($p = 1$ or 2) of these differences associated with each pixel and then summing up for all pixels, i.e., calculating the ℓ_1 norm. Thus, it can be defined via the mixed $\ell_{1,p}$ norm. When we set $\omega = 0$ and $p = 1$, HSSTV recovers SSTV as (3.4), meaning that HSSTV can be seen as a generalization of SSTV.

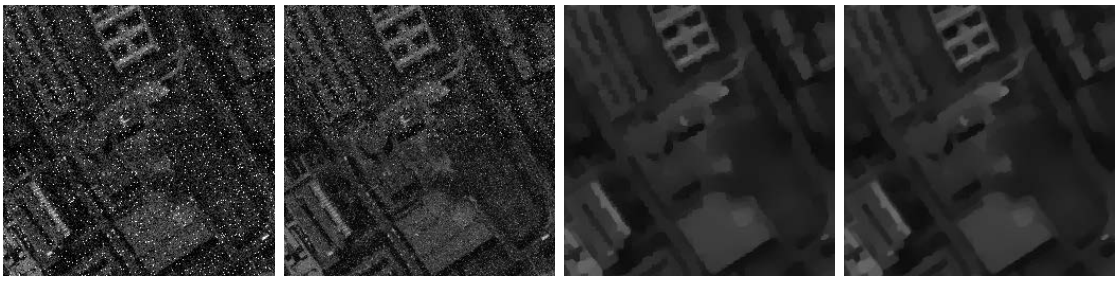

observation SSTV ℓ_1-HSSTV $\ell_{1,2}$-HSSTV

Figure 3.2: Restored HS images from an observation contaminated by similar noise in adjacent bands (the upper half area) and random noise (the lower half).

As reviewed in Section 3.1.1, since SSTV only evaluates spatio-spectral piecewise-smoothness, it cannot remove similar noise in adjacent bands. The direct spatial differences in HSSTV help to remove such noise. Fig. 3.2 is restored HS images from an observation contaminated by similar noise in adjacent bands (the upper half area) and random noise (the lower half area). One can see that large noise remains in the upper half area of the result by SSTV. In contrast, HSSTV effectively removes all noise. However, since minimizing the direct spatial differences strongly promotes spatial piecewise-smoothness, HSSTV produces spatial oversmoothing when the weight ω is large. Thus, the weight ω should be set to less than one, as demonstrated in Sec. 3.1.3.

HS Image Denoising by HSSTV

We consider restoring a desirable HS image $\bar{\mathbf{u}} \in \mathbb{R}^{NB}$ from an observation $\mathbf{v} \in \mathbb{R}^M$ ($M \leq NB$) contaminated by a Gaussian-sparse mixed noise. The observation model is given by the following form:

$$\mathbf{v} = \bar{\mathbf{u}} + \mathbf{n} + \mathbf{s}, \tag{3.7}$$

where $\mathbf{n} \in \mathbb{R}^M$ is Gaussian noise with the standard deviation σ, and $\mathbf{s} \in \mathbb{R}^M$ is a sparse noise.

Based on the above model, we formulate HS image restoration using HSSTV as the following optimization problem:

$$\min_{\mathbf{u},\mathbf{s}} \mathrm{HSSTV}(\mathbf{u}) \text{ s.t. } \left[\begin{array}{l} \mathbf{u}+\mathbf{s} \in \mathcal{B}^{\mathbf{v}}_{2,\varepsilon} := \{\mathbf{x} \in \mathbb{R}^M | \|\mathbf{v}-\mathbf{x}\| \leq \varepsilon\}, \\ \mathbf{s} \in \mathcal{B}_{1,\eta} := \{\mathbf{x} \in \mathbb{R}^M | \|\mathbf{x}\|_1 \leq \eta\}, \\ \mathbf{u} \in [\underline{\mu_{\mathbf{u}}}, \overline{\mu_{\mathbf{u}}}]^{NB}, \end{array}\right. \tag{3.8}$$

where $\mathcal{B}^{\mathbf{v}}_{2,\varepsilon}$ is a $\mathbf{v}$-centered ℓ_2-norm ball with the radius $\varepsilon > 0$, $\mathcal{B}_{1,\eta}$ is a $\mathbf{0}$-centered ℓ_1-norm ball with the radius $\eta > 0$, and $[\underline{\mu_{\mathbf{u}}}, \overline{\mu_{\mathbf{u}}}]^{NB}$ is a dynamic range of an HS image. Here, $\underline{\mu_{\mathbf{u}}}$ and $\overline{\mu_{\mathbf{u}}}$ are the minimum and maximum value of HS images, and $\underline{\mu_{\mathbf{u}}} < \overline{\mu_{\mathbf{u}}}$. This method simultaneously estimates the desirable HS image $\mathbf{u}$ and the sparse noise $\mathbf{s}$ for noise-robust restoration. The first and second constraints measure data fidelities to the observation $\mathbf{v}$ and the sparse noise $\mathbf{s}$, respectively. As mentioned in [8, 10, 12, 27, 35–42], such a constraint-type data-fidelity enables us to translate the hyperparameter(s)

balancing between regularization and data-fidelity like λ_1 and λ_2 in (3.1) to the upper bound of the degree of data-fidelity ε and η that can be set in a much easier manner.

Since all constraints are closed convex sets and HSSTV is a convex function, Prob. (3.8) is a constrained convex optimization problem. In this paper, we adopt ADMM (see Sec. 2.2) for solving the problem. In what follows, we reformulate Prob. (3.8) into Prob. (2.7).

We remove the hard constraints from Prob. (3.8) by using the indicator functions of the constraints. Prob. (3.8) can be rewritten as

$$\min_{\mathbf{u},\mathbf{s}} \|\mathbf{A}_\omega \mathbf{u}\|_{1,p} + \iota_{\mathcal{B}^{\mathbf{v}}_{2,\varepsilon}}(\mathbf{u}+\mathbf{s}) + \iota_{\mathcal{B}_{1,\eta}}(\mathbf{s}) + \iota_{[\underline{\mu_{\mathbf{u}}},\overline{\mu_{\mathbf{u}}}]^{NB}}(\mathbf{u}). \tag{3.9}$$

Note that from the definition of the indicator function, Prob. (3.9) is exactly equal to Prob. (3.8). By letting

$$f : \mathbb{R}^{NB} \to \mathbb{R}^2 : \mathbf{u} \mapsto (0,0), \tag{3.10}$$

$$g : \mathbb{R}^{5NB+2M} \to \mathbb{R} \cup \{\infty\} : (\mathbf{z}_1, \mathbf{z}_2, \mathbf{z}_3, \mathbf{z}_4) \mapsto \|\mathbf{z}_1\|_{1,p} + \iota_{\mathcal{B}^{\mathbf{v}}_{2,\varepsilon}}(\mathbf{z}_2) + \iota_{\mathcal{B}_{1,\varepsilon}}(\mathbf{z}_3) + \iota_{[\underline{\mu_{\mathbf{u}}},\overline{\mu_{\mathbf{u}}}]^{NB}}(\mathbf{z}_4), \tag{3.11}$$

$$\mathbf{G} : \mathbb{R}^{NB} \to \mathbb{R}^{5NB+2M} : \mathbf{u} \mapsto (\mathbf{A}_\omega \mathbf{u}, \mathbf{u}+\mathbf{s}, \mathbf{s}, \mathbf{u}). \tag{3.12}$$

Prob. (3.9) is reduced to Prob. (2.7). The resulting algorithm based on ADMM is summarized in Alg. 1.

Algorithm 1: ADMM method for Prob. (3.8)

input : $\mathbf{z}_1^{(0)}, \mathbf{z}_2^{(0)}, \mathbf{z}_3^{(0)}, \mathbf{z}_4^{(0)}, \mathbf{d}_1^{(0)}, \mathbf{d}_2^{(0)}, \mathbf{d}_3^{(0)}, \mathbf{d}_4^{(0)}$

while *A stopping criterion is not satisfied* **do**

- $(\mathbf{u}^{(n+1)}, \mathbf{s}^{(n+1)}) = \underset{\mathbf{u},\mathbf{s}}{\operatorname{argmin}} \frac{1}{2\gamma}(\|\mathbf{z}_1^{(n)} - \mathbf{A}_\omega \mathbf{u} - \mathbf{d}_1^{(n)}\|^2 + \|\mathbf{z}_2^{(n)} - (\mathbf{u}+\mathbf{s}) - \mathbf{d}_2^{(n)}\|^2 + \|\mathbf{z}_3^{(n)} - \mathbf{s} - \mathbf{d}_3^{(n)}\|^2 + \|\mathbf{z}_4^{(n)} - \mathbf{u} - \mathbf{d}_4^{(n)}\|^2)$;
- $\mathbf{z}_1^{(n+1)} = \operatorname{prox}_{\gamma\|\cdot\|_{1,p}}(\mathbf{A}_\omega \mathbf{u}^{(n+1)} + \mathbf{d}_1^{(n)})$;
- $\mathbf{z}_2^{(n+1)} = \operatorname{prox}_{\gamma \iota_{\mathcal{B}^{\mathbf{v}}_{2,\varepsilon}}}(\mathbf{u}^{(n+1)} + \mathbf{s}^{(n+1)} + \mathbf{d}_2^{(n)})$;
- $\mathbf{z}_3^{(n+1)} = \operatorname{prox}_{\gamma \iota_{\mathcal{B}_{1,\eta}}}(\mathbf{s}^{(n+1)} + \mathbf{d}_3^{(n)})$;
- $\mathbf{z}_4^{(n+1)} = \operatorname{prox}_{\gamma \iota_{[\underline{\mu_{\mathbf{u}}},\overline{\mu_{\mathbf{u}}}]^{NB}}}(\mathbf{u}^{(n+1)} + \mathbf{d}_4^{(n)})$;
- $\mathbf{d}_1^{(n+1)} = \mathbf{d}_1^{(n)} + \mathbf{A}_\omega \mathbf{u}^{(n+1)} - \mathbf{z}_1^{(n+1)}$;
- $\mathbf{d}_2^{(n+1)} = \mathbf{d}_2^{(n)} + \mathbf{u}^{(n+1)} + \mathbf{s}^{(n+1)} - \mathbf{z}_2^{(n+1)}$;
- $\mathbf{d}_3^{(n+1)} = \mathbf{d}_3^{(n)} + \mathbf{s}^{(n+1)} - \mathbf{z}_3^{(n+1)}$;
- $\mathbf{d}_4^{(n+1)} = \mathbf{d}_4^{(n)} + \mathbf{u}^{(n+1)} - \mathbf{z}_4^{(n+1)}$;
- $n \leftarrow n+1$;

The update of $\mathbf{u}$ and $\mathbf{s}$ in Alg. 1 comes down to the following forms:

$$\mathbf{u}^{(n+1)} = \left(\mathbf{A}_\omega^\top \mathbf{A}_\omega + \frac{3}{2}\mathbf{I}\right)^{-1} \mathrm{RHS},$$

$$\mathrm{RHS} = \mathbf{A}_\omega^\top(\mathbf{z}_1^{(n)} - \mathbf{d}_1^{(n)}) + \frac{1}{2}(\mathbf{z}_2^{(n)} - \mathbf{d}_2^{(n)}) - \frac{1}{2}(\mathbf{z}_3^{(n)} - \mathbf{d}_3^{(n)}) + (\mathbf{z}_4^{(n)} - \mathbf{d}_4^{(n)}),$$

$$\mathbf{s}^{(n+1)} = \frac{1}{2}(\mathbf{z}_2^{(n)} - \mathbf{u}^{(n+1)} - \mathbf{d}_2^{(n)} + \mathbf{z}_3^{(n)} - \mathbf{d}_3^{(n)}),$$

Since the update of $\mathbf{u}$ and $\mathbf{s}$ in Alg. 1 is strictly-convex quadratic minimization, one can obtain these updated forms by differentiating it.

For the update of $\mathbf{z}_1$, the proximity operators are reduced to simple soft-thresholding type operations described in Sec. 2.1. The updates of $\mathbf{z}_2$, $\mathbf{z}_3$, and $\mathbf{z}_4$ use the proximity operators of the indicator functions of each set, i.e., (2.4), (2.5), and (2.6), respectively.

3.1.3 Experimets

We demonstrate the advantages of the proposed method over three noise type: Gaussian noise, Gaussian-sparse mixed noise, and real noise. All the experiments were conducted by MATLAB 2018a.

To quantitatively evaluate restoration performance, we used the peak signal-to-noise ratio (PSNR) [dB] index and the structural similarity (SSIM) [43] index between a ground-truth $\bar{\mathbf{u}}$ and a restored HS image $\mathbf{u}$. PSNR is defined by $10\log_{10}(MAX_I^2/MSE)$, where MAX_I is the max value of the dynamic range of HS images, and MSE is the mean square error between ground-truth and restored HS images. The higher PSNR is, the more similar the two images are. SSIM is an image quality assessment index based on the human vision system, which is defined as follows:

$$\mathrm{SSIM}(\mathbf{u}, \bar{\mathbf{u}}) = \frac{1}{P}\sum_{i=1}^{P} \frac{(2\mu_{\mathbf{u}_i}\mu_{\bar{\mathbf{u}}_i} + C_1)(2\sigma_{\mathbf{u}_i\bar{\mathbf{u}}_i} + C_2)}{(\mu_{\mathbf{u}_i}^2 + \mu_{\bar{\mathbf{u}}_i}^2 + C_1)(\sigma_{\mathbf{u}_i}^2 + \sigma_{\bar{\mathbf{u}}_i}^2 + C_2)},$$

where $\mathbf{u}_i$ and $\bar{\mathbf{u}}_i$ are the ith pixel-centered local patches of a restored HS image and a ground-truth HS image, respectively, P is the number of patches, $\mu_{\mathbf{u}_i}$ and $\mu_{\bar{\mathbf{u}}_i}$ is the average values of the local patches of the restored and ground-truth HS images, respectively, $\sigma_{\mathbf{u}_i}$ and $\sigma_{\bar{\mathbf{u}}_i}$ represent the variances of $\mathbf{u}_i$ and $\bar{\mathbf{u}}_i$, respectively, and $\sigma_{\mathbf{u}_i\bar{\mathbf{u}}_i}$ denotes the covariance between $\mathbf{u}_i$ and $\bar{\mathbf{u}}_i$. Moreover, C_1 and C_2 are two constants, which avoid the numerical instability when either $\mu_{\mathbf{u}_i}^2 + \mu_{\bar{\mathbf{u}}_i}^2$ or $\sigma_{\mathbf{u}_i}^2 + \sigma_{\bar{\mathbf{u}}_i}^2$ is very close to zero. SSIM gives a normalized score between zero and one, where the maximum value means that $\mathbf{u}$ equals to $\bar{\mathbf{u}}$.

Gaussian noise removal

First, we conducted on Gaussian noise removal experiments. In these experiments, we generate a noisy observation based on (3.7) with $\mathbf{s} = 0$ and restore a desirable HS image $\mathbf{u}$. We use 13 HS images taken from the *SpecTIR* [44], *MultiSpec* [45] and *GIC* [46] as test images, where their dynamic range were normalized into $[0, 1]$. Here, the proposed denoising method assumes that the observation is contaminated by Gaussian and sparse noise, and then we improved the problem and the algorithm for Gaussian noise removal. Specifically, we formulate a Gaussian noise removal problem as follows:

$$\min_{\mathbf{u}} \mathrm{HSSTV}(\mathbf{u}) \text{ s.t. } \left[\begin{array}{l} \mathbf{u} \in \mathcal{B}_{2,\varepsilon}^{\mathbf{v}}, \\ \mathbf{u} \in [\underline{\mu_{\mathbf{u}}}, \overline{\mu_{\mathbf{u}}}]^{NB}, \end{array}\right.$$

Table 3.2: PSNR[dB] of the results on Gaussian noise removal experiments.

	σ	HTV	SSTV	ASSTV	BM4D	Proposed ($p=1$)	Proposed ($p=2$)
Beltsville	0.05	32.19	35.64	31.99	**37.01**	36.41	36.19
$n=256$	0.1	29.33	31.11	28.58	**33.39**	33.15	32.79
$m=256$	0.2	26.92	26.03	25.36	30.03	**30.23**	29.80
$b=32$	0.3	25.79	22.81	23.90	28.04	**28.68**	28.30
Suwannee	0.05	33.03	37.28	33.34	38.05	38.69	**38.73**
$n=256$	0.1	30.04	31.88	30.44	34.56	35.17	**35.19**
$m=256$	0.2	27.32	27.54	27.83	31.53	31.94	**32.01**
$b=32$	0.3	25.88	25.03	26.42	29.79	30.21	**30.30**
DC	0.05	30.06	35.56	30.87	**36.16**	35.96	35.57
$n=256$	0.1	26.87	30.93	27.65	31.88	**32.16**	31.74
$m=256$	0.2	24.29	25.86	24.92	28.27	**28.72**	28.33
$b=32$	0.3	23.05	22.63	23.52	26.43	**26.93**	26.57
Cuprite	0.05	34.32	37.64	33.40	39.10	**39.58**	39.56
$n=256$	0.1	31.62	31.97	30.34	35.65	**36.29**	36.26
$m=256$	0.2	29.31	27.22	27.41	32.39	**33.32**	**33.32**
$b=32$	0.3	28.13	24.50	25.71	30.60	31.75	**31.77**
Reno	0.05	32.01	36.76	32.25	37.46	**37.65**	37.43
$n=256$	0.1	28.98	31.79	29.23	33.44	**34.07**	33.83
$m=256$	0.2	26.50	26.57	26.78	29.91	**30.83**	30.65
$b=32$	0.3	25.19	24.47	25.54	28.12	**29.15**	29.03
Botswana	0.05	31.35	35.32	30.98	**36.01**	35.73	35.65
$n=256$	0.1	28.27	31.17	27.62	32.33	**32.46**	32.30
$m=256$	0.2	25.59	26.37	24.66	28.94	**29.43**	29.26
$b=32$	0.3	24.26	23.21	23.12	27.07	**27.81**	27.67
IndianPines	0.05	33.13	33.70	32.75	**34.59**	34.34	34.03
$n=145$	0.1	31.46	30.67	30.40	32.17	**32.41**	32.05
$m=145$	0.2	30.22	26.38	28.28	30.19	**30.95**	30.67
$b=32$	0.3	29.67	24.25	26.79	29.04	**30.26**	30.07
KSC	0.05	33.89	37.67	34.29	39.36	**39.44**	39.41
$n=256$	0.1	31.21	32.08	31.40	35.30	**36.15**	36.09
$m=256$	0.2	28.96	27.41	28.86	31.86	**33.14**	33.10
$b=32$	0.3	27.82	25.21	27.52	30.10	**31.59**	31.54
PaviaLeft	0.05	31.23	37.66	32.07	38.09	**38.23**	37.98
$n=216$	0.1	27.97	32.55	28.78	33.87	**34.39**	34.22
$m=216$	0.2	25.23	28.36	26.04	29.92	**30.83**	30.71
$b=32$	0.3	23.93	25.48	24.69	27.78	**28.94**	28.83
PaviaRight	0.05	31.90	37.62	33.00	**38.77**	38.63	38.38
$n=256$	0.1	28.58	32.25	29.61	34.60	**34.94**	34.69
$m=256$	0.2	25.73	28.59	26.71	30.53	**31.43**	31.21
$b=32$	0.3	24.33	25.76	25.26	28.34	**29.50**	29.31
PaviaU	0.05	32.16	37.65	33.18	**38.96**	38.81	38.60
$n=256$	0.1	28.90	32.77	29.88	34.89	**35.20**	35.01
$m=256$	0.2	26.07	28.60	27.06	30.86	**31.74**	31.61
$b=32$	0.3	24.65	25.62	25.63	28.74	**29.82**	29.71
Salinas	0.05	35.93	37.61	35.34	40.27	40.42	**40.44**
$n=217$	0.1	33.05	31.93	32.37	36.89	37.30	**37.36**
$m=217$	0.2	30.56	26.58	29.62	33.61	34.31	**34.43**
$b=32$	0.3	29.16	24.09	28.15	31.73	32.63	**32.80**
SalinaA	0.05	36.17	37.54	34.05	39.60	**39.92**	39.81
$n=83$	0.1	33.15	32.25	30.20	35.73	**36.72**	36.46
$m=86$	0.2	29.93	26.63	26.20	31.83	**33.64**	33.30
$b=32$	0.3	28.15	23.65	24.11	29.61	**31.96**	31.63

Table 3.3: SSIM of the results on Gaussian noise removal experiments.

	σ	HTV	SSTV	ASSTV	BM4D	Proposed ($p=1$)	Proposed ($p=2$)
Beltsville	0.05	0.8370	0.9076	0.8602	**0.9355**	0.9305	0.9262
	0.1	0.7483	0.7724	0.7772	**0.8737**	0.8668	0.8562
	0.2	0.6583	0.5230	0.6811	**0.7833**	0.7798	0.7630
	0.3	0.6150	0.3709	0.6216	0.7170	**0.7239**	0.7080
Suwannee	0.05	0.8723	0.9521	0.8937	0.9563	0.9648	**0.9657**
	0.1	0.7959	0.8646	0.8263	0.9104	0.9276	**0.9285**
	0.2	0.7091	0.6772	0.7512	0.8406	0.8668	**0.8672**
	0.3	0.6565	0.5401	0.7058	0.7866	0.8209	**0.8211**
DC	0.05	0.8584	0.9486	0.8929	**0.9635**	0.9633	0.9586
	0.1	0.7307	0.8679	0.7866	0.9140	**0.9156**	0.9065
	0.2	0.5772	0.6927	0.6417	0.8184	**0.8255**	0.8131
	0.3	0.4941	0.5456	0.5541	0.7335	**0.7501**	0.7377
Cuprite	0.05	0.8742	0.9412	0.8870	0.9538	0.9602	**0.9618**
	0.1	0.8095	0.8354	0.8284	0.9081	0.9226	**0.9243**
	0.2	0.7489	0.6115	0.7699	0.8342	0.8653	**0.8665**
	0.3	0.7200	0.4609	0.7391	0.7798	0.8244	**0.8258**
Reno	0.05	0.8604	0.9527	0.8859	0.9599	**0.9649**	0.9638
	0.1	0.7560	0.8635	0.7973	0.9083	**0.9220**	0.9193
	0.2	0.6503	0.6919	0.6935	0.8177	**0.8452**	0.8419
	0.3	0.5973	0.5588	0.6368	0.7469	**0.7848**	0.7821
Botswana	0.05	0.8495	0.9371	0.8592	0.9357	0.9468	**0.9477**
	0.1	0.7528	0.8629	0.7668	0.8721	0.9020	**0.9048**
	0.2	0.6405	0.6996	0.6578	0.7802	0.8313	**0.8349**
	0.3	0.5765	0.5574	0.5920	0.7117	0.7765	**0.7806**
IndianPines	0.05	0.8292	0.8414	0.8520	**0.8829**	0.8758	0.8635
	0.1	0.7752	0.6903	0.7838	0.8122	**0.8164**	0.7989
	0.2	0.7414	0.4407	0.7441	0.7445	**0.7673**	0.7554
	0.3	0.7306	0.3198	0.7280	0.6994	**0.7464**	0.7401
KSC	0.05	0.8879	0.9361	0.9035	0.9651	0.9690	**0.9691**
	0.1	0.8180	0.8185	0.8396	0.9162	**0.9367**	0.9358
	0.2	0.7508	0.6337	0.7727	0.8346	**0.8799**	0.8786
	0.3	0.7171	0.4786	0.7352	0.7757	**0.8384**	0.8369
PaviaLeft	0.05	0.8612	0.9699	0.8855	0.9683	**0.9720**	0.9705
	0.1	0.7354	0.9169	0.7776	0.9203	**0.9346**	0.9316
	0.2	0.5714	0.7877	0.6317	0.8224	**0.8589**	0.8537
	0.3	0.4782	0.6546	0.5415	0.7343	**0.7900**	0.7834
PaviaRight	0.05	0.8625	0.9617	0.8894	0.9653	**0.9703**	0.9692
	0.1	0.7484	0.8911	0.7904	0.9175	**0.9351**	0.9321
	0.2	0.6065	0.7355	0.6605	0.8163	**0.8659**	0.8592
	0.3	0.5252	0.5927	0.5804	0.7256	**0.8038**	0.7942
PaviaU	0.05	0.8719	0.9602	0.8943	0.9649	**0.9690**	0.9675
	0.1	0.7784	0.8879	0.8133	0.9226	**0.9336**	0.9300
	0.2	0.6585	0.7220	0.7059	0.8378	**0.8693**	0.8647
	0.3	0.5858	0.5759	0.6386	0.7682	**0.8154**	0.8107
Salinas	0.05	0.9202	0.9246	0.9297	0.9615	0.9638	**0.9647**
	0.1	0.8837	0.7949	0.8951	0.9332	0.9405	**0.9423**
	0.2	0.8480	0.5415	0.8578	0.8882	0.9092	**0.9121**
	0.3	0.8293	0.4067	0.8382	0.8486	0.8868	**0.8908**
SalinaA	0.05	0.9231	0.9364	0.9252	0.9580	0.9670	**0.9688**
	0.1	0.8915	0.8238	0.8821	0.9164	0.9416	**0.9443**
	0.2	0.8509	0.5880	0.8255	0.8416	0.9049	**0.9068**
	0.3	0.8242	0.4288	0.7932	0.7837	0.8782	**0.8797**

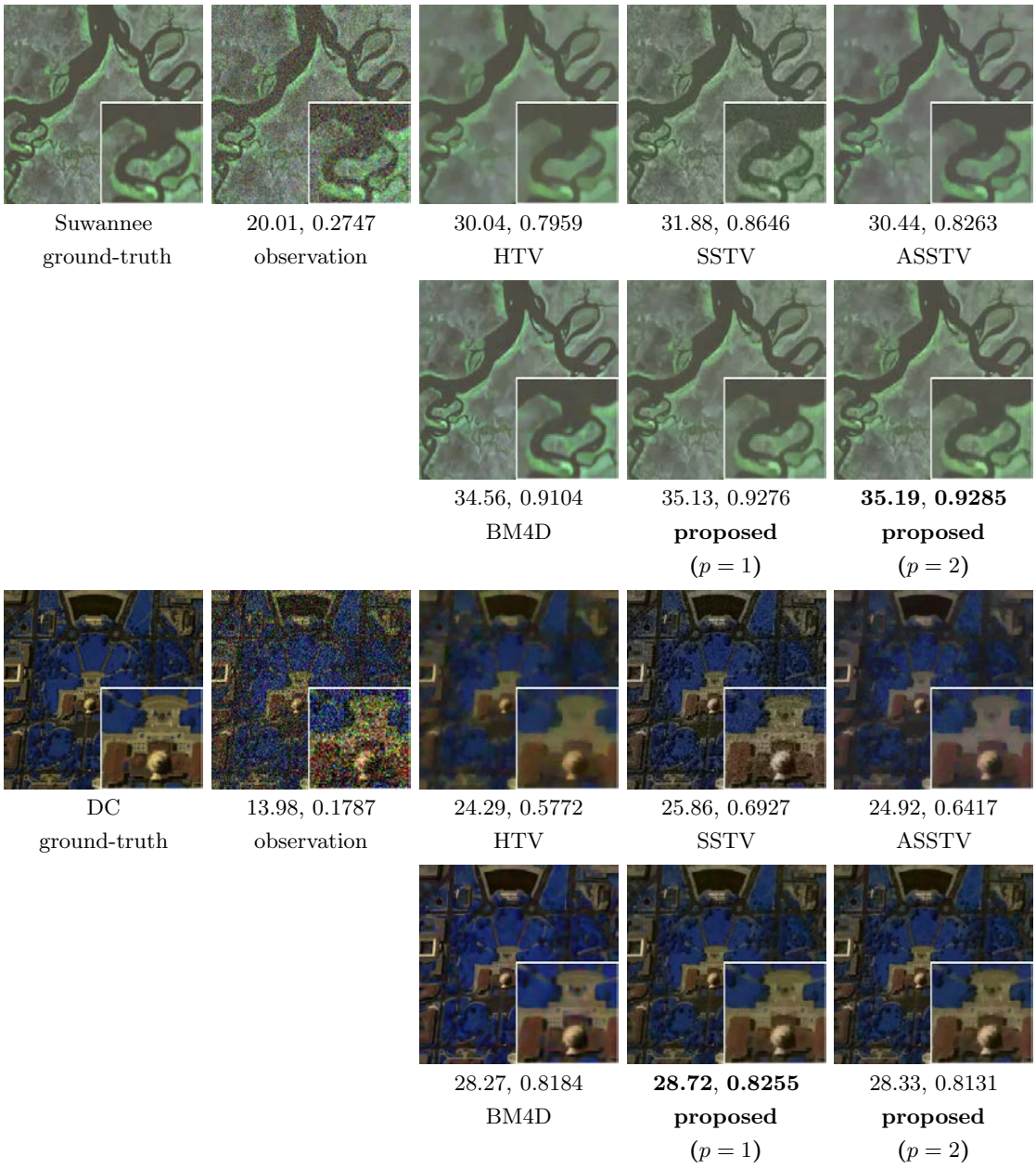

Figure 3.3: Resulting HS images with their PSNR[dB] (left) and SSIM (right) in the Gaussian denoising experiment (top: Suwannee, $\sigma = 0.1$, bottom: DC, $\sigma = 0.2$).

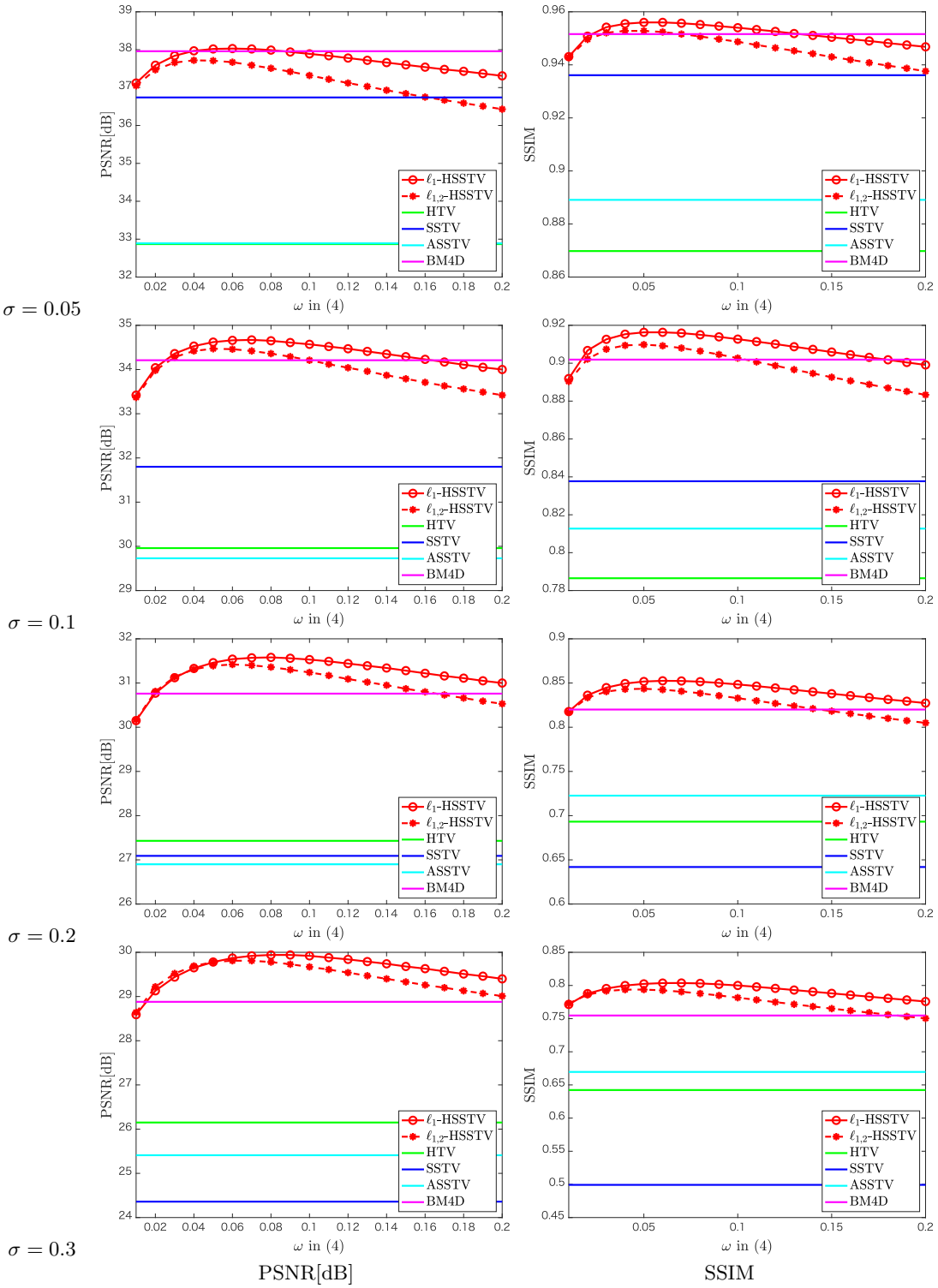

Figure 3.4: PSNR[dB] or SSIM versus ω in (3.6) in the Gaussian denoising experiment.

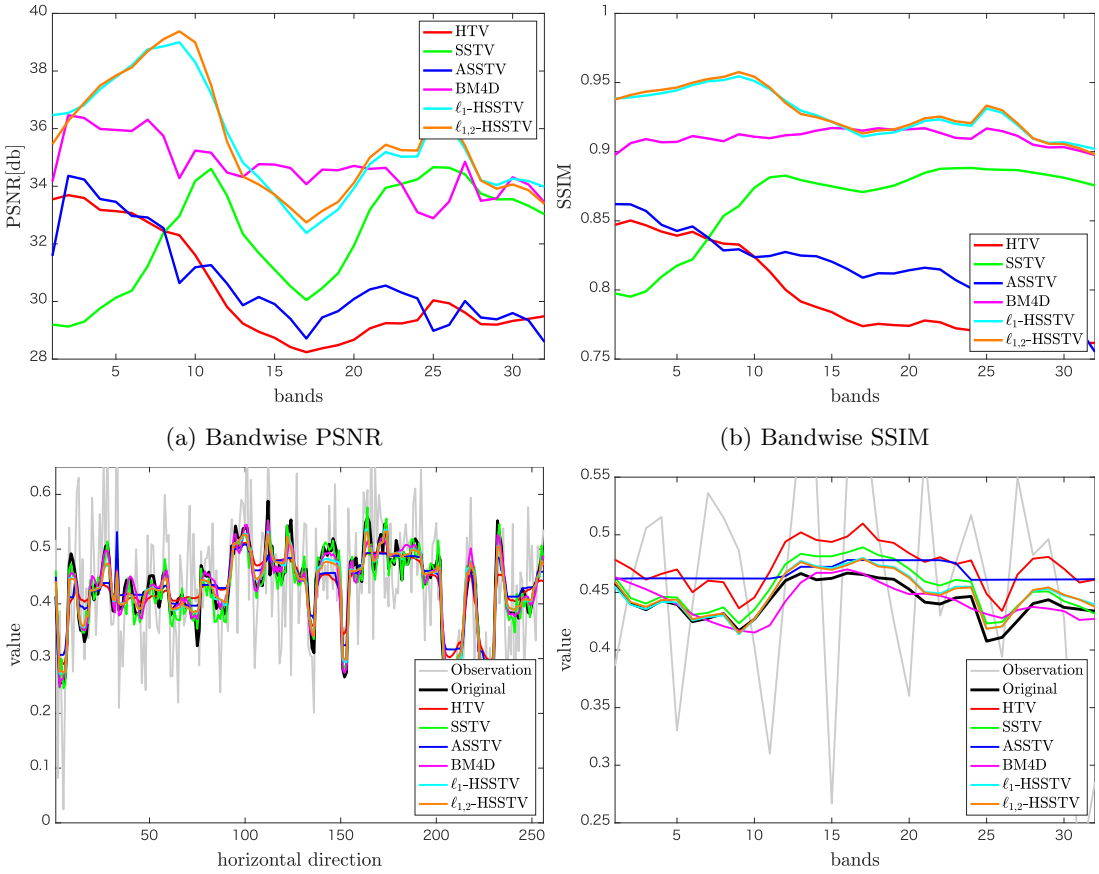

(a) Bandwise PSNR

(b) Bandwise SSIM

(c) Spatial response

(d) Spectral response

Figure 3.5: Bandwise PSNR[dB] and SSIM and spatial and spectral responses in the Gaussian denoising experiment (Suwannee).

and solve it by ADMM.

We compared the proposed method with HTV [6], SSTV [7] and ASSTV [8]. For a fair comparison, we replaced HSSTV in Prob. (3.8) with HTV, SSTV or ASSTV, and solved the problem by ADMM. We also compare HSSTV with BM4D [47], which is known to be a state-of-the-art denoising method for 3D signals. Note that BM4D and a recent CNN-based HS image denoising method [48] cannot be represented as explicit regularization functions and are fully customized to denoising tasks. In contrast, our HSSTV can be used as a building block in various HS image restoration methods based on optimization. In addition, BM4D is a nonlocal method, and thus, it has several limitations. Meanwhile, CNN-based methods strongly depend on what training data are used, which means that they cannot adapt to a wide range of noise intensity. Thus, the design concepts of these methods are different from TVs, and the comparison of HSSTV and BM4D is just a reference. We also remark that we do not compare HSSTV with LRM-based techniques. This is because our focus is to evaluate the potential of local TV regularization techniques

including HTV, SSTV, ASSTV, and our HSSTV.

The radius ε in Prob. (3.8) was set to $\sqrt{NB\sigma^2}$. In the ASSTV case, we set the weights $\tau_v = \tau_h = \tau_b = 1$. In the BM4D case, we used the program code distributed by the authors of [47]. We set the max iteration number, the stepsize γ and the stopping criterion of ADMM to 5000, 0.1 and $\|\mathbf{u}^{(n)} - \mathbf{u}^{(n+1)}\| < 0.01$, respectively.

In Tab. 3.2 and 3.3, we show PSNR and SSIM of the denoised HS images by each method for various σ and HS images, respectively. The balancing weight ω in HSSTV is set to 0.08 for the ℓ_1-norm case and 0.06 for the $\ell_{1,2}$-norm case. For all HS images, σ and quality measures, HSSTV outperforms HTV, SSTV, and ASSTV. In addition, even though HSSTV does not utilize nonlocal information, the denoising ability is better than BM4D for most cases. We also found that SSTV does not work well when σ is large. On the other hand, HSSTV is effective for a wide range of noise intensity. This would be because HSSTV evaluates direct spatial piecewise smoothness.

Fig. 3.3 shows the resulting images on *Suwannee* ($\sigma = 0.1$, top) and *DC* ($\sigma = 0.2$, bottom) with their PSNR (left) and SSIM (right). Here, we depict these HS images as RGB images, where R, G and B are 8th, 16th, and 32rd bands of HS images. In Fig. 3.3, we show both the results and the magnified image of the small range, because one can more see the advantage of the results by the proposed method. One can see that the results by HTV and ASSTV lose spacial details, and noise remains in the results by SSTV. In the case of $\sigma = 0.1$, BM4D can restore a high quality HS image, but it produces spectral artifacts in the case of $\sigma = 0.2$. This means that BM4D cannot preserve spectral information when an observed image is heavily contaminated by noise. In contrast, HSSTV can restore HS images preserving both details and spectral information without artifacts.

Fig. 3.4 plots PSNR or SSIM of the results by HSSTV versus various ω changed from 0.01 to 0.2, where the values of PSNR and SSIM are averaged over the 13 HS images. One can see that $\omega \in [0.05, 0.1]$ is a good choice in most cases.

Fig. 3.5 plots bandwise PSNR and SSIM (left) and spatial and spectral responses (right) of the denoised *Suwannee* HS image, where $\sigma = 0.1$. The graphs regarding bandwise PSNR and SSIM show that HSSTV achieves higher-quality restoration than HTV, SSTV, and ASSTV for all bands and BM4D for most bands. The graph (c) plots the spatial response of the 243rd row of the 30th band. In the same way, the graph (d) plots the spectral response of the 243rd row and 107th col. We can see that the spatial response of the results by HTV and ASSTV are too smooth compared with the true one. On the other hand, there exist undesirable variations in the spatial response of the result by SSTV. In contrast, BM4D and HSSTV restore similar responses to the true one. In the graph (d), one can see that (i) the shape of the spectral responses of the results by HTV and SSTV are similar to the that of true one, but the mean values are larger than the true one, (ii) the spectral response of the results by ASSTV and BM4D are too smooth and different from the true one, and (iii) HSSTV can restore a spectral response very similar to the true one.

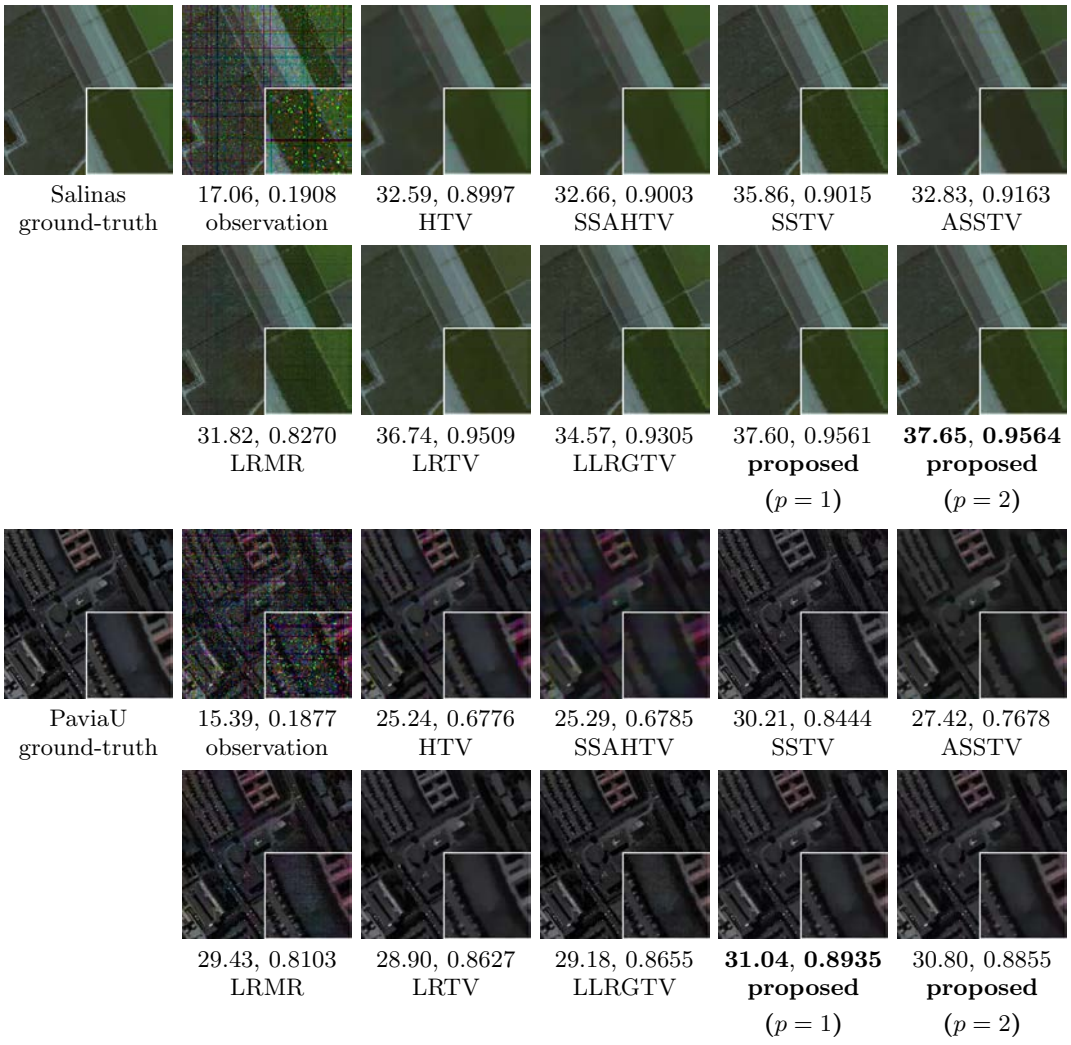

Figure 3.6: Resulting HS images with their PSNR[dB] (left) and SSIM (right) in the mixed noise removal experiment (top: Salinas, the noise level (i), bottom: PaviaU, the noise level (ii)).

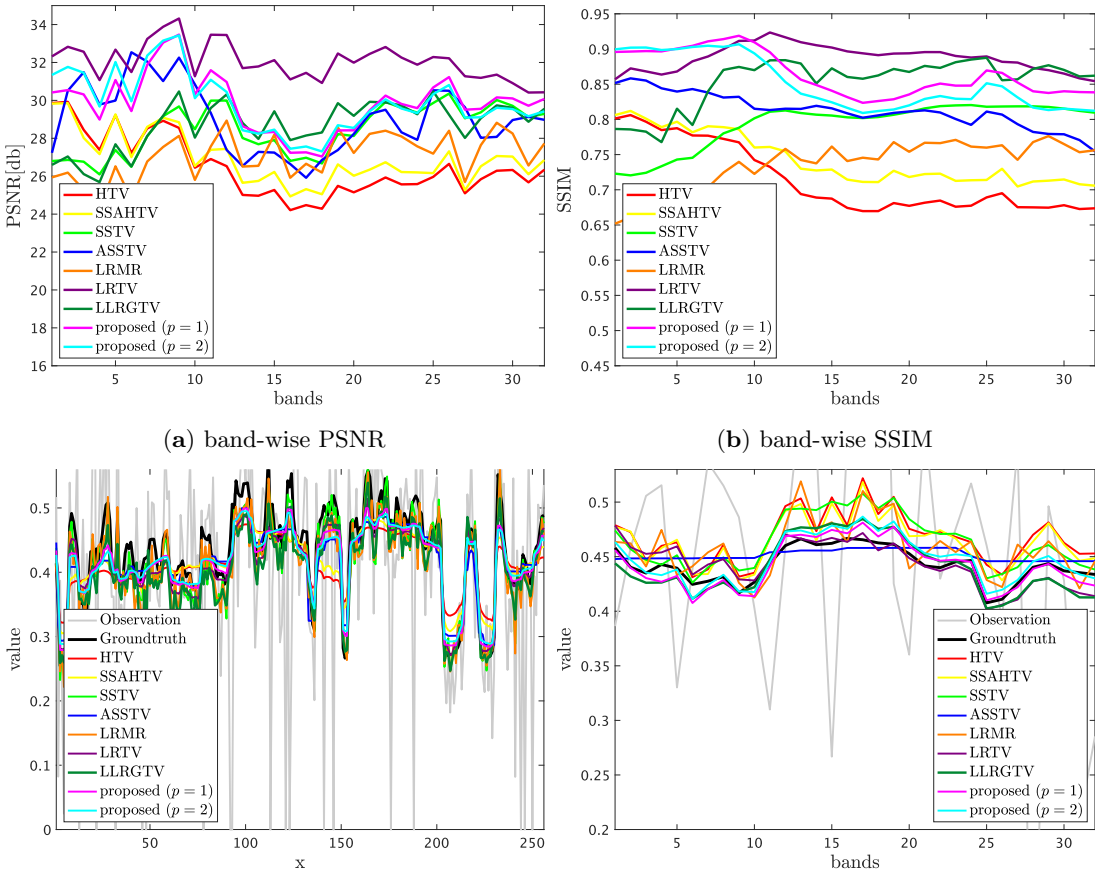

(**a**) band-wise PSNR

(**b**) band-wise SSIM

(**c**) Spatial response

(**d**) Spectral response

Figure 3.7: Band-wise PSNR[dB] and SSIM and spatial and spectral responses in the mixed noise removal experiment (Suwannee).

Table 3.4: Parameter settings for ASSTV, LRMR, LRTV, and the proposed method.

Parameters \ Noise Level		(i) $(\sigma,\ s_p,\ l_v = l_h) = (0.05,\ 0.04,\ 0.04)$	(ii) $(0.1,\ 0.05,\ 0.05)$
ASSTV	$\tau_v = \tau_h$	1	
	τ_b	3	2
LRMR	r	3	
	k	$s_p + l_v + l_h - l_v l_h$ (the rate of sparse noise)	
LRTV	r	2	
	τ	0.005	0.008
LLRGTV	r	2	
	λ	0.1	
	τ	0.01	
proposed	ω	0.04	

Mixed noise removal

We conducted on the simulation experiments for Gaussian-sparse mixed noise removal. In the experiments, we used 13 HS images as like Gaussian noise removal experiment. The observed HS images included an additive white Gaussian noise $\mathbf{n}$ with the standard deviation σ and sparse noise $\mathbf{s}$, which is equal to (3.7). We assumed that sparse noise consists of salt-and-pepper noise and vertical and horizontal line noise, with these noise ratio in all pixels being s_p, l_v, and l_h, respectively. We generated noisy HS images by adding two types of mixed noise to ground-truth HS images: (i) $(\sigma,\ s_p,\ l_v = l_h) = (0.05,\ 0.04,\ 0.04)$, (ii) $(0.1,\ 0.05,\ 0.05)$.

The proposed method was compared with HTV [6], SSAHTV [6], SSTV [7], and ASSTV [8]. For a fair comparison, we replaced HSSTV in Prob. (3.8) with HTV, SSAHTV, SSTV, or ASSTV and solved the problem by ADMM. We also compared our proposed method with LRMR [5], TV-regularized low-rank matrix factorization (LRTV) [12], and local low-rank matrix recovery and global spatial-spectral TV (LLRGTV) [27]. We did not compare our proposed method with recent CNN-based HS image denoising methods [48]. The CNN-based methods cannot be represented as explicit regularization functions and are fully customized to denoising tasks. In contrast, our proposed method can be used as a building block in various HS image restoration methods based on optimization. Meanwhile, CNN-based methods strongly depend on what training data are used, which means that they cannot adapt to a wide range of noise intensity. Thus, the design concepts of these methods are different from TVs and LRM-based approaches.

We set ε and η in Prob. (3.8) as $0.83\sqrt{NB(1-(s_p(1-l_v-l_h)+l_v+l_h-l_vl_h))\sigma^2}$ and $NB(0.45s_p+(l_v+l_h)v_{ave}-l_vl_hv_{ave})$, respectively, where v_{ave} is the average of the observed image. Tab. 3.4 shows the parameters settings for ASSTV, LRMR, LRTV, LLRGTV, and the proposed method. We set these parameters to achieve the best performance for each method. We set the max iteration number, the stepsize γ, and the stopping criterion of ADMM to 10000, 0.05, and $\|\mathbf{u}^{(n)} - \mathbf{u}^{(n+1)}\| < 0.01$, respectively.

Table 3.5: PSNR[dB] (top) and SSIM (bottom) in mixed noise removal experiments.

	HS image	Noise Level	HTV	SSAHTV	SSTV	ASSTV	LRMR	LRTV	LLRGTV	**Proposed ($p = 1$)**	**Proposed ($p = 2$)**
PSNR	Beltsville	(i)	29.43	29.47	33.66	27.16	30.91	**35.32**	33.61	34.25	34.16
		(ii)	26.40	26.43	28.42	24.60	27.13	**31.22**	28.51	29.79	29.62
	Suwannee	(i)	30.14	30.18	34.59	32.60	30.30	**36.20**	33.35	35.15	36.01
		(ii)	26.70	26.74	29.55	28.71	26.90	**31.95**	28.50	31.08	31.22
	DC	(i)	26.46	26.51	33.03	28.80	31.71	**34.78**	33.50	33.36	33.08
		(ii)	23.84	23.88	27.71	25.25	27.35	**29.53**	28.14	28.57	28.32
	Cuprite	(i)	31.67	31.68	34.42	29.14	30.16	28.39	32.67	34.96	**36.20**
		(ii)	28.20	28.21	29.86	26.57	27.32	27.94	27.99	31.63	**31.73**
	Reno	(i)	28.53	28.57	34.37	30.49	32.21	**37.06**	34.95	35.11	34.96
		(ii)	25.56	25.61	28.11	26.95	28.47	**31.00**	27.99	29.83	29.72
	Botswana	(i)	27.98	28.05	33.32	26.47	31.62	29.00	32.02	**33.61**	33.53
		(ii)	25.21	25.25	28.55	24.01	28.31	27.33	28.08	**29.39**	29.35
	IndianPines	(i)	31.05	31.06	31.45	29.07	28.96	26.16	29.74	**31.90**	31.80
		(ii)	28.57	28.57	27.82	26.72	25.14	**29.82**	26.70	29.26	29.18
	KSC	(i)	30.17	30.25	34.74	31.64	33.74	35.74	34.75	**36.39**	36.33
		(ii)	28.03	28.06	29.23	28.62	30.19	30.22	29.53	**31.82**	31.72
	PaviaLeft	(i)	27.62	27.70	35.57	30.91	33.01	**36.49**	34.75	35.98	35.81
		(ii)	24.74	24.78	29.93	26.71	29.46	29.02	29.22	**30.47**	30.24
	PaviaRight	(i)	26.93	27.35	34.54	31.13	33.33	**35.82**	34.17	35.68	35.23
		(ii)	24.90	25.16	30.70	27.23	29.82	29.08	29.24	**31.59**	31.39
	PaviaU	(i)	27.92	28.04	35.52	31.65	33.00	**36.72**	34.59	36.31	36.17
		(ii)	25.24	25.29	30.21	27.42	29.43	28.90	29.17	**31.04**	30.80
	Salinas	(i)	32.59	32.64	35.86	32.83	31.82	36.74	34.36	37.60	**37.65**
		(ii)	28.88	28.91	28.19	28.99	28.02	**32.73**	29.09	32.01	32.12
	SalinaA	(i)	32.54	32.65	35.29	28.12	31.18	28.49	34.07	**36.27**	36.23
		(ii)	28.69	28.80	29.67	25.19	27.67	26.10	27.87	**31.68**	31.64
SSIM	Beltsville	(i)	0.7902	0.7904	0.8856	0.8111	0.8583	**0.9372**	0.9278	0.9132	0.9085
		(ii)	0.6954	0.6959	0.7057	0.7177	0.7083	**0.8568**	0.8248	0.8186	0.8088
	Suwannee	(i)	0.8406	0.8410	0.9353	0.9052	0.8689	0.9502	0.9431	**0.9559**	0.9555
		(ii)	0.7542	0.7552	0.8146	0.8226	0.7470	0.8930	0.8622	0.9125	**0.9158**
	DC	(i)	0.7622	0.7633	0.9274	0.8676	0.9248	**0.9613**	0.9548	0.9442	0.9394
		(ii)	0.6189	0.6201	0.8092	0.7211	0.8214	**0.8810**	0.8722	0.8611	0.8533
	Cuprite	(i)	0.8550	0.8552	0.9179	0.8632	0.8495	0.9396	0.9411	**0.9459**	0.9426
		(ii)	0.7849	0.7852	0.7717	0.7953	0.7098	0.8814	0.8524	0.9031	**0.9058**
	Reno	(i)	0.7818	0.7819	0.9322	0.8832	0.9012	**0.9589**	0.9523	0.9531	0.9515
		(ii)	0.6640	0.6645	0.8045	0.7539	0.7905	**0.8816**	0.8640	0.8679	0.8635
	Botswana	(i)	0.7896	0.7900	0.9202	0.8199	0.9068	0.9282	**0.9384**	0.9343	0.9344
		(ii)	0.6810	0.6820	0.8175	0.7095	0.8201	0.8564	0.8756	0.8745	**0.8765**
	IndianPines	(i)	0.8118	0.8120	0.8015	0.7671	0.7593	0.8190	0.8224	**0.8335**	0.8243
		(ii)	0.7713	0.7713	0.6229	0.7303	0.7893	**0.7939**	0.7433	0.7785	0.7689
	KSC	(i)	0.8271	0.8278	0.9116	0.8922	0.8890	0.9385	0.9322	**0.9542**	0.9532
		(ii)	0.7598	0.7602	0.7885	0.8064	0.7529	0.8427	0.8216	**0.8809**	0.8747
	PaviaLeft	(i)	0.7752	0.7770	0.9593	0.8828	0.9359	0.9612	0.9601	**0.9661**	0.9645
		(ii)	0.6102	0.6116	0.8755	0.7267	0.8565	0.8791	0.8882	**0.8898**	0.8815
	PaviaRight	(i)	0.7769	0.7772	0.9494	0.8862	0.9256	0.9540	0.9470	**0.9616**	0.9598
		(ii)	0.6474	0.6471	0.8635	0.7493	0.8261	0.8507	0.8551	**0.9086**	0.9006
	PaviaU	(i)	0.7973	0.7986	0.9452	0.8891	0.9124	0.9540	0.9493	**0.9622**	0.9610
		(ii)	0.6776	0.6785	0.8444	0.7678	0.8103	0.8627	0.8649	**0.8935**	0.8855
	Salinas	(i)	0.8997	0.9002	0.9015	0.9163	0.8270	0.9509	0.9285	0.9561	**0.9564**
		(ii)	0.8570	0.8575	0.7117	0.8732	0.6670	0.9225	0.8333	0.9223	**0.9240**
	SalinaA	(i)	0.9129	0.9137	0.9134	0.8468	0.8632	0.9384	**0.9513**	0.9448	0.9416
		(ii)	0.8793	0.8803	0.7789	0.8110	0.7266	0.8951	0.8549	**0.9197**	0.9195

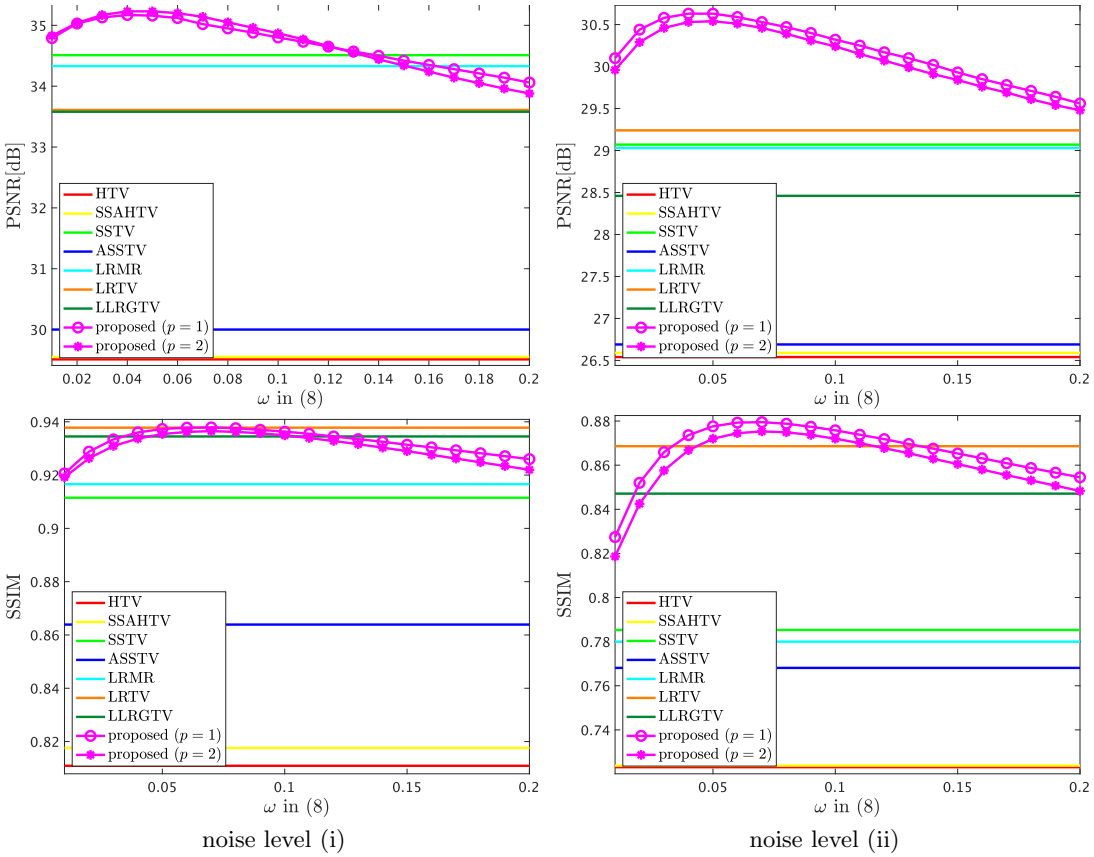

Figure 3.8: PSNR[dB] (top) or SSIM (bottom) versus ω in (3.6) in the mixed noise removal experiment.

In Tab. 3.5, we show the PSNR and SSIM of the denoised HS images by each method for two types of noise intensity and HS images. For HTV, SSAHTV, SSTV, ASSTV, and LRMR, the proposed method outperforms the existing methods. Besides, one can see that the PSNR and SSIM of the results by the proposed method are higher than those by LLRGTV for most situations. Meanwhile, LRTV outperforms the proposed method in some cases. This would be because LRTV combines TV-based and LRM-based regularization techniques. We would like to mention that the proposed method outperforms LRTV in over half of the situations, even though it uses only TV-based regularization.

Fig. 3.6 shows the resulting images on *Salinas* (the noise level (i), top) and *PaviaU* (the noise level (ii), bottom), with their PSNR (left) and SSIM (right). Here, we depicted these HS images as RGB images (R = 8th, G = 16th, and B = 32nd bands). One can see that the results by HTV, SSAHTV, and ASSTV lose spatial details, and noise remains in the results by SSTV, LRMR, and LLRGTV. Besides, since the restored images by SSTV and LRTV lose color with large noise intensity, SSTV and LRTV change spectral variation. In contrast, the proposed method can restore HS images preserving both details

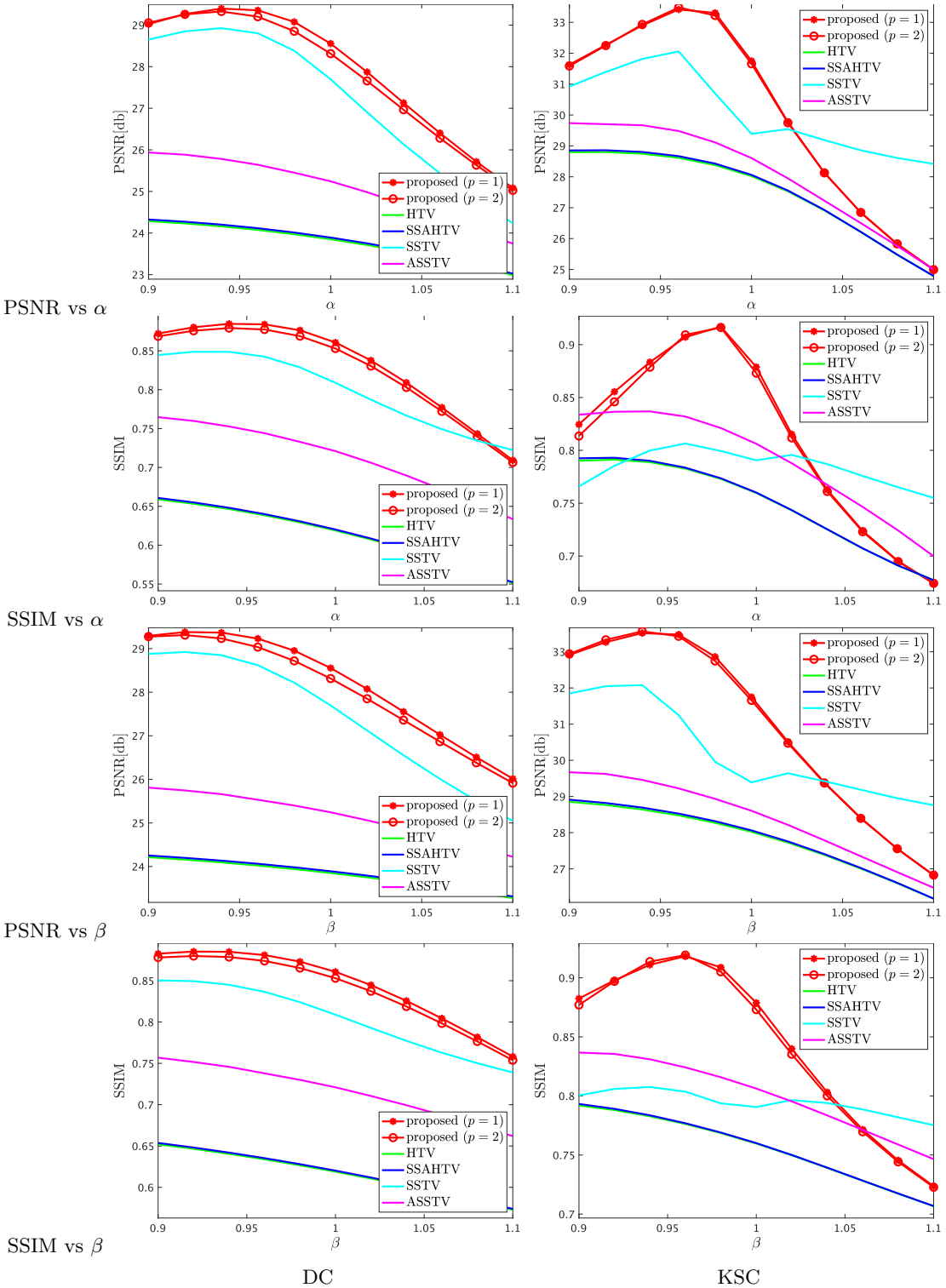

Figure 3.9: PSNR[dB] or SSIM versus α or β on the mixed noise removal experiment (the noise level (ii), left: DC, right: KSC).

and spectral information without artifacts.

Fig. 3.7 plots band-wise PSNR and SSIM (top), and spatial and spectral responses (bottom) of the denoised *Suwannee* HS image in the case of the noise level (ii). The graphs regarding band-wise PSNR and SSIM show that the proposed method achieves higher-quality restoration than HTV, SSAHTV, and SSTV for all bands and ASSTV and LRMR for most bands. Besides, even though the proposed method only utilizes HSSTV, the results by the proposed method outperform those by LRTV for some bands of the SSIM case and those by LLRGTV for many bands. Graph (c) plots the spatial response of the 243rd row of the 30th band. Similarly, graph (d) plots the spectral response of the 243rd row and 107th col. We can see that the spatial response of the results by HTV and SSAHTV is too smooth compared with the ground-truth one. On the other hand, there exist undesirable variations in the spatial response of the results by SSTV, LRMR, and LLRGTV. In contrast, ASSTV, LRTV, and the proposed method restore similar responses to the ground-truth one. In graph (d), one can see that (i) HTV, SSAHTV, and LRMR produce spectral artifacts, (ii) the shape of the spectral responses of the results by SSTV is similar to that of the ground-truth one, but the mean value is larger than the ground-truth one, (iii) the spectral response of the results by ASSTV is too smooth and different from the ground-truth one, and (iv) LRTV, LLRGTV, and the proposed method can restore a spectral response very similar to the ground-truth one.

To search the suitable ω in (3.6), we changed ω between 0.01 and 0.2 at 0.01 intervals. Fig. 3.8 plots PSNR or SSIM of the results by the proposed method versus various ω. Here, the values of PSNR and SSIM are averaged over the 13 HS images. One can see that $\omega \in [0.03,\ 0.07]$ is a good choice. The results show that the suitable ω in the mixed noise removal experiments is a little smaller than that in the Gaussian noise removal experiments, and the proposed method can achieve high quality denoising regardless of noise type if one set $\omega \in [0.05,\ 0.07]$. ASSTV and LRTV require adjusting the weight τ_b and the hyperparameter τ newly for difference noise intensity, respectively, but the suitable parameter ω in HSSTV is noise-robust.

To verify the sensitivity of the parameter ε and η in Prob. (3.8), we conducted additional mixed noise removal experiments, where we examined various values of ε and η. Specifically, we set $\varepsilon = 0.83\alpha\sqrt{NB(1-(s_p(1-l_v-l_h)+l_v+l_h-l_vl_h))\sigma^2}$ and $\eta = \beta NB(0.45s_p+(l_v+l_h)v_{ave}-l_vl_hv_{ave})$, which are hand-optimized values of the parameters and changed α and β from 0.9 to 1.1 at 0.02 interval (the *DC* and the *KSC* images and the noise level (ii)). Fig. 3.9 plots PSNR or SSIM of the results by HTV, SSAHTV, SSTV, ASSTV, and the proposed method versus α or β. For HTV, SSAHTV, ASSTV, and the proposed method, the graphs show that the suitable values of α and β do not vary significantly for both image, so the parameters ε and η are independent of both a regularization technique and an observed image. In the SSTV cases, the shapes of the plots are different between KSC and DC. This is because in the DC case, SSTV converges for all parameter settings, while in the case of KSC, it does not converge when $\alpha, \beta > 1$.

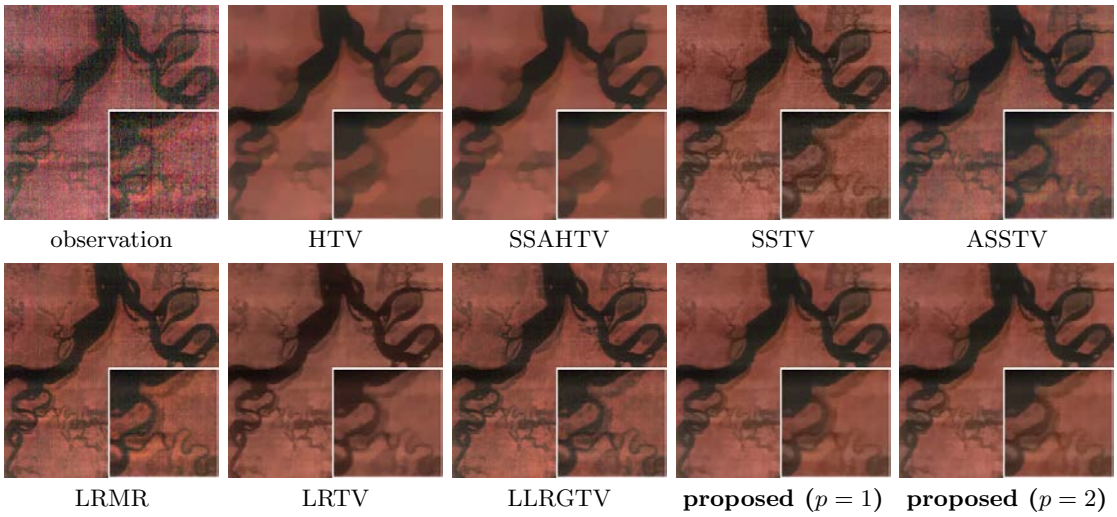

Figure 3.10: The denoising results on the real noise removal experiments.

Real Noise Removal

We illustrated the performance of the proposed method for real noise removal. In the experiments, we restore a desirable HS image from an observation with real noise by the proposed mixed noise removal method. We selected noisy 16 bands from *Suwannee* and used it as a real observed HS image $\mathbf{v}$. To maximize the performance of each method, we searched for suitable values of σ, s_p, l_v, and l_h. We also compared the proposed method with HTV, SSAHTV, SSTV, ASSTV, LRMR, LRTV, and LLRGTV. We set the parameter $\varepsilon = 3.1893$ and $\eta = 31893$ for all TVs. Besides, the parameters τ_v, τ_h, and τ_b in ASSTV are set as 1, 1, 3, respectively, r and k in LRMR are set as 3 and 0.1204, respectively, r and tau in LRTV are set as 2 and 0.008, and r, λ, and τ in LLRGTV are set as 2, 0.1 and 0.01.

Fig. 3.10 shows the results, where the HS images are depicted as RGB images (R = 2nd, G = 6th, and B = 13rd bands). The results by HTV and SSAHTV have spatial over-smoothing, and SSTV, ASSTV, LRMR, and LLRGTV produce spatial artifacts. Besides, one can see that the results by LRMR and LRTV have spectral artifacts. On the other hand, the proposed method can restore a detail-preserved HS image without artifacts.

3.2 Compressed Sensing Reconstruction

Multichannel images with the large number of bands have high-resolution 1D spectral and 2D spatial information, i.e., HS or multispectral (MS) images. The imaging requires a 2D spectral sensor for capturing 1D spatial information, and thus it is impossible to capture the images in real-time. To resolve the above problem, CS reconstruction plays a very important role [49–51]. The CS theory said that a high-dimensional signal can be reconstructed from a much fewer number of random observations by leveraging the sparsity of the signal, and so one-shot multichannel imaging based on CS is actively

studied [52, 53]. Therefore, the CS theory requires a robust reconstruction method to noise and outliers.

In this section, we focus on CS methods for an HS image. This is because HS images have the huge number of bands in multichannel image, and CS is essential technique for real-time HS imaging. CS reconstruction can be considered as the one of the image restoration method, and most CS methods are based on optimization. The reconstruction problems mainly consists of a regularization and a data-fidelity terms. As like with the denoising methods, the regularization techniques play an important role for the improvement of the CS performance. Besides, many CS methods for HS images [54–57] assume that observation is contaminated by only Gaussian noise, but optical systems often cause the other type of noise and/or outliers.

Based on the above discussion, we propose a new robust CS method to noise and outliers. Specifically, the method estimates a desirable HS image by solving optimization problem, which evaluates noise and outliers by multiple constraints and utilizes HSSTV as regularization. To efficiently solving the problem, we also provide an iterative solver based on a primal-dual splitting method [17]. In the experiments, we illustrate the utility of the proposed framework.

3.2.1 CS Reconstruction under Gaussian Noise Situation

Problem Formulation

Consider to restore an clean HS image $\bar{\mathbf{u}} \in \mathbb{R}^{NB}$ from an observation $\mathbf{v} \in \mathbb{R}^{M}$, which is cast as inverse problems of the form:

$$\mathbf{v} = \mathbf{\Phi}\bar{\mathbf{u}} + \mathbf{n}, \tag{3.13}$$

where $\mathbf{\Phi} \in \mathbb{R}^{M \times NB}$ $(M \leq NB)$ is a sensing matrix, e.g., random sampling, $\mathbf{n}$ is an additive white Gaussian noise with the standard deviation σ.

Based on the above model, we newly formulate compressed HS image reconstruction as the following convex optimization problem:

$$\min_{\mathbf{u}} \mathrm{HSSTV}(\mathbf{u}) \text{ s.t. } \left[\begin{array}{l} \mathbf{\Phi u} \in \mathcal{B}^{\mathbf{v}}_{2,\varepsilon} := \{\mathbf{x} \in \mathbb{R}^{M} | \|\mathbf{x} - \mathbf{v}\| \leq \varepsilon\}, \\ \mathbf{u} \in [\underline{\mu_{\mathbf{u}}}, \overline{\mu_{\mathbf{u}}}]^{NB}. \end{array} \right. \tag{3.14}$$

The first term in (3.14) is a regularization function for HS image restoration. HSSTV simultaneously evaluates spatio-spectral piecewise-smoothness and direct spatial piecewise-smoothness, and we explain HSSTV in Sec. 3.1.2. The first constraint in (3.14) serve as data-fidelity regarding Gaussian noise to the observation $\mathbf{v}$, and $\mathcal{B}^{\mathbf{v}}_{2,\varepsilon}$ is the $\mathbf{v}$-centered ℓ_2-norm ball with the radius ε. The second constraint in (3.14) is the dynamic range of $\mathbf{u}$ $(\underline{\mu_{\mathbf{u}}} < \overline{\mu_{\mathbf{u}}})$.

Algorithm 2: ADMM method for Prob. (3.14)

input : $\mathbf{z}_1^{(0)}, \mathbf{z}_2^{(0)}, \mathbf{z}_3^{(0)}, \mathbf{d}_1^{(0)}, \mathbf{d}_2^{(0)}, \mathbf{d}_3^{(0)}$

while *A stopping criterion is not satisfied* **do**

$\mathbf{u}^{(n+1)} = \underset{\mathbf{u}}{\operatorname{argmin}} \frac{1}{2\gamma}(\|\mathbf{z}_1^{(n)} - \mathbf{A}_\omega\mathbf{u} - \mathbf{d}_1^{(n)}\|^2 + \|\mathbf{z}_2^{(n)} - \mathbf{\Phi}\mathbf{u} - \mathbf{d}_2^{(n)}\|^2 + \|\mathbf{z}_3^{(n)} - \mathbf{u} - \mathbf{d}_3^{(n)}\|^2)$;

$\mathbf{z}_1^{(n+1)} = \operatorname{prox}_{\gamma\|\cdot\|_{1,p}}(\mathbf{A}_\omega\mathbf{u}^{(n+1)} + \mathbf{d}_1^{(n)})$;

$\mathbf{z}_2^{(n+1)} = \operatorname{prox}_{\gamma\iota_{\mathcal{B}_{2,\varepsilon}^{\mathbf{v}}}}(\mathbf{\Phi}\mathbf{u}^{(n+1)} + \mathbf{d}_2^{(n)})$;

$\mathbf{z}_3^{(n+1)} = \operatorname{prox}_{\gamma\iota_{[\underline{\mu_{\mathbf{u}}},\overline{\mu_{\mathbf{u}}}]^{NB}}}(\mathbf{u}^{(n+1)} + \mathbf{d}_3^{(n)})$;

$\mathbf{d}_1^{(n+1)} = \mathbf{d}_1^{(n)} + \mathbf{A}_\omega\mathbf{u}^{(n+1)} - \mathbf{z}_1^{(n+1)}$;

$\mathbf{d}_2^{(n+1)} = \mathbf{d}_2^{(n)} + \mathbf{\Phi}\mathbf{u}^{(n+1)} - \mathbf{z}_2^{(n+1)}$;

$\mathbf{d}_3^{(n+1)} = \mathbf{d}_3^{(n)} + \mathbf{u}^{(n+1)} - \mathbf{z}_3^{(n+1)}$;

$n \leftarrow n + 1$;

Optimization

We solve Sec. (3.14) by ADMM. To solve it ADMM, we reformulate Prob. (3.14) into Prob. (2.7) like Sec. 3.1.2. By letting

$$f : \mathbb{R}^{NB} \to \mathbb{R} : \mathbf{u} \mapsto 0, \tag{3.15}$$

$$g : \mathbb{R}^{5NB+M} \to \mathbb{R} \cup \{\infty\} : (\mathbf{z}_1, \mathbf{z}_2, \mathbf{z}_3) \mapsto \|\mathbf{z}_1\|_{1,p} + \iota_{\mathcal{B}_{2,\varepsilon}^{\mathbf{v}}}(\mathbf{z}_2) + \iota_{[\underline{\mu_{\mathbf{u}}},\overline{\mu_{\mathbf{u}}}]^{NB}}(\mathbf{z}_3), \tag{3.16}$$

$$\mathbf{G} : \mathbb{R}^{NB} \to \mathbb{R}^{5NB+M} : \mathbf{u} \mapsto (\mathbf{A}_\omega\mathbf{u}, \mathbf{\Phi}\mathbf{u}, \mathbf{u}). \tag{3.17}$$

Prob. (3.14) is reduced to Prob. (2.7). The resulting algorithm based on ADMM is summarized in Alg. 2.

The update of $\mathbf{u}$ in Alg. 2 comes down to the following forms:

$$\begin{aligned}\mathbf{u}^{(n+1)} &= \left(\mathbf{A}_\omega^\top\mathbf{A}_\omega + \mathbf{\Phi}^\top\mathbf{\Phi} + \mathbf{I}\right)^{-1}\mathrm{RHS},\\ \mathrm{RHS} &= \mathbf{A}_\omega^\top(\mathbf{z}_1^{(n)} - \mathbf{d}_1^{(n)}) + \mathbf{\Phi}^\top(\mathbf{z}_2^{(n)} - \mathbf{d}_2^{(n)}) + (\mathbf{z}_3^{(n)} - \mathbf{d}_3^{(n)})\end{aligned} \tag{3.18}$$

Since the update of $\mathbf{u}$ in Alg. 2 is strictly-convex quadratic minimization, one can obtain these updated forms by differentiating it.

Here, we should consider the structure of $\mathbf{\Phi}$ because it affects the matrix inversion in (3.18). If $\mathbf{\Phi}$ is a block-circulant-with-circulant-blocks (BCCB) matrix [58], we can leverage 3DFFT to efficiently solve the inversion in Step 2 with the difference operators having a periodic boundary, i.e., $\mathbf{A}_\omega^\top\mathbf{A}_\omega + \mathbf{\Phi}^\top\mathbf{\Phi} + \mathbf{I}$ can be diagonalized by the 3DFFT matrix and its inverse. If $\mathbf{\Phi}$ is a semiorthogonal matrix, i.e., $\mathbf{\Phi}\mathbf{\Phi}^\top = \alpha\mathbf{I}$ ($\alpha > 0$), we leave it to the update of $\mathbf{z}_2$, which means that we replace $\iota_{\mathcal{B}_{2,\varepsilon}^{\mathbf{v}}}$ by $\iota_{\mathcal{B}_{2,\varepsilon}^{\mathbf{v}}} \circ \mathbf{\Phi}$ in (3.16) and $\mathbf{\Phi}\mathbf{u}$ by $\mathbf{u}$ in (3.17). This is because the proximity operator of $\iota_{\mathcal{B}_{2,\varepsilon}^{\mathbf{v}}} \circ \mathbf{\Phi}$, in this case, can be computed by using [18, Table 1.1-x] as follows:

$$\operatorname{prox}_{\gamma\iota_{\mathcal{B}_{2,\varepsilon}^{\mathbf{v}}}\circ\mathbf{\Phi}}(\mathbf{x}) = \mathbf{x} + \alpha^{-1}\mathbf{\Phi}^\top(P_{\mathcal{B}_{2,\varepsilon}^{\mathbf{v}}}(\mathbf{\Phi}\mathbf{x}) - \mathbf{\Phi}\mathbf{x}).$$

If $\mathbf{\Phi}$ is a sparse matrix, we offer to use a preconditioned conjugate gradient method [59] for approximately solving the inversion or to apply primal-dual splitting methods [17, 60, 61] instead of ADMM. Here, primal-dual splitting methods require no matrix inversion but in general their convergence speed is slower than ADMM. Otherwise, randomized image restoration methods using stochastic proximal splitting algorithms [62–65] might be useful for reducing the computational cost.

For the update of $\mathbf{z}_1$, the proximity operators are reduced to simple soft-thresholding type operations described in Sec. 2.1. The updates of $\mathbf{z}_2$ and $\mathbf{z}_3$ use the proximity operators of the indicator functions of each set, i.e., (2.4) and (2.6), respectively.

Experiments

We experimented on CS reconstruction under Gaussian noise situation. In this experiment, we generate an observation based on (3.13) and reconstruct a desirable HS image from it. For test HS images, we took 13 HS images as like the Gaussian noise removal experiment. We assume that $\mathbf{\Phi} \in \mathbb{R}^{M \times NB}$ in (3.13) is a random sampling matrix with the sampling rate m ($0 < m < 1$ and $M = mNB$). Here, since $\mathbf{\Phi}$ is a semiorthogonal matrix, we can efficiently solve the problem, as explained in the optimization section. We set the standard deviation of Gaussian noise σ as 0.1 and the sampling rate m of $\mathbf{\Phi}$ as 0.2 or 0.4.

The proposed method was compared with HTV, SSAHTV, SSTV, and ASSTV. For fair comparison, we replaced HSSTV in Prob. (3.14) with the TVs and solved the problem by ADMM. In the ASSTV case, we set the parameters $(\tau_v, \tau_h, \tau_b) = (1, 1, 0.5)$, which experimentally achieves the best performance. We set the hyperparameter $\varepsilon = \sqrt{mNB\sigma^2}$ in (3.14), and ω in (3.6) is set to 0.08/0.06 in the $\ell_1/\ell_{1,2}$-HSSTV case, respectively.

Tab. 3.6 shows PSNR and SSIM of the reconstructed HS images. For all m and HS images, both PSNR and SSIM of the proposed method results are almost higher than that by HTV, SSAHTV, SSTV, and ASSTV.

Fig. 3.11 is the reconstructed results on *KSC* and *Reno* with the random sampling ratio $m = 0.4$ and 0.2, respectively. Here, the HS images are depicted as RGB images (R = 8th, G = 16th, and B = 32nd bands). One can see that (i) HTV and SSAHTV cause spatial oversmoothing, (ii) SSTV produces artifacts and spectral distortion, appearing different from the color of the ground-truth HS images, and (iii) the results by ASSTV have spatial oversmoothing and spectral distortion. On the other hand, the proposed method reconstructs meaningful details without both artifacts and spectral distortion.

Fig. 3.12 plots band-wise PSNR or SSIM (left) and spatial and spectral responses (right) (*Suwannee*, $m = 0.2$). According to band-wise PSNR and SSIM, one can see that the proposed method achieves higher-quality reconstruction for all bands than HTV, SSAHTV, SSTV, and ASSTV. Graphs (c) and (d) plot the spatial and spectral responses of the same position in the denoising experiments. Graph (c) shows that (i) the spatial response of the results by HTV, SSAHTV, and ASSTV are oversmoothing, (ii) SSTV produces undesirable variation, and (iii) the spatial response reconstructed by the proposed method is similar to the ground-truth one. In graph (d), HTV and SSAHTV generate undesirable variation, and ASSTV causes oversmoothing. Thanks to the evaluation of

Table 3.6: PSNR[dB] (top) and SSIM (bottom) in the CS reconstruction experiment under Gaussian noise situation.

	HS image	m	HTV	SSAHTV	SSTV	ASSTV	**Proposed ($p=1$)**	**Proposed ($p=2$)**
PSNR	Beltsville	0.4	27.46	27.49	27.53	26.51	**31.15**	30.71
		0.2	26.23	26.25	24.34	24.12	**29.63**	29.18
	Suwannee	0.4	27.97	28.02	28.49	27.68	32.98	**33.04**
		0.2	26.47	26.50	25.69	25.39	31.37	**31.44**
	DC	0.4	24.69	24.73	27.33	24.71	**29.70**	29.29
		0.2	23.31	23.33	24.16	22.69	**27.98**	27.59
	Cuprite	0.4	29.94	29.96	28.21	28.59	**34.36**	34.34
		0.2	28.77	28.77	25.79	26.38	**32.97**	32.95
	Reno	0.4	26.99	27.05	27.82	26.49	**31.80**	31.61
		0.2	25.57	25.61	25.57	24.52	**30.22**	30.04
	Botswana	0.4	26.10	26.15	27.81	25.13	**30.32**	30.15
		0.2	24.66	24.69	24.79	22.86	**28.79**	28.63
	IndianPines	0.4	30.54	30.55	27.65	29.55	**31.36**	31.04
		0.2	29.99	29.99	25.11	28.19	**30.71**	30.46
	KSC	0.4	29.30	29.33	28.34	28.63	**34.10**	34.03
		0.2	28.11	28.12	27.00	26.59	**32.67**	32.60
	PaviaLeft	0.4	25.66	25.69	29.66	25.41	**31.96**	31.83
		0.2	24.26	24.27	27.17	23.24	**30.20**	30.08
	PaviaRight	0.4	25.83	25.85	29.86	25.61	**32.45**	32.21
		0.2	24.30	24.30	27.54	23.61	**30.56**	30.38
	PaviaU	0.4	26.49	26.53	30.02	26.38	**32.88**	32.70
		0.2	24.95	24.97	27.35	24.08	**31.13**	30.96
	Salinas	0.4	31.19	31.24	27.69	30.18	35.43	**35.51**
		0.2	29.94	29.98	25.28	28.09	34.05	**34.10**
	SalinasA	0.4	30.67	30.82	27.93	28.19	**34.45**	34.14
		0.2	28.68	28.75	24.15	24.94	**32.71**	32.36
SSIM	Beltsville	0.4	0.6829	0.6940	0.6013	0.6836	**0.8105**	0.7948
		0.2	0.6363	0.6493	0.4348	0.6108	**0.7604**	0.7427
	Suwannee	0.4	0.7332	0.7497	0.7377	0.7367	0.8902	**0.8909**
		0.2	0.6810	0.7007	0.5739	0.6633	0.8531	**0.8534**
	DC	0.4	0.6096	0.6242	0.7522	0.6245	**0.8577**	0.8460
		0.2	0.5215	0.5384	0.6120	0.5037	**0.7970**	0.7846
	Cuprite	0.4	0.7665	0.7804	0.6826	0.7652	0.8882	**0.8895**
		0.2	0.7368	0.7525	0.5057	0.7207	0.8568	**0.8578**
	Reno	0.4	0.6769	0.6868	0.7414	0.6730	**0.8733**	0.8705
		0.2	0.6202	0.6326	0.6276	0.5940	**0.8263**	0.8228
	Botswana	0.4	0.6683	0.6803	0.7551	0.6460	0.8563	**0.8598**
		0.2	0.6014	0.6162	0.6225	0.5519	0.8119	**0.8163**
	IndianPines	0.4	0.7497	0.7777	0.5066	0.7617	**0.7806**	0.7655
		0.2	0.7366	**0.7658**	0.3488	0.7465	0.7589	0.7491
	KSC	0.4	0.7660	0.7742	0.6814	0.7544	**0.9019**	0.9002
		0.2	0.7318	0.7410	0.6008	0.7032	**0.8698**	0.8679
	PaviaLeft	0.4	0.6082	0.6205	0.8386	0.5932	**0.8900**	0.8857
		0.2	0.5103	0.5251	0.7319	0.4434	**0.8418**	0.8364
	PaviaRight	0.4	0.6357	0.6423	0.7962	0.6275	**0.8937**	0.8877
		0.2	0.5502	0.5584	0.6917	0.5069	**0.8475**	0.8392
	PaviaU	0.4	0.6867	0.6956	0.7830	0.6818	**0.8950**	0.8901
		0.2	0.6138	0.6242	0.6623	0.5680	**0.8557**	0.8508
	Salinas	0.4	0.8577	0.8672	0.6153	0.8566	0.9222	**0.9245**
		0.2	0.8404	0.8516	0.4620	0.8302	0.9052	**0.9080**
	SalinasA	0.4	0.8647	0.8871	0.6595	0.8489	0.9178	**0.9208**
		0.2	0.8387	0.8655	0.4810	0.8005	0.8966	**0.9002**

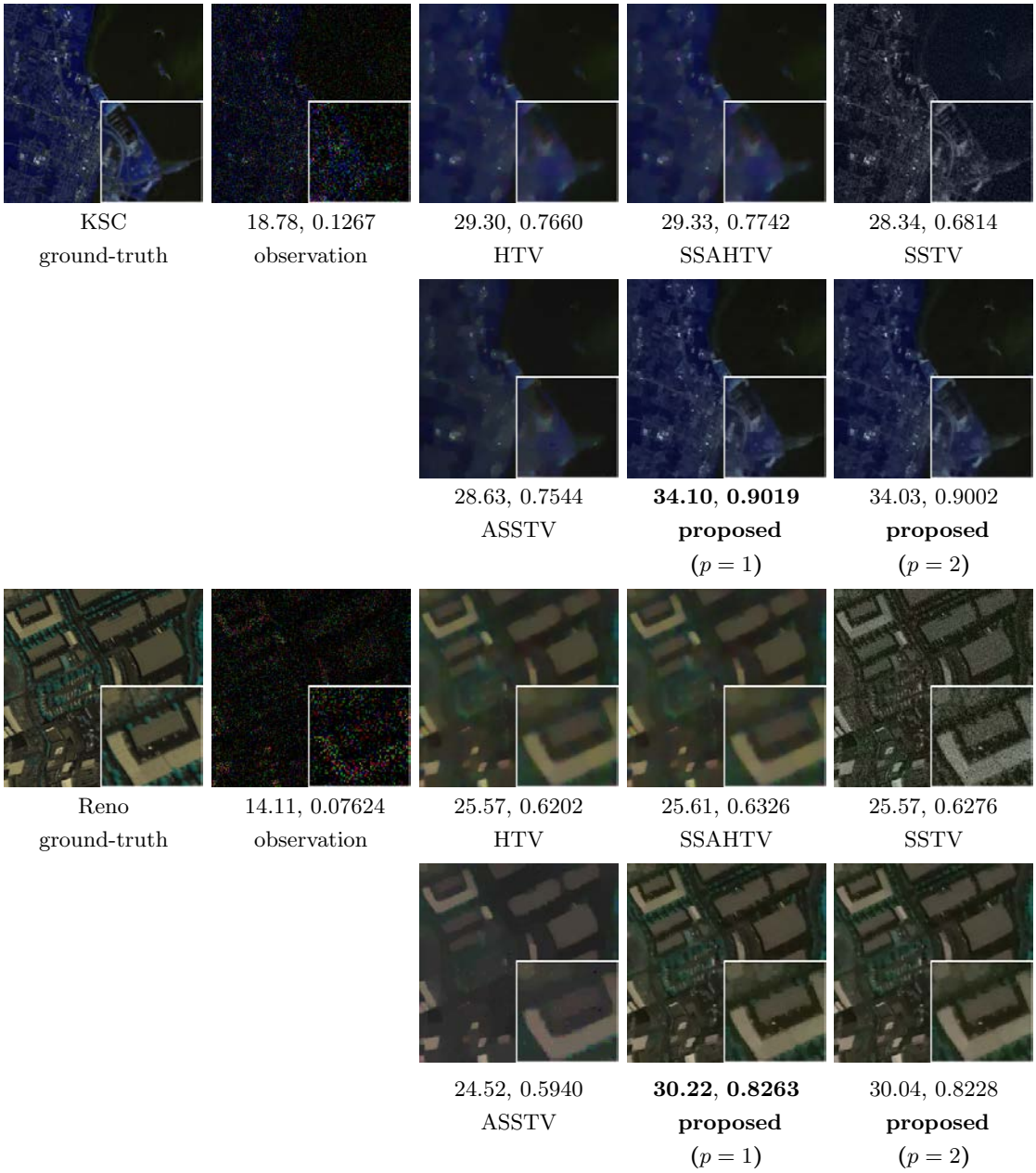

Figure 3.11: Resulting HS images with their PSNR[dB] (left) and SSIM (right) on the CS reconstruction experiment under Gaussian noise situation (top: KSC, $m = 0.4$, bottom: Reno, $m = 0.2$).

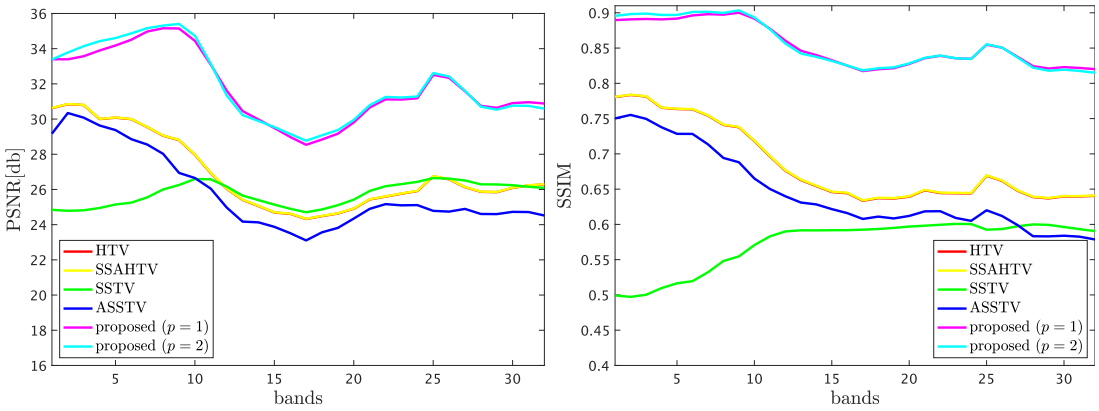

(**a**) band-wise PSNR

(**b**) band-wise SSIM

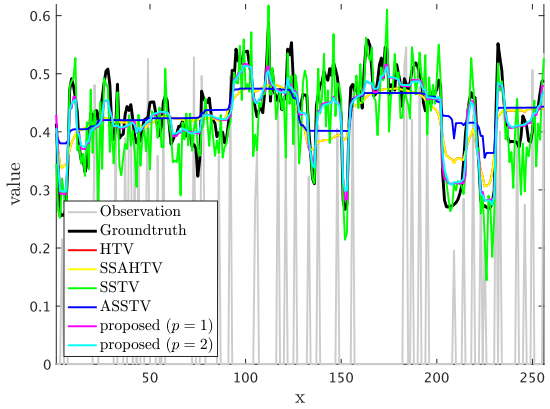

(**c**) Spatial response

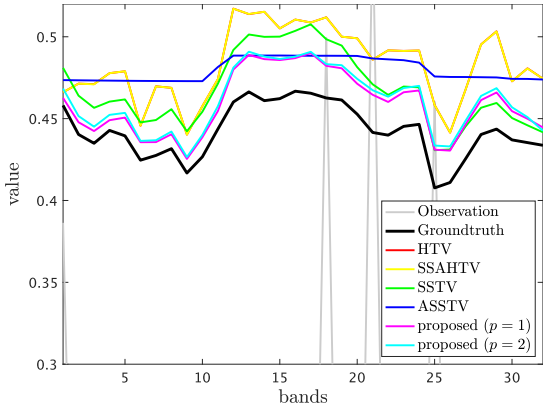

(**d**) Spectral response

Figure 3.12: Band-wise PSNR[dB] and SSIM and spatial and spectral responses on the CS reconstruction experiment under Gaussian noise situation (Suwannee).

spatio-spectral piecewise-smoothness, SSTV reconstructs a similar spectral response to the ground-truth one. However, the mean value is larger than the ground-truth value. The proposed method achieves the most similar reconstruction of spectral response among all the TVs.

To search the suitable ω in (3.6), we changed ω between 0.01 and 0.2 at 0.01 intervals. Fig. 3.13 plots PSNR or SSIM of the results by the proposed method versus various ω, where the values of PSNR and SSIM are averaged over the 13 HS images. One can see that $\omega \in [0.05, 0.1]$ is a good choice in most cases. The results show that the suitable range of ω in CS reconstruction is the same as Gaussian noise removal.

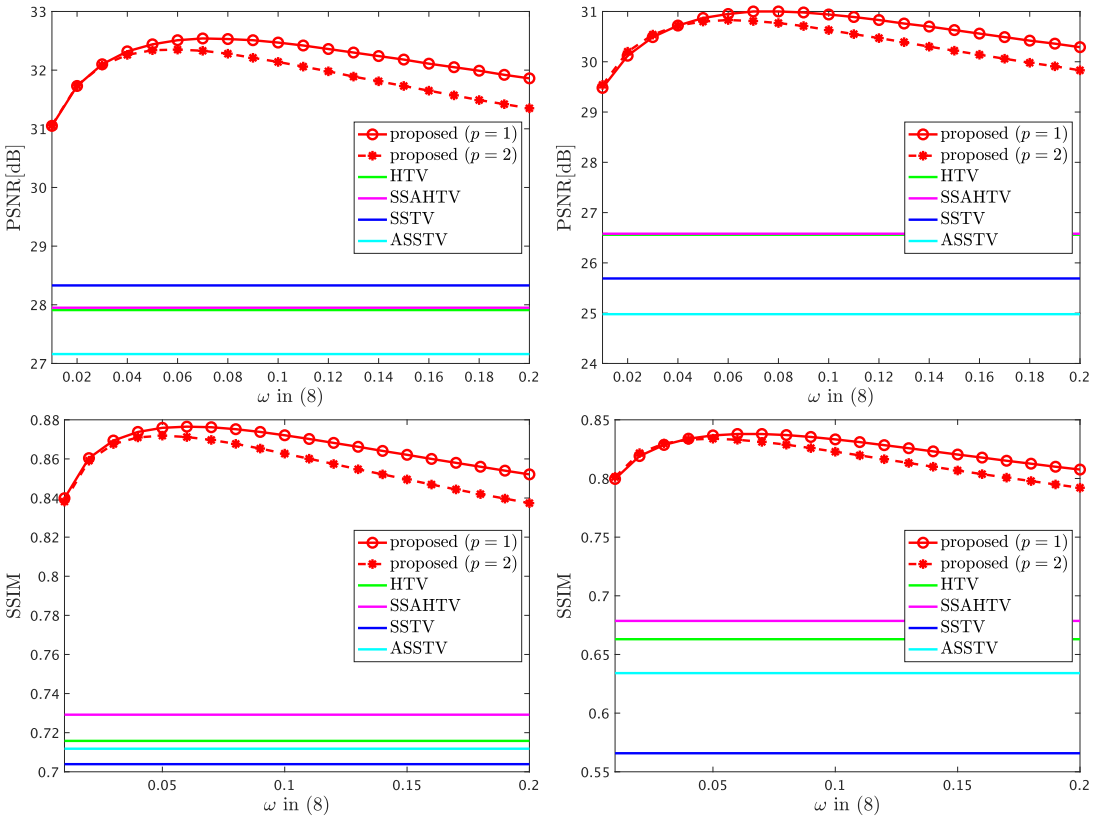

$m = 0.4$ $m = 0.2$

Figure 3.13: PSNR[dB] (top) or SSIM (bottom) versus ω in (3.6) on the CS reconstruction experiment under Gaussian noise situation.

3.2.2 CS Reconstruction under Mixed Noise Situation

Problem Formulation

To consider to CS reconstruction under mixed noise situation, we model the observation $\mathbf{v} \in \mathbb{R}^M$ as follows:

$$\mathbf{v} = \mathbf{\Phi}\bar{\mathbf{u}} + \mathbf{n} + \mathbf{s}. \tag{3.19}$$

Based on the above model, we newly formulate compressed HS image reconstruction considering mixed noise as the following convex optimization problem:

$$\min_{\mathbf{u},\mathbf{s}} \mathrm{HSSTV}(\mathbf{u}) \text{ s.t. } \begin{bmatrix} \mathbf{\Phi u} + \mathbf{s} \in \mathcal{B}^{\mathbf{v}}_{2,\varepsilon} := \{\mathbf{x} \in \mathbb{R}^M | \|\mathbf{x} - \mathbf{v}\| \leq \varepsilon\}, \\ \mathbf{s} \in \mathcal{B}_{1,\eta} := \{\mathbf{x} \in \mathbb{R}^M | \|\mathbf{x}\|_1 \leq \eta\}, \\ \mathbf{u} \in [\underline{\mu_{\mathbf{u}}}, \overline{\mu_{\mathbf{u}}}]^{NB}. \end{bmatrix} \tag{3.20}$$

The first term in (3.20) is a regularization function for HS image restoration as defined in Sec. 3.1.2. The first and second constraints in (3.20) serve as data-fidelity regarding Gaussian and sparse noise to the observation $\mathbf{v}$, respectively. The first constraint set $\mathcal{B}^{\mathbf{v}}_{2,\varepsilon}$

Algorithm 3: Primal-dual splitting method for Prob. (3.20)

input : $\mathbf{u}^{(0)}$, $\mathbf{s}^{(0)}$, $\mathbf{y}_1^{(0)}$, $\mathbf{y}_2^{(0)}$, $\mathbf{y}_3^{(0)}$,$\mathbf{y}_4^{(0)}$, γ_1, γ_2

while *A stopping criterion is not satisfied* **do**

$\mathbf{u}^{(n+1)} = \mathbf{u}^{(n)} - \gamma_1(\mathbf{A}_\omega^\top \mathbf{y}_1 + \mathbf{\Phi}^\top \mathbf{y}_2 + \mathbf{y}_4)$;

$\mathbf{s}^{(n+1)} = \mathbf{s}^{(n)} - \gamma_1(\mathbf{y}_2 + \mathbf{y}_3)$;

$\mathbf{y}_1^{(n)} \leftarrow \mathbf{y}_1^{(n)} + \gamma_2 \mathbf{A}_\omega(2\mathbf{u}^{(n+1)} - \mathbf{u}^{(n)})$;

$\mathbf{y}_2^{(n)} \leftarrow \mathbf{y}_2^{(n)} + \gamma_2(\mathbf{\Phi}(2\mathbf{u}^{(n+1)} - \mathbf{u}^{(n)}) + (2\mathbf{s}^{(n+1)} - \mathbf{s}^{(n)}))$;

$\mathbf{y}_3^{(n)} \leftarrow \mathbf{y}_3^{(n)} + \gamma_2(2\mathbf{s}^{(n+1)} - \mathbf{s}^{(n)})$;

$\mathbf{y}_4^{(n)} \leftarrow \mathbf{y}_4^{(n)} + \gamma_2(2\mathbf{u}^{(n+1)} - \mathbf{u}^{(n)})$;

$\mathbf{y}_1^{(n+1)} = \mathbf{y}_1^{(n)} - \gamma_2 \operatorname{prox}_{\frac{1}{\gamma_2}\|\cdot\|_{1,p}}\left(\frac{\mathbf{y}_1^{(n)}}{\gamma_2}\right)$;

$\mathbf{y}_2^{(n+1)} = \mathbf{y}_2^{(n)} - \gamma_2 \operatorname{prox}_{\frac{1}{\gamma_2}\iota_{\mathcal{B}_{2,\varepsilon}^{\mathbf{v}}}}\left(\frac{\mathbf{y}_2^{(n)}}{\gamma_2}\right)$;

$\mathbf{y}_3^{(n+1)} = \mathbf{y}_3^{(n)} - \gamma_2 \operatorname{prox}_{\frac{1}{\gamma_2}\iota_{\mathcal{B}_{1,\eta}}}\left(\frac{\mathbf{y}_3^{(n)}}{\gamma_2}\right)$;

$\mathbf{y}_4^{(n+1)} = \mathbf{y}_4^{(n)} - \gamma_2 \operatorname{prox}_{\frac{1}{\gamma_2}\iota_{[\underline{\mu_\mathbf{u}},\overline{\mu_\mathbf{u}}]^{NB}}}\left(\frac{\mathbf{y}_4^{(n)}}{\gamma_2}\right)$;

$n \leftarrow n + 1$;

is the $\mathbf{v}$-centered ℓ_2-norm ball with the radius ε, and the second one is the $\mathbf{0}$-centered ℓ_1-norm ball with the radius η. The third constraint in (3.20) is the dynamic range of $\mathbf{u}$.

Optimization

In this part, we introduce an algorithm for solving Prob. (3.20). Since the problem is a highly nonsmooth convex optimization problem, we solve it by an iterative algorithm based on a primal-dual splitting method [17]. In Sec. 2.3, the primal-dual splitting method can solve convex optimization problems of the form of Prob. (2.9) by the algorithm (2.10), and then we reformulate Prob. (3.20) into Prob. (2.9).

We put the constraints in Prob. (3.20) in the objective function by the indicator functions. Then, Prob. (3.20) can be rewritten as follows:

$$\min_{\mathbf{u},\mathbf{s}} \|\mathbf{A}_\omega \mathbf{u}\|_{1,p} + \iota_{\mathcal{B}_{2,\varepsilon}^{\mathbf{v}}}(\mathbf{\Phi}\mathbf{u} + \mathbf{s}) + \iota_{\mathcal{B}_{1,\eta}}(\mathbf{s}) + \iota_{[\underline{\mu_\mathbf{u}},\overline{\mu_\mathbf{u}}]^{NB}}(\mathbf{u}). \tag{3.21}$$

Note that Prob. (3.21) is equivalent to Prob. (3.20) (there is no approximation) because of the definition of the indicator function. By letting

$$g : \mathbb{R}^{NB} \to \mathbb{R}^2 : (\mathbf{u}, \mathbf{s}) \mapsto \mathbf{0},$$

$$h : \mathbb{R}^{5NB+2M} \to \mathbb{R} \cup \{\infty\} : (\mathbf{z}_1, \mathbf{z}_2, \mathbf{z}_3, \mathbf{z}_4) \mapsto \|\mathbf{z}_1\|_{1,p} + \iota_{\mathcal{B}_{2,\varepsilon}^{\mathbf{v}}}(\mathbf{z}_2) + \iota_{\mathcal{B}_{1,\eta}}(\mathbf{z}_3) + \iota_{[\underline{\mu_\mathbf{u}},\overline{\mu_\mathbf{u}}]^{NB}}(\mathbf{z}_4),$$

$$\mathbf{L} : \mathbb{R}^{NB} \to \mathbb{R}^{5NB+2M} : (\mathbf{u}, \mathbf{s}) \mapsto (\mathbf{A}_\omega \mathbf{u}, \mathbf{\Phi}\mathbf{u} + \mathbf{s}, \mathbf{s}, \mathbf{u}),$$

Prob. (3.21) is reduced to Prob. (2.9). The resulting algorithm based on the primal-dual splitting method is summarized in Alg. 3 with (2.11).

For the update of $\mathbf{y}_1$, we use a simple soft-thresholding type operation (2.2) or (2.3). The update of $\mathbf{y}_2$, $\mathbf{y}_3$, and $\mathbf{y}_4$ can be calculated by (2.4), (2.5), and (2.6), respectively.

Table 3.7: The four quality measures of the results on CS reconstruction under mixed noise situation.

methods \ quality measures		PSNR[dB]	SAM	ERGAS	$Q2^n$
ℓ_2 fidelity constraint only	HTV [6]	23.78	7.477	28.04	0.2294
	SSTV [7]	24.33	5.229	24.65	0.3907
	ASSTV [22]	21.81	10.59	30.36	0.2829
	ℓ_1-HSSTV	28.72	4.177	16.07	0.5609
	$\ell_{1,2}$-HSSTV	28.40	4.237	16.97	0.5656
Proposed (ℓ_1 and ℓ_2 fidelity constraints)	HTV [6]	25.90	4.846	21.24	0.3689
	SSTV [7]	27.27	5.375	18.75	0.5878
	ASSTV [22]	26.12	6.649	19.30	0.3865
	ℓ_1-HSSTV	30.98	3.609	**12.34**	0.6726
	$\ell_{1,2}$-HSSTV	**31.03**	**3.608**	12.40	**0.6733**

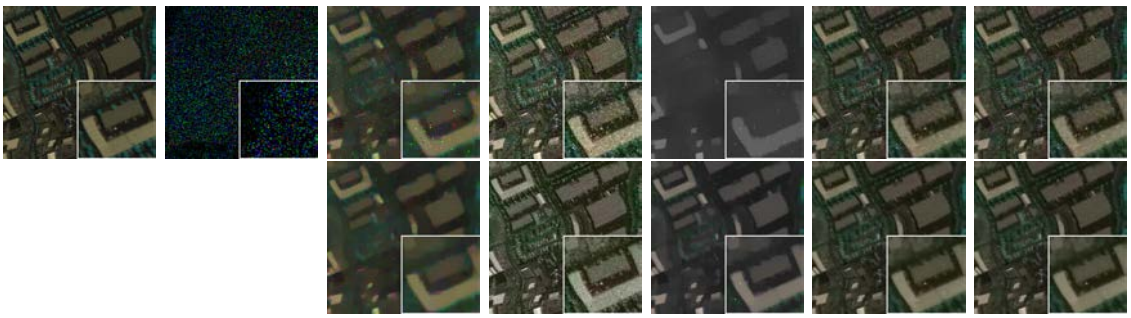

Figure 3.14: Resulting HS images on CS reconstruction under mixed noise situation (Reno, top: ℓ_2 fidelity constraint only, bottom: proposed).

Experiments

To verify the utility of the proposed framework, we conducted compressed HS reconstruction experiments under mixed Gaussian-sparse noise contamination. We examined various regularizations: HTV, SSTV, ASSTV, and our HSSTV.

In the experiments, we artificially generated an observation based on (3.19) and reconstructed a desirable HS image from it. The sensing matrix $\mathbf{\Phi}$ in (3.19) is assumed to be a random-sampling operator of ratio $m = 0.2$. We assumed that $\mathbf{n}$ is an additive white Gaussian noise with the standard deviation $\sigma = 0.05$, and $\mathbf{s}$ is a salt-and-peeper noise of ratio $s_p = 0.04$. For test HS images, we took five HS images from the *SpecTIR* [44] and *MultiSpec* [45], cropped a region of size $256 \times 256 \times 32$ for each HS image, and normalized their dynamic range into $[0, 1]$. The radiuses ε and η in Prob. (3.20) were set to $\sqrt{mNB(1-s_p)\sigma^2}$ and $0.5mNBs_p$, respectively.

We reconstruct a desirable HS image by solving Prob. 3.20 replacing HSSTV with HTV, SSTV, and ASSTV and set the parameters in ASSTV and HSSTV as $\tau_b = 4$ and $\omega = 0.04$, respectively. To verify the performance of the proposed framework, we compared our framework with the method considering only Gaussian noise, i.e., Prob. (3.14). In the above case, we set $\varepsilon = \sqrt{rNB((1-s_p)\sigma^2 + 0.25s_p)}$. To evaluate the quality of restored HS images, we used four quality measures: PSNR [dB], SAM [14], ERGAS [15], and $Q2^n$ [66]. We set the max iteration number and the stopping criterion of the primal-dual splitting method to 10000 and $\|\mathbf{u}^{(n)} - \mathbf{u}^{(n+1)}\|/\|\mathbf{u}^{(n+1)}\| < 1.0 \times 10^{-4}$, respectively.

Tab. 3.7 shows the values of the four quality measures of the results, which is the average of five HS images. The left of the table represents the results by the method considering only Gaussian noise, and the right is our framework. For most quality measures, one can see that considering mixed Gaussian-sparse noise improves reconstruction accuracy. Besides, HSSTV achieves the highest quality of all the regularizations.

In Fig 3.14, we show the reconstructed HS images (*Reno*) depicted as RGB images, where we choose $R = 8$th, $G = 16$th, and $B = 32$nd bands. One can see that our frameworks with $\ell_1/\ell_{1,2}$-HSSTV achieve the best performance.

Chapter 4

Image Fusion

4.1 Blur and Noisy Image Fusion

Image deblurring, removing blur from a given photograph, has been a fundamental and longstanding problem in image processing and computer vision. Many image deblurring methods, e.g., [67–75], are categolized as *single image blind deblurring*, that is, estimating both the blur kernel and the latent image from a single blurred image (for more infomation on single image blind deblurring, see a comprehensive survey [76]). Although single image blind deblurring assumes the most realistic situation, it is a very challenging task due to the highly under-costrained nature, so that it often leads to inaccurate estimation of blur kernels, high sensitivity to noise, and heavy dependence on prior information used.

To overcome the inherent difficulty, blind deblurring methods with a blurred/noisy image pair have been studied [77–81]. These methods consider such a situation that both images are captured in low light conditions with different settings. Specifically, the blurred image is taken with a slow shutter speed and a low ISO setting. With enough light, it has the correct color and intensity, but it is blurry due to camera shake. On the other hands, the noisy image is taken with a fast shutter speed and a high ISO setting. It is sharp but very noisy because of insufficient exposure and high camera gain. In addition, since it has low contrast, the colors of this image are also partially lost. Under this situation, existing methods take a two-step approach: first estimating the blur kernel from the image pair and then restoring a sharp image using the estimated kernel. Essentially, they can yield a better and much more stable result in their kernel estimation step than single image deblurring methods, since the difference between the two images is extremely informative for kernel estimation.

On the other hand, there exists a room for improvement in the image restoration step of these methods. Specifically, the methods [77–79] estimate the latent image based only on a given blurred image, i.e., do not exploit the information on a given noisy image in their image restoration step, so that they are sensitive to the estimation error of the blur kernel. In addition, if noise in the blurred image is not negligible, restoring a sharp image from it becomes difficult even when using the true kernel. Meanwhile, the methods [80,81] exploit the information on both images in their image restoration step. In these methods, the image restoration problem is formulated as the minimization of a regularization term,

reflecting prior information on the latent image, plus two data-fidelity terms, keeping the consistency to a blurred/noisy image pair, where the balance among these terms is controled by multiple weights. However, the tuning of such multiple weights is a tedious task because they are *interdependent* and have no physical meaning. Indeed, suitable values of them vary depending on the latent image and/or the regularization terms used.

Based on the above discussion, we propose a new image restoration method of using both a blurred image and a noisy image, which can be integrated into any blind deblurring methods with a blurred/noisy image pair. In our method, the image restoration problem is formulated as a constrained convex optimization problem: minimizing a (possibly nonsmooth) regularization function subject to multiple hard constraints. Two of the hard constraints correspond to data-fidelity to a blurred image and that to a noisy image, respectively, where the degree of fidelity to each image can be controlled by *independent* parameters that are explicitly related to the noise intensity of the image pair. We also prove the existence of an optimal solution of the problem under reasonable assumptions. Since our problem formulation properly incorporates the information on a blurred/noisy image pair, it achieves (i) high quality restoration when the blurred image also contains noise; and (ii) robustness to the estimation error of the blur kernel. At the same time, the independence and clear meaning of the parameters thanks to the hard constraints offer (iii) easy parameter setting.

Through several reformulations, we also provide an efficient algorithm with guaranteed convergence for solving the constrained convex optimization problem. Our algorithm is based on ADMM a celebrated optimization method based on proximal splitting.

4.1.1 Problem Formulation

Consider to estimate an unknown latent color image $\bar{\mathbf{u}} \in \mathbb{R}^{3N}$ (3 is the number of color channels) from an observed blurred image $\mathbf{v}_n \in \mathbb{R}^{3N}$ and an observed noisy image $\mathbf{v}_b \in \mathbb{R}^{3N}$. Specifically, following the prior work [80, 81] we model them as

$$\mathbf{v}_n = \mathbf{B}\bar{\mathbf{u}} + \mathbf{n}_n, \tag{4.1}$$

$$\mathbf{v}_b = \bar{\mathbf{u}} + \mathbf{n}_b, \tag{4.2}$$

where $\mathbf{B} \in \mathbb{R}^{3N\times 3N}$ is a blur operator estimated in advance, and $\mathbf{n}_n$ and $\mathbf{n}_b$ are additive white Gaussian noises with their standard deviations σ_n and σ_b, respectively. The model assumes that the blurred image $\mathbf{v}_n$ also contains noise (usually $\sigma_n < \sigma_b$), which is a realistic setting as addressed in [80, 82].

Based on the above observation models, we newly formulate a convex optimization problem with multiple hard constraints for image restoration using a blurred/noisy image pair as follows:

$$\min_{\mathbf{u}} \mathcal{R}(\mathbf{\Psi u}) \text{ s.t. } \left[\begin{array}{l} \mathbf{u} \in [0,255]^{3N}, \\ \mathbf{Bu} \in \mathcal{B}_{\mathbf{v}_n,\varepsilon_n} := \{\mathbf{x} \in \mathbb{R}^{3N} | \|\mathbf{x} - \mathbf{v}_n\| \le \varepsilon_n\}, \\ \mathbf{u} \in \mathcal{B}_{\mathbf{v}_b,\varepsilon_b} := \{\mathbf{x} \in \mathbb{R}^{3N} | \|\mathbf{x} - \mathbf{v}_b\| \le \varepsilon_b\}. \end{array}\right. \tag{4.3}$$

Here, $\mathcal{R} \circ \mathbf{\Psi} : \mathbb{R}^N \to (-\infty, \infty]$ is a regularization function ($\mathbf{\Psi} \in \mathbb{R}^{L\times 3N}, \mathcal{R} \in \Gamma_0(\mathbb{R}^L)$). We assume that the proximity operator of $\mathcal{R}$ (NOT $\mathcal{R} \circ \mathbf{\Psi}$) can be computed efficiently.

This assumption is essential in solving the problem by ADMM, as will be explained in an optimization section. The first constraint set $[0,255]^{3N} \subset \mathbb{R}^{3N}$ is the dynamic range of eight-bit color images. The second and third ones $\mathcal{B}_{\mathbf{v}_n,\varepsilon_n}, \mathcal{B}_{\mathbf{v}_b,\varepsilon_b} \subset \mathbb{R}^{3N}$ are ℓ_2-norm balls that represent data-fidelity to a blurred image $\mathbf{v}_n$ and that to a noisy image $\mathbf{v}_b$, respectively, where $\varepsilon_n \geq 0$ and $\varepsilon_b \geq 0$ are their radiuses determined based on the noise intensity (noise standard deviations) of $\mathbf{v}_n$ and $\mathbf{v}_b$.

Remark 1 (Design of regularization). TV [83] and its vectorial variants, e.g., [33, 84–87], are well-known edge-preserving regularizers for images, and they have been used in many deblurring methods. In this case, $\mathcal{R}$ is some norm, e.g., the ℓ_1 norm, the mixed $\ell_{1,2}$ norm or the nuclear norm, and $\mathbf{\Psi}$ is a discrete gradient operator. The proximity operators of such norms are computable (see, e.g., [18, 88]). Another well-known example is frame regularization relying on the sparsity of images in some transformed domain. In this case, $\mathcal{R}$ is the ℓ_1 norm, and $\mathbf{\Psi}$ is a frame analysis operator, e.g., wavelet [89] and curvelet [90]. More involved regularization, such as nonlocal regularization [91–93], regularization using learned operators [94, 95] and plug-and-play regularization [96, 97], can also be handled in our formulation by setting $\mathbf{\Psi}$ to the corresponding nonlocal/learned analysis operator.

Remark 2 (Benefits of incorporating data-fidelity as hard constraints). Since ε_n and ε_b, the radiuses of the ℓ_2-norm balls in (4.3), are directly related to the noise intensity (noise standard deviations) of a blurred image and a noisy image, respectively, one can determine their values with the help of existing noise level estimation methods. More importantly, these parameters can be determined (almost) independent of the latent image $\bar{\mathbf{u}}$ and the regularization function $\mathcal{R}\circ\mathbf{\Psi}$. This means that once finding suitable values of ε_n and ε_b for some noise intensity, they can be used for various types of latent images and regularization functions under the same noise intensity, which makes the setting of parameters on data-fidelity much easier than existing methods that requires the tuning of interdependent parameters (see the section of facilitation of parameter setting). Such benefits of hard constraints have also been addressed, for example, in [10, 36, 37, 39, 98–100].

The following statement is on the existence of a solution of Prob. (4.3)

Proposition 1. *Assume that the intersection of the constraint sets in* (4.3) *is nonempty, i.e.,*

$$S := [0,255]^{3N} \cap \mathbf{\Phi}\mathcal{B}_{\mathbf{v}_n,\varepsilon_n} \cap \mathcal{B}_{\mathbf{v}_b,\varepsilon_b} \neq \emptyset,$$

and that there exists some $\mathbf{x} \in S$ *such that* $\mathcal{R}(\mathbf{\Psi}\mathbf{x}) < \infty$. *Then, Prob.* (4.3) *has at least one optimal solution, i.e., the function* $\mathcal{R} \circ \mathbf{\Psi}$ *has a minimizer over* S.

Proof: Since $\mathcal{R} \circ \mathbf{\Psi} \in \Gamma_0(\mathbb{R}^{3N})$ and S is a bounded closed convex subset of $\mathbb{R}^{3N}$, the statement is a direct consequence of [101, Proposition 11.14]. □

4.1.2 Optimization

Since Prob. (4.3) is a highly nonsmooth constrained problem, we need suitable iterative optimization methods to solve it. In this paper, we adopt ADMM, reviewed in Sec. 2.2. In what follows, we reformulate Prob. (4.3) into the ADMM-applicable form, i.e., Prob. (2.7).

First, let us define the indicator functions (see Sec. 2.1) of the closed convex sets $[0,255]^{3N}$, $\mathcal{B}_{\mathbf{v}_n,\varepsilon_n}$ and $\mathcal{B}_{\mathbf{v}_b,\varepsilon_b}$. Then, Prob. (4.3) can be rewritten as

$$\min_{\mathbf{u}} \mathcal{R}(\mathbf{\Psi u}) + \iota_{[0,255]^{3N}}(\mathbf{u}) + \iota_{\mathcal{B}_{\mathbf{v}_n,\varepsilon_n}}(\mathbf{Bu}) + \iota_{\mathcal{B}_{\mathbf{v}_b,\varepsilon_b}}(\mathbf{u}). \tag{4.4}$$

Second, we replace the input variables of all the terms in (4.4) with auxiliary variables $\mathbf{z}_1, \ldots, \mathbf{z}_4$, and express the relation between the input and the auxiliary variables by linear equality constraints, yielding

$$\begin{aligned} \min_{\mathbf{u}} \mathcal{R}(\mathbf{z}_1) + \iota_{[0,255]^{3N}}(\mathbf{z}_2) + \iota_{\mathcal{B}_{\mathbf{v}_n,\varepsilon_n}}(\mathbf{z}_3) + \iota_{\mathcal{B}_{\mathbf{v}_b,\varepsilon_b}}(\mathbf{z}_4) \\ \text{s.t.} \quad \mathbf{z}_1 = \mathbf{\Psi u},\ \mathbf{z}_2 = \mathbf{u},\ \mathbf{z}_3 = \mathbf{\Phi u},\ \mathbf{z}_4 = \mathbf{u}. \end{aligned} \tag{4.5}$$

Third, we define

$$g(\mathbf{z}_1, \ldots, \mathbf{z}_4) := \mathcal{R}(\mathbf{z}_1) + \iota_{[0,255]^{3N}}(\mathbf{z}_2) + \iota_{\mathcal{B}_{\mathbf{v}_n,\varepsilon_n}}(\mathbf{z}_3) + \iota_{\mathcal{B}_{\mathbf{v}_b,\varepsilon_b}}(\mathbf{z}_4).$$

Then, the function g becomes proximable thanks to the variable splitting, as long as each term of g is proximable. Indeed, $\mathcal{R}$ is proximable from the assumption, and the other terms, the three indicator functions, are also proximable because the metric projections onto the corresponding closed convex sets are available (see Sec. 2.1).

Finally, by letting $\mathbf{I}$ be the identity matrix of size $3N \times 3N$ and defining

$$f(\mathbf{u}) := 0 \quad \text{and} \quad \mathbf{G} := \begin{pmatrix} \mathbf{\Psi} \\ \mathbf{I} \\ \mathbf{B} \\ \mathbf{I} \end{pmatrix}, \tag{4.6}$$

Prob. (4.5) is reduced to Prob. (2.7).

The resulting algorithm based on ADMM is summarized in Alg. 4. Since $\mathbf{G}$ in (4.6) is a full column rank matrix due to $\mathbf{I}$, $\mathbf{G}^\top\mathbf{G}$ is invertible, so that the convergence of Alg. 4 is guaranteed if a saddle point of $g(\mathbf{z}) - \langle \mathbf{d}, \mathbf{Gu} - \mathbf{z} \rangle$ exists.

Now we discuss the computation of each step of Alg 4. Since the update of $\mathbf{u}$ (Step 2) is strictly-convex quadratic minimization because of the full-column-rankness of $\mathbf{G}$, it boils down to solving the following matrix inversion:

$$\begin{aligned} \mathbf{u}^{(n+1)} =& (\mathbf{\Psi}^\top\mathbf{\Psi} + \mathbf{B}^\top\mathbf{B} + 2\mathbf{I})^{-1}\mathrm{RHS} \\ \mathrm{RHS} :=& (\mathbf{\Psi}^\top(\mathbf{z}_1^{(n)} - \mathbf{d}_1^{(n)}) + (\mathbf{z}_2^{(n)} - \mathbf{d}_2^{(n)}) + \mathbf{B}^\top(\mathbf{z}_3^{(n)} - \mathbf{d}_3^{(n)}) + (\mathbf{z}_4^{(n)} - \mathbf{d}_4^{(n)})). \end{aligned}$$

Here, the above inverse matrix can be efficiently computed as with the CS reconstruction cases.

For the updates of $\mathbf{z}_1, \ldots, \mathbf{z}_4$ (Step 3-6), we need to compute the proximity operators of each term of g. The proximity operator of $\mathcal{R}$ depends on the design of regularization. As addressed in Remark 1, it is indeed computable for many types of regularization. The proximity operator of $\iota_{\mathcal{B}^{\mathbf{v}_n}_{2,\varepsilon_n}}$, $\iota_{\mathcal{B}^{\mathbf{v}_b}_{2,\varepsilon_b}}$, and $\iota_{[0,255]^{3N}}$ equal to the metric projection onto each set given by (2.4) and (2.6).

Algorithm 4: ADMM method for Prob. (4.3)

input : $\mathbf{z}_1^{(0)}$, $\mathbf{z}_2^{(0)}$, $\mathbf{z}_3^{(0)}$, $\mathbf{z}_4^{(0)}$, $\mathbf{d}_1^{(0)}$, $\mathbf{d}_2^{(0)}$, $\mathbf{d}_3^{(0)}$, $\mathbf{d}_4^{(0)}$, and $\gamma > 0$

while *A stopping criterion is not satisfied* **do**

$\mathbf{u}^{(n+1)} = \underset{\mathbf{u}}{\operatorname{argmin}} \frac{1}{2\gamma}(\|\mathbf{z}_1^{(n)} - \mathbf{\Psi}\mathbf{u}^{(n)} - \mathbf{d}_1^{(n)}\|^2 + \|\mathbf{z}_2^{(n)} - \mathbf{u}^{(n)} - \mathbf{d}_2^{(n)}\|^2 + \|\mathbf{z}_3^{(n)} - \mathbf{\Phi}\mathbf{u}^{(n)} - \mathbf{d}_3^{(n)}\|^2 + \|\mathbf{z}_4^{(n)} - \mathbf{u}^{(n)} - \mathbf{d}_4^{(n)}\|^2)$;

$\mathbf{z}_1^{(n+1)} = \operatorname{prox}_{\gamma\mathcal{R}}(\mathbf{\Psi}\mathbf{u}^{(n+1)} + \mathbf{d}_1^{(n)})$;

$\mathbf{z}_2^{(n+1)} = \operatorname{prox}_{\gamma\iota_{[0,255]^{3N}}}(\mathbf{u}^{(n+1)} + \mathbf{d}_2^{(n)})$;

$\mathbf{z}_3^{(n+1)} = \operatorname{prox}_{\gamma\iota_{\mathcal{B}_{\mathbf{v}_n,\varepsilon_n}}}(\mathbf{\Phi}\mathbf{u}^{(n+1)} + \mathbf{d}_3^{(n)})$;

$\mathbf{z}_4^{(n+1)} = \operatorname{prox}_{\gamma\iota_{\mathcal{B}_{\mathbf{v}_b,\varepsilon_b}}}(\mathbf{u}^{(n+1)} + \mathbf{d}_4^{(n)})$;

$\mathbf{d}_1^{(n+1)} = \mathbf{d}_1^{(n)} + \mathbf{\Psi}\mathbf{u}^{(n+1)} - \mathbf{z}_1^{(n+1)}$;

$\mathbf{d}_2^{(n+1)} = \mathbf{d}_2^{(n)} + \mathbf{u}^{(n+1)} - \mathbf{z}_2^{(n+1)}$;

$\mathbf{d}_3^{(n+1)} = \mathbf{d}_3^{(n)} + \mathbf{\Phi}\mathbf{u}^{(n+1)} - \mathbf{z}_3^{(n+1)}$;

$\mathbf{d}_4^{(n+1)} = \mathbf{d}_4^{(n)} + \mathbf{u}^{(n+1)} - \mathbf{z}_4^{(n+1)}$;

$n \leftarrow n + 1$;

Figure 4.1: Test images

4.1.3 Experiments

We demonstrate the three advantages of the proposed method: (i) high quality restoration when the blurred image also contains noise, (ii) robustness to the estimation error of the blur kernel, and (iii) easy parameter setting. In the following experiments, we used 20 color images used as test images, which are taken from the *Berkley Segmentation Database* [102] (Fig. 4.1). Then, we generated a pair of an observations based on (4.1) and (4.2), and estimated a desirable image from them.

We utilized a popular color TV [33] as regularization in our method, which is defined as follows:

$$\mathrm{TV}(\mathbf{u}) := \|\mathbf{D}\mathbf{u}\|_{1,2}.$$

In this case, $\mathcal{R} := \|\cdot\|_{1,2}$ and $\mathbf{\Psi} := \mathbf{D}$ in Prob. (4.3) The proximity operator of the mixed $\ell_{1,2}$ norm can be computed by (2.3). We set ε_n and ε_b in (4.3) to $0.95\sqrt{3N\sigma_n^2}$ and $0.95\sqrt{3N\sigma_b^2}$, respectively.

Experiments results of using both a blurred image and a noisy image are compared with that of using a blurred image only and that of using a noisy image only. At this

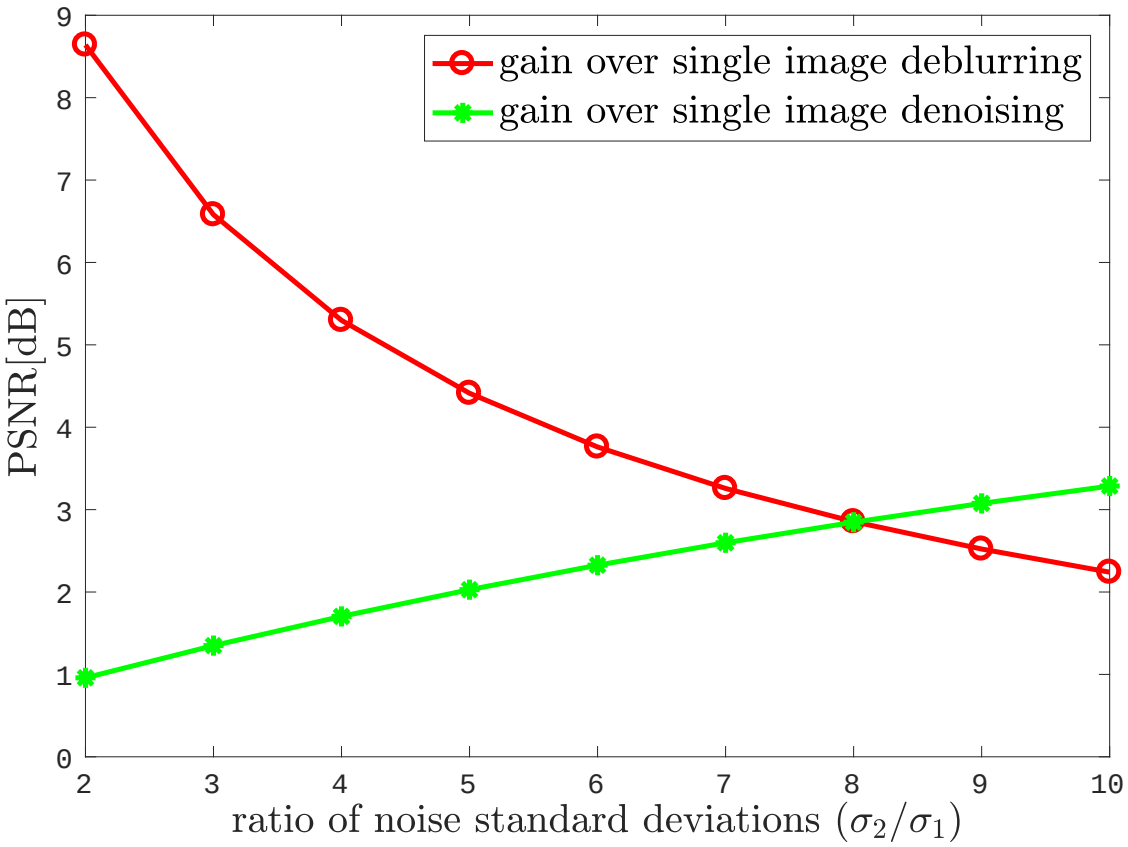

Figure 4.2: PSNR gain of the proposed method over the single image deblurring/denoising.

time, in the case of using a blurred image only, we solved that optimization problem:

$$\min_{\mathbf{u}} \mathrm{TV}(\mathbf{u}) \text{ s.t. } \begin{cases} \mathbf{u} \in [0,255]^{3N}, \\ \mathbf{\Phi u} \in \mathcal{B}_{\mathbf{v}_n,\varepsilon_n} := \{\mathbf{x} \in \mathbb{R}^{3N} | \|\mathbf{x}-\mathbf{v}_n\| \leq \varepsilon_n\}, \end{cases}$$

and in the case of using a blurred image only, we solved that one:

$$\min_{\mathbf{u}} \mathrm{TV}(\mathbf{u}) \text{ s.t. } \begin{cases} \mathbf{u} \in [0,255]^{3N}. \\ \mathbf{u} \in \mathcal{B}_{\mathbf{v}_b,\varepsilon_b} := \{\mathbf{x} \in \mathbb{R}^{3N} | \|\mathbf{x}-\mathbf{v}_b\| \leq \varepsilon_b\}. \end{cases}$$

We adopted PSNR[dB] to evaluate the objective quality of a restored image $\mathbf{u}$, which is given by

$$20 \cdot \log 10 \frac{3N \times 255}{\|\mathbf{u}-\bar{\mathbf{u}}\|}.$$

Basic Performance Evaluation

To evaluate the effectiveness of incorporating multiple hard constraints on data-fidelity to a blurred/noisy image pair, we compare our method with two single image restoration

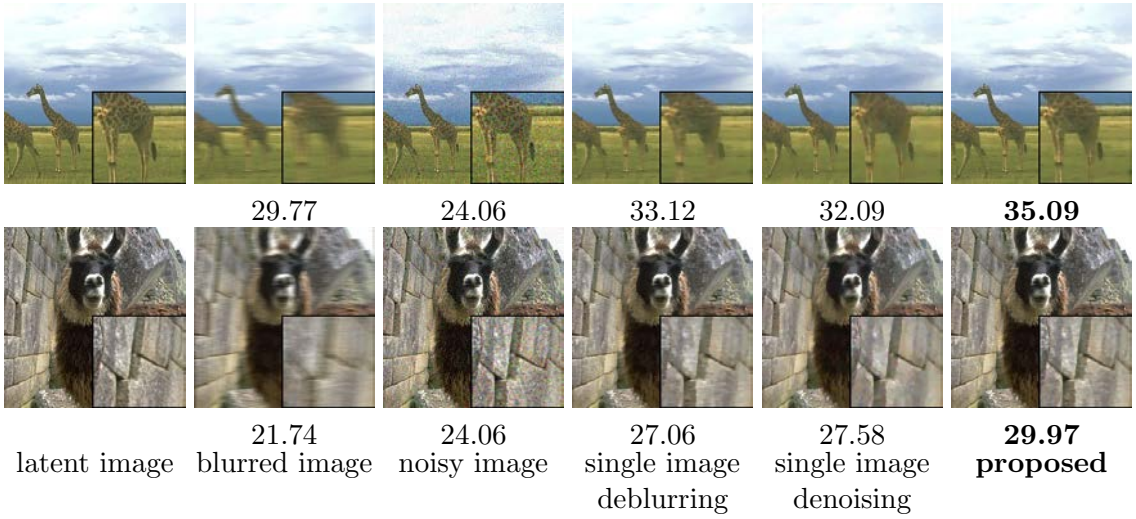

Figure 4.3: Resulting images with their PSNR[dB] in the first experiment ($\sigma_b/\sigma_n = 8$).

methods. One is single image deblurring, i.e., solving Prob. (4.3) without the constraint $\mathbf{u} \in \mathcal{B}_{\mathbf{v}_b,\varepsilon_b}$. The other is single image denoising, i.e., solving Prob. (4.3) without the constraint $\mathbf{\Phi u} \in \mathcal{B}_{\mathbf{v}_n,\varepsilon_n}$. As in our method, ADMM was used for both methods.

In this experiment, we generated blurred images as follows: clean test images are blurred by a horizontal motion blur of 9 pixels and then contaminated by an additive white Gaussian noise $\mathbf{n}_n$ in (4.1) with the standard deviation $\sigma_n = 2$. Meanwhile, noisy images were generated by adding a white Gaussian noise $\mathbf{n}_b$ in (4.2) to clean test images, where the standard deviation σ_b was increased from 4 to 20 by 2.

Fig. 4.2 plots the PSNR gain of our method over the single image deblurring (circle marker) and the single image denoising (asterisk marker), where PSNR is averaged over the 20 test images. One can see that for all the ratio of the noise standard deviations σ_b/σ_n, the proposed method outperforms both single image deblurring and denoising methods. This observation suggests that for a given blurred/noisy image pair, exploiting information on the noisy image in the image restoration step is very effective when the blurred image also contains noise.

Fig. 4.3 depicts some resulting images with their PSNR ($\sigma_b/\sigma_n = 8$). One can see that 1. details are lost in the images obtained by the single image deblurring, 2. color artifact remains in the images obtained by the single image denoising, and 3. Our method achieves detail-preserving restoration with much less artifact.

We also check the convergence behavior of our algorithm (Alg. 4). For evaluation of convergence, we define the normalized root mean square error (NRMSE) between the current estimate $\mathbf{u}^{(n)}$ and the optimal solution $\mathbf{u}^\star$ of Prob. (4.3), i.e., $\mathrm{NRMSE}_n := \|\mathbf{u}^{(n)} - \mathbf{u}^\star\|/\|\mathbf{u}^\star\|$. Since the optimal solution $\mathbf{u}^\star$ is analytically unavailable, it was pre-computed by Alg. 4 with 100000 iterations. Fig. 4.4 plots the evolution of NRMSE_n versus iterations (left) and the evolution of PSNR versus iterations (right), where the stepsize γ of ADMM was set to 0.01. These plots suggest that Alg. 4 properly works, and that exploiting

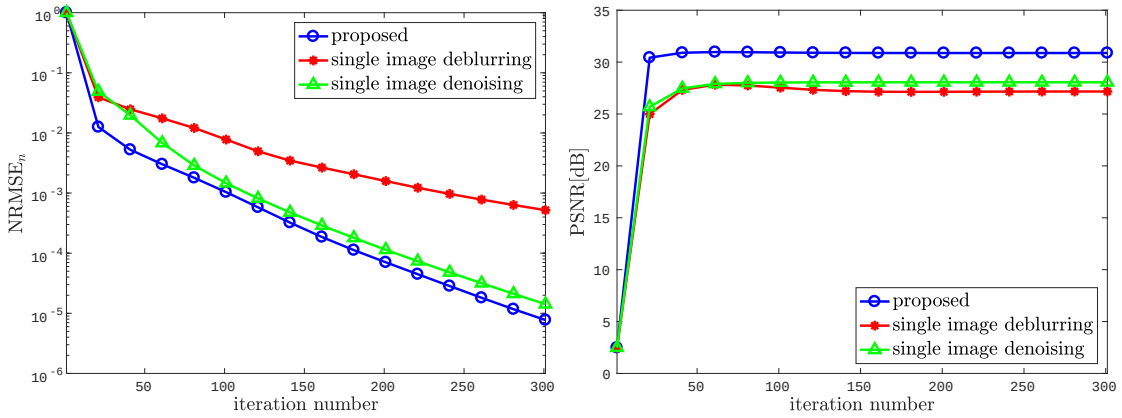

Figure 4.4: Evolution of NRMSE$_n$ versus iterations (left) and the evolution of PSNR[dB] versus iterations (right) of Alg. 4.

Table 4.1: Results of the experiment using inaccurate blur kernel.

kernel error	0°	1°	2°	3°	4°	5°	6°	7°	8°	9°	10°	spatially-varying
PSNR [dB]	32.97	32.91	32.62	32.29	32.01	31.79	31.61	31.47	31.36	31.26	31.17	30.12
gain over single image deblurring	2.85	2.88	3.06	3.40	3.81	4.18	4.47	4.70	4.88	5.03	5.15	6.58

the information on a blurred/noisy image pair makes the convergence of ADMM faster than the single image deblurring/denoising, which is a positive side effect of using a blurred/noisy image pair.

Robustness to Inaccurate Blur Kernels

To illustrate the robustness of our method to the estimation error of blur kernels, we conducted the following experiment. First, we generated images blurred by a certain blur kernel, which we refer to as the true blur kernel, and then in the image restoration step, we used an inaccurate blur kernel. Specifically, we consider the two cases: motion blur and spatially-varying blur. In the motion blur case, the true blur kernel was set to a horizontal motion blur of 9 pixels, and the inaccurate blur kernel was set to a motion blur of 9 pixels with its angle $\theta > 0$, where we examined $\theta = 1^\circ$ to 10° by 1°. In the spatially-varying blur case, the true blur matrix $\mathbf{\Phi}$ was made from spatially-varying per-pixel kernels, as visualized in Fig. 4.6, and the inaccurate blur kernel was set to be spatially invariant with its kernel being the center kernel of the second image from left in Fig. 4.6. For both cases, the blurred images contain an additive white Gaussian noise with the standard deviation $\sigma_n = 2$, and the noisy images $\sigma_b = 16$.

Tab. 4.1 shows PSNR of restored images and the PSNR gain over the single image deblurring, where these valuers are averaged over the 20 test images. One can observe that for the motion blur case, the PSNR gain over the single image deblurring is proportional

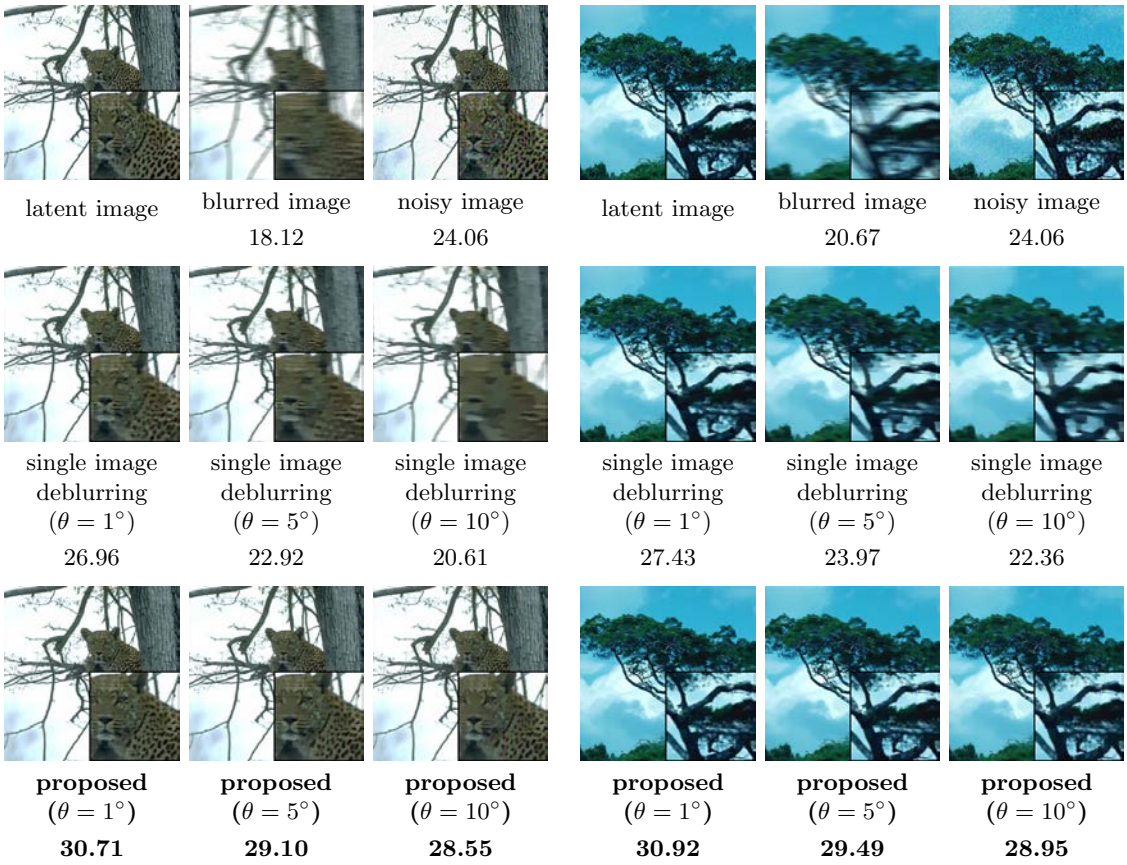

Figure 4.5: Restored results with their PSNR[dB] by using inaccurate blur kernels in the motion blur case.

to the angle error, implying the robustness of our method to inaccurate blur kernels compared with the single image deblurring. For the spartially-varying blur case, the PSNR gain is also significant.

Fig. 4.5 and Fig. 4.6 depict several resulting images with their PSNR. One can see that the single image deblurring leads to oversmoothing when the kernel error is large. By contrast, our method can restore sharp images in such a situation.

Facilitation of Parameter Setting

In the final experiment, we demonstrate that the setting of the parameters on data-fidelity in our method are much easier than the existing methods using a blurred/noisy image pair in the restoration step [80, 81]. In the existing methods, image restoration is performed by minimizing the sum of some specific regularization term and two data-fidelity terms on a blurred/noisy image pair, which can be expressed as the following

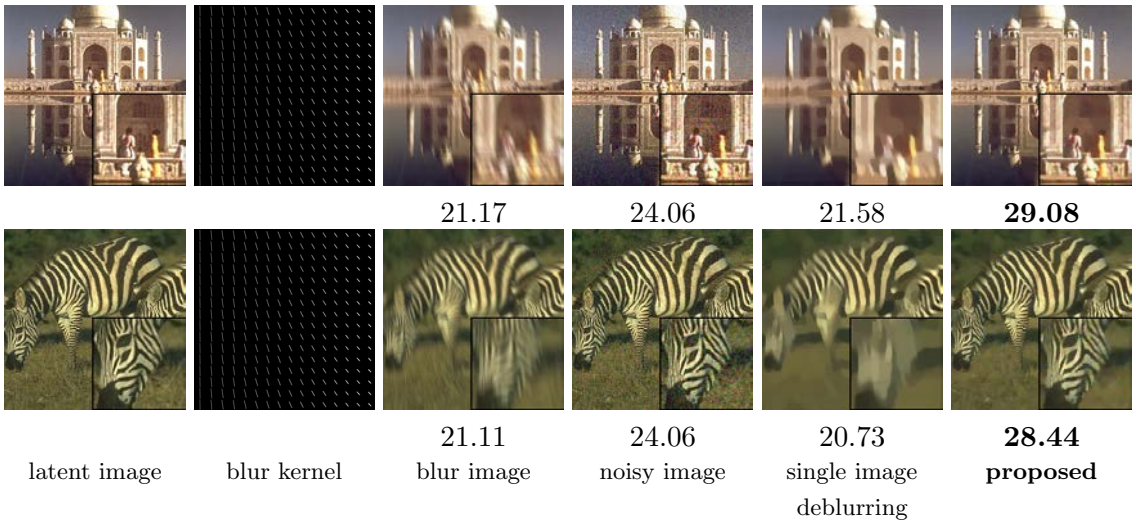

Figure 4.6: Restored results with their PSNR[dB] by using an inaccurate blur kernel in the spatially-varying blur case.

Table 4.2: Best values of λ_1 and λ_2 in the existing formulation (Prob. (4.7)).

image	img1	img2	img3	img4	img5	img6	img7	img8	img9	img10
λ_1	733	1047	578	603	563	801	916	446	589	645
λ_2	8	9	11	7	9	8	7	9	6	7
image	img11	img12	img13	img14	img15	img16	img17	img18	img19	img20
λ_1	770	895	988	932	905	812	917	678	920	650
λ_2	6	8	8	8	7	6	8	8	8	8

optimization problem:

$$\min_{\mathbf{u}} \mathcal{R}(\mathbf{\Psi u}) + \frac{\lambda_1}{2}\|\mathbf{\Phi u} - \mathbf{v}_n\|^2 + \frac{\lambda_2}{2}\|\mathbf{u} - \mathbf{v}_b\|^2, \tag{4.7}$$

where $\lambda_1, \lambda_2 > 0$ control the balance among the three terms.

Tab. 4.2 shows the (hand-optimized) best values of λ_1 and λ_2 (in terms of PSNR) in Prob. (4.7) for each test image, where the regularization term was set to the color TV. For every test image, the noise standard deviations of a blurred/noisy image pair (σ_n, σ_b) were fixed at $(2, 16)$. One can see that the best values of λ_1 and λ_2 are different for each test image even though the noise standard deviations are the same for every test image. This is because λ_1 and λ_2 depend on the latent image, so that the tuning of them is very difficult. By contrast, the proposed method achieves almost the same restoration performance with common parameters $\varepsilon_n = 0.95\sqrt{3N\sigma_n^2}$ and $\varepsilon_b = 0.95\sqrt{3N\sigma_b^2}$ for all the test images, i.e., the parameter setting is much easier.

4.2 Hyperspectral Image Fusion for Super-resolution

An HS image has rich spectral information, and HS imaging is a promising research topic and offers many applications in a wide range of fields [19, 20]. These applications require an HS image of high spatial and spectral resolution (HR-HS image). However, since the amount of incident energy is limited, and there are critical tradeoffs between the spatial resolution and the spectral resolution of HS imaging systems, it is a very difficult task to capture an HR-HS image.

HS image fusion techniques [103–105] try to resolve this dilemma, and have been actively studied [106–121]. They estimate an HR-HS image using a pair of an observed HS image of high spectral resolution but low spatial resolution (LR-HS image) and an observed guide image of high spatial resolution but low spectral resolution. In general, the guide image is assumed a panchromatic (PAN) image or an MS image, where a PAN image has only 2D spatial information, i.e., a grayscale image.

Most recent HS image fusion methods [113–121] utilize apriori knowledge on an HS image and observed information on an LR-HS image and a guide image, and estimate HR-HS images by solving optimization problems. Thanks to the setting, they achieve high-quality fusion. However, since these methods do not consider that a guide image may also contain noise, they cannot achieve high-quality estimation, when the guide image is noisy. As a result, the resulting HS images often have artifacts and spectral distortion.

To resolve the above problems, we propose a new robust HS image fusion method, which considers noisy guide images. The proposed method estimates not only an HR-HS image but also a clean guide image, leading to high quality and robust estimation. The method is built upon a convex optimization problem, where its objective function consists of regularization terms for HS and guide images, respectively, and an edge similarity term between HS and guide images. Data-fidelity to an LR-HS and a guide image and their dynamic ranges are evaluated by hard constraints. This problem fully utilizes observed information and apriori knowledge of an HS and a guide image, so that it can estimate an HR-HS image without artifacts and spectral distortion even if both observed images are contaminated by severe noise. To solve the optimization problem, we adopt a primal-dual splitting method.

4.2.1 Problem Formulation

In hyperspectral image fusion, an LR-HS image $\mathbf{v}_H \in \mathbb{R}^{\frac{NB}{r}}$ and an observed guide image $\mathbf{v}_g \in \mathbb{R}^M$ are assumed to be given with the observation model:

$$\mathbf{v}_H = \mathbf{S}\mathbf{B}\bar{\mathbf{u}} + \mathbf{n}_H, \tag{4.8}$$

$$\mathbf{v}_g = \mathbf{R}\bar{\mathbf{u}} + \mathbf{n}_g, \tag{4.9}$$

where $\mathbf{S} \in \mathbb{R}^{\frac{NB}{r} \times NB}$ is a downsampling matrix with a downsampling rate of r (r is divisor of N), $\mathbf{B}$ is a blur matrix, $\mathbf{n}_H$ and $\mathbf{n}_g$ are additive white Gaussian noises with standard deviations σ_H and σ_g, respectively, and $\mathbf{R} \in \mathbb{R}^{M \times NB}$ is a matrix representing the spectral response of the observed PAN image ($\mathbf{R}$ calculates weighted average along the spectral direction). In general, since HS images contain more noise than guide images, we assume

$\sigma_H > \sigma_g$. This model says that both the LR-HS image and the observed guide image contain considerable noise, which is a natural situation in hyperspectral imaging.

Based on the model, we formulate a hyperspectral image fusion problem as a convex optimization problem. This problem estimates not only an HR-HS image $\mathbf{u}_H \in \mathbb{R}^{NB}$ but also a clean guide image $\mathbf{u}_g \in \mathbb{R}^M$, leading to high quality and robust estimation.

$$\begin{aligned} &\min_{\mathbf{u}_H, \mathbf{u}_g} \mathrm{HSSTV}(\mathbf{u}_H) + \lambda \|\mathbf{D}\mathbf{u}_H - \mathbf{D}\mathbf{M}\mathbf{u}_g\|_{1,2} + \|\mathbf{D}\mathbf{u}_g\|_{1,2} \\ &\text{s.t.} \quad \left[\begin{array}{l} \mathbf{S}\mathbf{B}\mathbf{u}_H \in \mathcal{B}_{2,\varepsilon}^{\mathbf{v}_H} := \{\mathbf{x} \in \mathbb{R}^{\frac{NB}{r}} \,|\, \|\mathbf{x} - \mathbf{v}_H\| \leq \varepsilon\}, \\ \mathbf{u}_g \in \mathcal{B}_{2,\eta}^{\mathbf{v}_g} := \{\mathbf{x} \in \mathbb{R}^N \,|\, \|\mathbf{x} - \mathbf{v}_g\| \leq \eta\}, \\ \mathbf{u}_H \in [\underline{\mu_{\mathbf{u}_H}}, \overline{\mu_{\mathbf{u}_H}}]^{NB}, \\ \mathbf{u}_g \in [\underline{\mu_{\mathbf{u}_g}}, \overline{\mu_{\mathbf{u}_g}}]^M, \end{array} \right. \end{aligned} \tag{4.10}$$

where the parameter $\lambda > 0$ is the parameter adjusting evaluation degree of the second term, and $\mathbf{M} \in \mathbb{R}^{NB \times M}$ is a linear operator that replicates the estimated guide image along the spectral direction so that the number of bands in the guide image is the same as that in the HS image.

The first and third terms in Prob. (4.10) are regularization functions for HS image and guide imege restoration, respectively. HSSTV has been shown to be very effective in HS image restoration, and we describe HSSTV in Sec. 3.1.2. By using HSSTV, the proposed hyperspectral image fusion method can do robust estimation when the LR-HS image and the observed guide image contain noise. The regularization for guide image restoration is vectorial TV.

The second term in Prob. (4.10) evaluates edge similarity between the HR-HS image $\mathbf{u}_H$ and the estimated guide image $\mathbf{u}_g$, which is originally proposed in [122]. Specifically, we can assume that the non-zero differences of the HR-HS image are sparse and correspond to edges, and that their positions should be the same as those of the estimated guide image. Hence, evaluating their errors by the mixed $\ell_{1,2}$ norm is a reasonable approach for exploiting the spatial information on the estimated guide image.

The first constraint in (4.10) serves as data-fidelity to the LR-HS image $\mathbf{v}_H$ and is defined as the $\mathbf{v}_H$-centered ℓ_2-norm ball with the radius $\varepsilon > 0$. Likewise, the second constraint in (4.10) plays data-fidelity role to the observed PAN image $\mathbf{v}_g$ and is defined as the $\mathbf{v}_g$-centered ℓ_2-norm ball with the radius $\eta > 0$. The third and fourth constraint in (4.10) represent the dynamic range of a HS image and a guide image, respectively.

4.2.2 Optimization

Since Prob. (4.10) is a convex but highly constrained nonsmooth optimization problem, we require a suitable iterative algorithm, e.g., an alternating direction method of multipliers, to solve it. In this paper, we adopt a primal-dual splitting method [17] and we explain it in Sec. 2.3. To solve Prob. (4.10) by the primal-dual splitting method, we reformulate Prob. (4.10) into Prob. (2.9).

We put the four constraints in Prob. (4.10) into the objective function. By the indicator

Algorithm 5: A primal-dual splitting method for Prob. (4.10).

input : $\mathbf{u}^{(0)}$, $\mathbf{u}_g^{(0)}$, $\mathbf{y}_1^{(0)}$, $\mathbf{y}_2^{(0)}$, $\mathbf{y}_3^{(0)}$, $\mathbf{y}_4^{(0)}$, $\mathbf{y}_5^{(0)}$

while *A stopping criterion is not satisfied do* **do**

$\mathbf{u}^{(n+1)} = \mathrm{prox}_{\gamma_1 \iota_{[\underline{\mu_{\mathbf{u}_H}}, \overline{\mu_{\mathbf{u}_H}}]^{NB}}} (\mathbf{u}^{(n)} - \gamma_1(\mathbf{A}_\omega^\top \mathbf{y}_1^{(n)} + \mathbf{D}^\top \mathbf{y}_2^{(n)} + \mathbf{B}^\top \mathbf{S}^\top \mathbf{y}_4^{(n)}))$;

$\mathbf{u}_g^{(n+1)} = \mathrm{prox}_{\gamma_1 \iota_{[\underline{\mu_{\mathbf{u}_g}}, \overline{\mu_{\mathbf{u}_g}}]^{N}}} (\mathbf{u}_g^{(n)} - \gamma_1(-\mathbf{M}^\top \mathbf{D}^\top \mathbf{y}_2^{(n)} + \mathbf{D}^\top \mathbf{y}_3^{(n)} + \mathbf{y}_5^{(n)}))$;

$\mathbf{y}_1^{(n)} \leftarrow \mathbf{y}_1^{(n)} + \gamma_2 \mathbf{A}_\omega (2\mathbf{u}^{(n+1)} - \mathbf{u}^{(n)})$;

$\mathbf{y}_2^{(n)} \leftarrow \mathbf{y}_2^{(n)} + \gamma_2 (\mathbf{D}(2\mathbf{u}^{(n+1)} - \mathbf{u}^{(n)}) - \mathbf{DM}(2\mathbf{u}_g^{(n+1)} - \mathbf{u}_g^{(n)}))$;

$\mathbf{y}_3^{(n)} \leftarrow \mathbf{y}_3^{(n)} + \gamma_2 \mathbf{D}(2\mathbf{u}_g^{(n+1)} - \mathbf{u}_g^{(n)})$;

$\mathbf{y}_4^{(n)} \leftarrow \mathbf{y}_4^{(n)} + \gamma_2 \mathbf{SB}(2\mathbf{u}^{(n+1)} - \mathbf{u}^{(n)})$;

$\mathbf{y}_5^{(n)} \leftarrow \mathbf{y}_5^{(n)} + \gamma_2 (2\mathbf{u}_g^{(n+1)} - \mathbf{u}_g^{(n)})$;

$\mathbf{y}_1^{(n+1)} = \mathbf{y}_1^{(n)} - \gamma_2 \, \mathrm{prox}_{\frac{1}{\gamma_2}, \|\cdot\|_{1,p}} \left(\frac{\mathbf{y}_1^{(n)}}{\gamma_2} \right)$;

$\mathbf{y}_2^{(n+1)} = \mathbf{y}_2^{(n)} - \gamma_2 \, \mathrm{prox}_{\frac{\lambda}{\gamma_2}, \|\cdot\|_{1,2}} \left(\frac{\mathbf{y}_2^{(n)}}{\gamma_2} \right)$;

$\mathbf{y}_3^{(n+1)} = \mathbf{y}_3^{(n)} - \gamma_2 \, \mathrm{prox}_{\frac{1}{\gamma_2}, \|\cdot\|_{1,2}} \left(\frac{\mathbf{y}_3^{(n)}}{\gamma_2} \right)$;

$\mathbf{y}_4^{(n+1)} = \mathbf{y}_4^{(n)} - \gamma_2 \, \mathrm{prox}_{\frac{1}{\gamma_2}, \mathcal{B}_{2,\varepsilon}^{\mathbf{v}}} \left(\frac{\mathbf{y}_4^{(n)}}{\gamma_2} \right)$;

$\mathbf{y}_5^{(n+1)} = \mathbf{y}_5^{(n)} - \gamma_2 \, \mathrm{prox}_{\frac{1}{\gamma_2}, \mathcal{B}_{2,\eta}^{\mathbf{v}_g}} \left(\frac{\mathbf{y}_5^{(n)}}{\gamma_2} \right)$;

$n \leftarrow n + 1$;

functions, Prob. (4.10) can be rewritten as

$$\min_{\mathbf{u}_H, \mathbf{u}_g} \|\mathbf{A}_\omega \mathbf{u}_H\|_{1,p} + \lambda \|\mathbf{D}\mathbf{u}_H - \mathbf{DM}\mathbf{u}_g\|_{1,2} + \|\mathbf{D}\mathbf{u}_g\|_{1,2} + \iota_{\mathcal{B}_{2,\varepsilon}^{\mathbf{v}_H}}(\mathbf{SB}\mathbf{u}_H) + \iota_{\mathcal{B}_{2,\eta}^{\mathbf{v}_g}}(\mathbf{u}_g) + \iota_{[\underline{\mu_{\mathbf{u}_H}}, \overline{\mu_{\mathbf{u}_H}}]^{NB}}(\mathbf{u}_H) + \iota_{[\underline{\mu_{\mathbf{u}_g}}, \overline{\mu_{\mathbf{u}_g}}]^{M}}(\mathbf{u}_g). \tag{4.11}$$

Prob. (4.10) and Prob. (4.11) are equivalent from the definition of the indicator function. Then, by letting

$$g : \mathbb{R}^{NB+M} \to \mathbb{R}^2 : (\mathbf{u}_H, \mathbf{u}_g) \mapsto (\iota_{[\underline{\mu_{\mathbf{u}_H}}, \overline{\mu_{\mathbf{u}_H}}]^{NB}}(\mathbf{u}_H), \iota_{[\underline{\mu_{\mathbf{u}_g}}, \overline{\mu_{\mathbf{u}_g}}]^{M}}(\mathbf{u}_g))$$

$$h : \mathbb{R}^{\left(\left(5+\frac{1}{r}\right)B+3\right)N+M} \to \mathbb{R} \cup \{\infty\} : (\mathbf{y}_1, \mathbf{y}_2, \mathbf{y}_3, \mathbf{y}_4, \mathbf{y}_5) \mapsto \|\mathbf{y}_1\|_{1,p} + \lambda \|\mathbf{y}_2\|_{1,2} + \|\mathbf{y}_3\|_{1,2} + \iota_{\mathcal{B}_{2,\varepsilon}^{\mathbf{v}_H}}(\mathbf{y}_4) + \iota_{\mathcal{B}_{2,\eta}^{\mathbf{v}_g}}(\mathbf{y}_5),$$

$$\mathbf{L} : \mathbb{R}^{N(B+1)} \to \mathbb{R}^{\left(\left(5+\frac{1}{r}\right)B+3\right)N+M} : (\mathbf{u}_H, \mathbf{u}_g) \mapsto (\mathbf{A}_\omega \mathbf{u}_H, \mathbf{D}\mathbf{u}_H - \mathbf{DM}\mathbf{u}_g, \mathbf{D}\mathbf{u}_g, \mathbf{SB}\mathbf{u}_H, \mathbf{u}_g),$$

Prob. (4.11) is reduced to Prob. (2.9). Using (2.11), the resulting algorithm for solving (4.10) is summarized in Alg. 5. Some steps in Alg. 5 require the proximity operators, and we explain them in Sec 2.1.

4.2.3 Hyperspectral Pansharpening Experiments

In this section, we demonstrate the advantages of the proposed method over existing HS pansharpening methods. For HS pansharpening, a guide image $\mathbf{v}_g$ is a PAN image,

Table 4.3: Quality measures for $\sigma_g = 0.025$ (top), $\sigma_g = 0.05$ (middle), and $\sigma = 0.075$ (bottom).

σ_g	method	CC	SAM	RMSE	ERGAS
0.025	SFIM [112]	0.4528	38.87	1571	23.86
	MTF-GLP [110]	0.6920	34.68	974.4	16.05
	MTF-GLP-HPM [111]	0.4605	38.89	1576	23.80
	GS [108]	0.5946	39.77	1101	20.54
	GSA [109]	0.6841	41.71	1083	20.11
	PCA [123]	0.5913	39.93	1111	20.72
	GFPCA [107]	0.9019	11.18	462.1	8.045
	CNMF [116]	0.8863	15.10	512.1	8.338
	Bayesian Naive [113]	0.8498	27.20	602.2	11.07
	Bayesian Sparse [114]	0.8526	26.68	594.1	10.95
	HySure [115]	0.9273	15.93	402.9	7.017
	proposed ($p = 1$)	0.9515	9.777	322.4	5.672
	proposed ($p = 2$)	**0.9516**	**9.763**	**322.2**	**5.666**
0.05	SFIM	0.4170	39.45	1691	25.32
	MTF-GLP	0.6284	35.47	1112	17.76
	MTF-GLP-HPM	0.4286	39.54	1680	25.11
	GS	0.5108	41.04	1213	22.39
	GSA	0.6201	44.77	1303	23.81
	PCA	0.5086	41.21	1221	22.53
	GFPCA	0.8813	11.54	500.6	8.762
	CNMF	0.7839	16.23	729.0	11.90
	Bayesian Naive	0.7782	30.88	800.9	14.26
	Bayesian Sparse	0.7830	30.34	785.4	14.03
	HySure	0.8704	20.46	557.1	9.714
	proposed ($p = 1$)	0.9409	9.891	344.4	6.135
	proposed ($p = 2$)	**0.9410**	**9.878**	**344.2**	**6.130**
0.075	SFIM	0.4259	39.59	1680	25.63
	MTF-GLP	0.5826	36.03	1210	18.92
	MTF-GLP-HPM	0.4429	39.57	1643	25.25
	GS	0.4310	42.00	1311	24.02
	GSA	0.5459	48.48	1601	28.89
	PCA	0.4297	42.17	1317	24.13
	GFPCA	0.8694	11.71	520.2	9.138
	CNMF	0.6811	17.69	951.5	15.48
	Bayesian Naive	0.6920	35.00	1052	18.38
	Bayesian Sparse	0.7003	34.35	1023	17.93
	HySure	0.7868	25.34	774	13.52
	proposed ($p = 1$)	0.9350	9.919	356.7	6.387
	proposed ($p = 2$)	**0.9351**	**9.907**	**356.5**	**6.382**

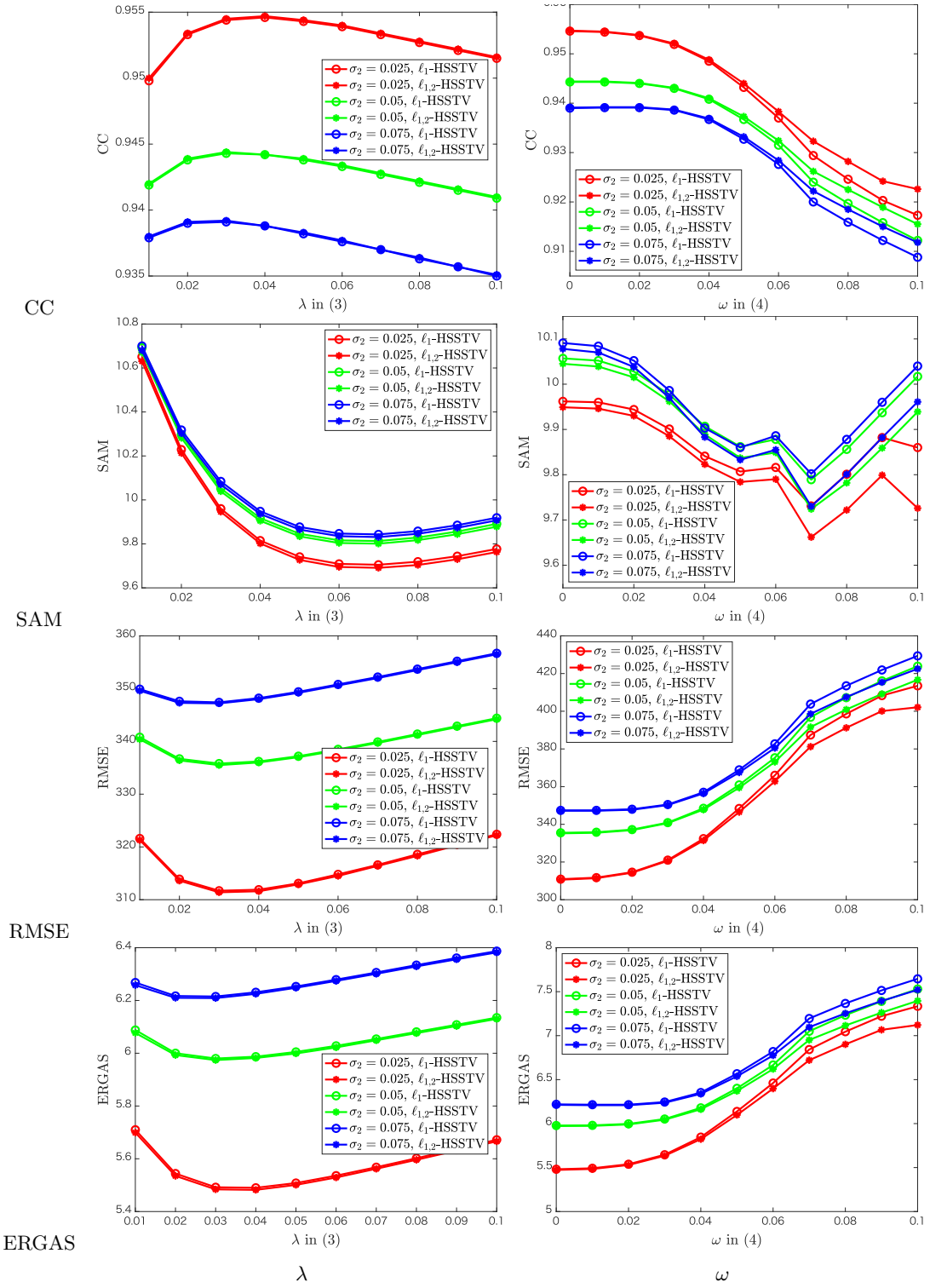

Figure 4.7: Quality measures versus λ in (4.10) (top) / ω in (3.6) (bottom).

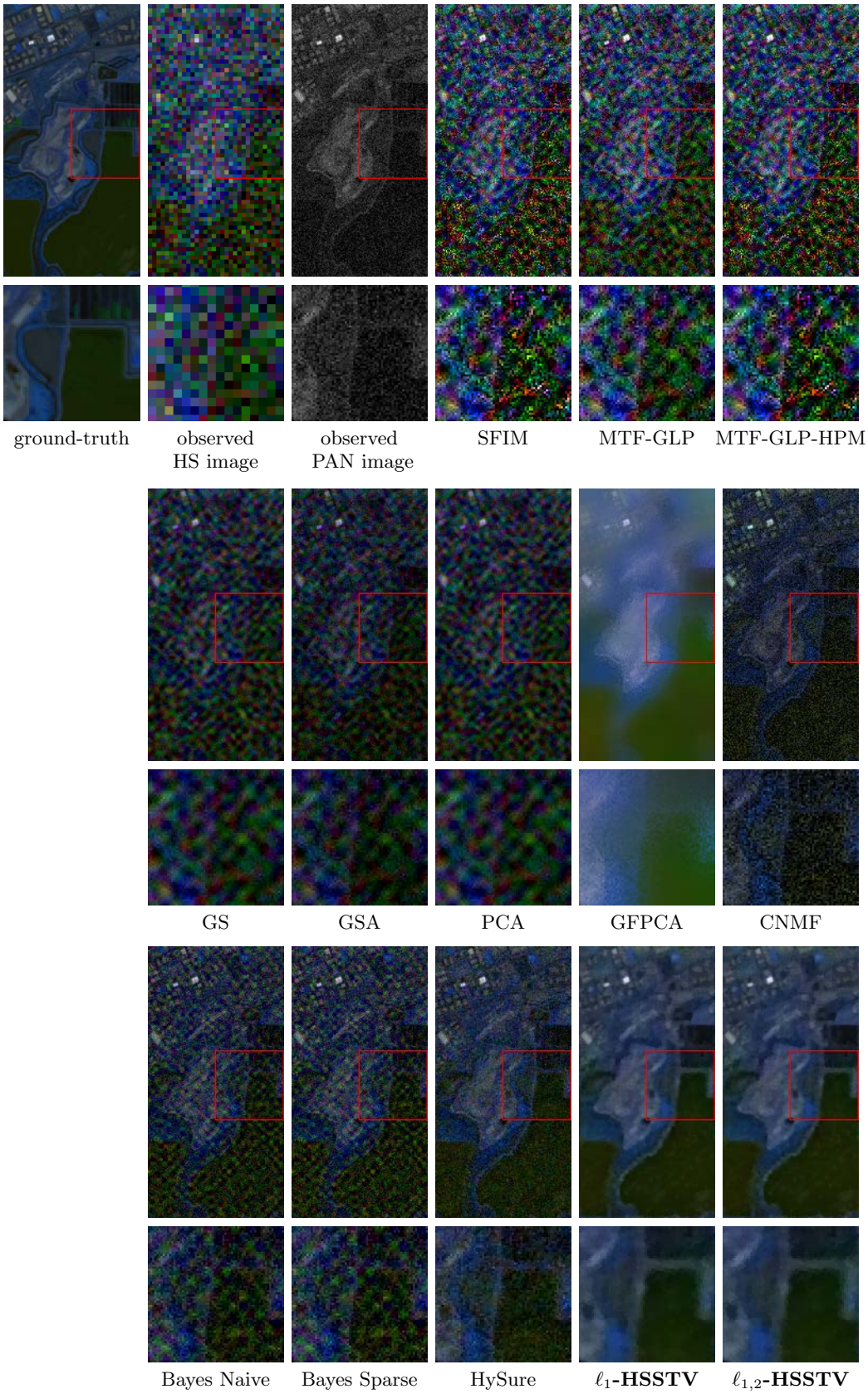

Figure 4.8: Resulting HS images on the HS pansharpening experiments ($\sigma_H = 0.1$, $\sigma_g = 0.05$).

i.e., the number of pixel $M = N$. In this experiments, we generated a pair of an LR-HS and an observed PAN image based on (4.8) and (4.9), estimated the HR-HS image from the pair. We used a Moffett field dataset as the true HR-HS image, which it is clipped in a region of size $256 \times 128 \times 176$ and normalized its dynamic range into $[0, 1]$, i.e., $\underline{\mu_{\mathbf{u}_H}} = \underline{\mu_{\mathbf{u}_g}} = 0$ and $\overline{\mu_{\mathbf{u}_H}} = \overline{\mu_{\mathbf{u}_g}} = 1$ in Prob. (4.10). In (4.8) and (4.9), the downsampling rate of $\overline{\mathbf{S}}$ was set as $r = 4$, $\mathbf{B}$ was set to a 9×9 Gaussian blur matrix, and $\mathbf{R}$ was set to an weighted-average matrix with its weights w_i $(i = 1, \ldots, B)$ were defined by

$$w_i = \begin{cases} 1, & \text{if } 1 \leq i \leq 41 \\ 0, & \text{otherwise.} \end{cases}$$

Then, we experimented with three pair of the standard deviations, $(\sigma_H, \sigma_g) = (0.1, 0.025)$, $(0.1, 0.05)$, $(0.1, 0.075)$. The above procedures follow Wald's protocol [124], so that one can see that it is a standard quality assessment methodology of HS pansharpening.

As compared methods, we utilize 11 existing methods: SFIM [112], MTF-GLP [110], MTF-GLP-HPM [111], GS [108], GSA [109], PCA [123], GFPCA [107], CNMF [116], Bayesian Naive [113], Bayesian Sparse [114] and HySure [115]. To set all parameters of these methods other than HySure, we used setting in a MATLAB toolbox of HS pansharpening[1]. For HySure, we set its hyperparameter as $\lambda_{\mathbf{v}_g hi} = 0.1\sigma_H$ to enhance its performance, and other parameters were set in the same way with other methods. For our method, the parameters ε and η in (4.10) were set to oracle value, i.e., $\varepsilon = \|\mathbf{v} - \mathbf{SB}\bar{\mathbf{u}}\|$, $\eta = \|\mathbf{v}_g - \mathbf{R}\bar{\mathbf{u}}\|$. Moreover, we varied $\lambda \in [0.01, 0.1]$ and $\omega \in [0, 0.1]$ to inspect suitable them. We set the stepsizes, the max iteration number and the stopping criterion of the primal-dual splitting method to $\gamma_1 = 0.005$, $\gamma_2 = 1/1100\gamma_1$, 5000 and $\|\mathbf{u}^{(n)} - \mathbf{u}^{(n+1)}\|/\|\mathbf{u}^{(n)}\| < 1.0 \times 10^{-4}$, respectively.

For the evaluation of the estimation performance, we adopt cross correlation (CC), the spectral angle mapper (SAM) [14], the root mean squared error (RMSE), and erreur relative globale adimensionnelle de synthèse (ERGAS) [15] as quality measures, which are defined as follows: for $i = 1, \ldots, N$ and $j = 1, \ldots, B$,

$$\begin{aligned}
\mathrm{CC}(\mathbf{u}, \bar{\mathbf{u}}) &= \frac{1}{B} \sum_{j=1}^{B} \frac{\sum_{i=1}^{N} (u_{i+(j-1)N} - \alpha_{\mathbf{u},j})(\bar{u}_{i+(j-1)N} - \alpha_{\bar{\mathbf{u}},j})}{\sqrt{\sum_{i=1}^{N} (u_{i+(j-1)N} - \alpha_{\mathbf{u},j})^2 \sum_{i=1}^{N} (\bar{u}_{i+(j-1)N} - \alpha_{\bar{\mathbf{u}},j})^2}}, \\
\mathrm{SAM}(\mathbf{u}, \bar{\mathbf{u}}) &= \frac{1}{N} \sum_{i=1}^{N} \arccos\left(\frac{\mathbf{u}_i^\top \bar{\mathbf{u}}_i}{\|\mathbf{u}_i\| \|\bar{\mathbf{u}}_i\|} \right), \\
\mathrm{RMSE}(\mathbf{u}, \bar{\mathbf{u}}) &= \frac{\|\mathbf{u} - \bar{\mathbf{u}}\|}{\sqrt{NB}}, \\
\mathrm{ERGAS}(\mathbf{u}, \bar{\mathbf{u}}) &= \frac{100}{r} \sqrt{\frac{1}{B} \sum_{j=1}^{B} \frac{\|\mathbf{u}_j^* - \bar{\mathbf{u}}_j^*\|^2}{\left(\frac{1}{p} \mathbf{1}^\top \mathbf{u}_j^*\right)^{2'}}},
\end{aligned}$$

respectively, where $\mathbf{u}_i = [u_i, u_{i+N}, \ldots, u_{i+(B-1)N}] \in \mathbb{R}^B$ is the i-th spectral vector of $\mathbf{u}$, $\mathbf{u}_j^* = [u_{N(j-1)+1}, u_{N(j-1)+2}, \ldots, u_{N(j-1)+N}] \in \mathbb{R}^N$ is the j-th spatial one, $\alpha_{\mathbf{u},j} =$

[1] http://openremotesensing.net/

Table 4.4: Quality measures for $\sigma_g = 0.04$ (left) and $\sigma_g = 0.06$ (right) averaged all HS images.

	$\sigma_m = 0.04$				$\sigma_m = 0.08$			
	PSNR	SAM	ERGAS	$Q2^n$	PSNR	SAM	ERGAS	$Q2^n$
MTF-GLP [110]	22.80	10.45	7.557	0.4937	22.28	11.09	7.905	0.4649
CNMF [116]	26.40	9.139	6.104	0.6264	24.25	10.68	7.211	0.5273
HySure [115]	28.65	8.354	7.511	0.6836	27.93	7.676	7.448	0.6550
MAPSMM [120]	24.06	10.39	14.00	0.4973	23.49	11.12	14.53	0.4658
proposed (HTV, $p = 1$)	29.79	5.103	4.459	0.7110	28.64	5.277	4.931	0.6790
proposed (HTV, $p = 2$)	29.89	**5.020**	**4.386**	0.7163	**28.70**	**5.209**	**4.866**	0.6832
proposed (HSSTV, $p = 1$)	29.86	5.774	5.062	0.7179	28.56	6.062	5.569	0.6829
proposed (HSSTV, $p = 2$)	**29.95**	5.711	5.006	**0.7231**	28.64	6.002	5.513	**0.6880**

$\sum_{i=1}^{N} u_{i+(j-1)N}$, $\alpha_{\bar{\mathbf{u}},j} = \sum_{i=1}^{N} \bar{u}_{i+(j-1)N}$ and $\mathbf{1} = [1, \ldots, 1] \in \mathbb{R}^N$. Moreover, the closer CC is 1 and the smaller SAM, RMSE and ERGAS are, the more alike the estimated HR-HS image $\mathbf{u}$ and the true HR-HS image $\bar{\mathbf{u}}$.

Tab. 4.3 shows CC, SAM, RMSE and ERGAS of the HR-HS images estimated by the existing and proposed methods ($p = 1$ or 2 in (3.6)) for $\sigma_g = 0.025$, 0.05 and 0.075. For all the quality measures and all standard deviations, one can see that the proposed method outperforms all the existing methods.

Fig. 4.7 plots CC, SAM, RMSE and ERGAS of the HR-HS images estimated by the proposed method versus λ in (4.10) and ω in (3.6), respectively, where we set $\omega = 0.01$ in the λ graphs and $\lambda = 0.03$ in the ω graphs. In CC, RMSE and ERGAS case, we found that $\lambda \in [0.02, 0.05]$ and $\omega \in [0, 0.02]$ are good choices, and HSSTV almost need not to evaluate the direct spatial piecewise smoothness of an HS image in this experimental setting. This is because the second term in Prob. (4.10) can evaluate it not just edge similarity. For SAM case, $\lambda \in [0.06, 0.08]$ and $\omega \in [0.05, 0.08]$ are good choices.

Fig. 4.8 is the estimated HR-HS images in the $(\sigma_H, \sigma_g) = (0.1, 0.05)$ case, which depicts as RGB images (R = 16th, G = 32nd and B = 64th bands). One can see that the results estimated by most of the existing methods remain noise in the observed PAN image and include artifacts. In addition, since the color in the results by GFPCA, CNMF and HySure is different from that in the original HS image, it shows that these methods produce spectral distortion. In contrast, the proposed method can estimate the HR-HS image without noise, artifacts and spectral distortion, and it is most similar to the true HR-HS image.

4.2.4 Hyperspectral and Multispectral Image Fusion Experiments

We demonstrate the advantages of the proposed method over existing HS and MS fusion methods. In the experience, first, we generated both LR-HS and MS images using a test

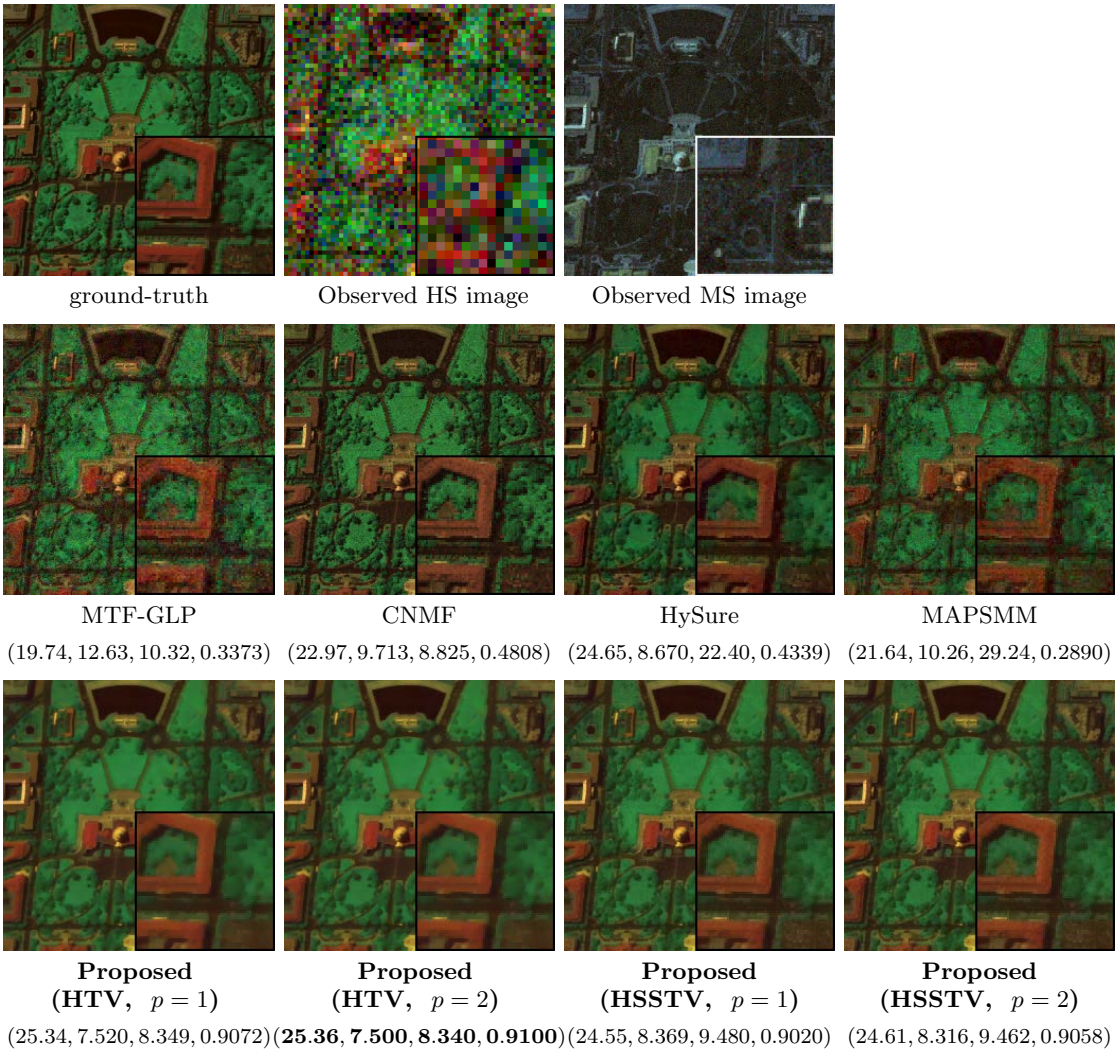

Figure 4.9: Resulting HS images with four quality measure (PSNR[dB], SAM, ERGAS, $Q2^n$) (DC, $\sigma_g = 0.04$).

HR-HS image based on (4.8) and (4.9), where $\mathbf{n}_H$ and $\mathbf{n}_g$ are additive white Gaussian noises with standard deviation σ_H and σ_g, respectively. At this time, we adopted 15 HS images from the *SpecTIR* [44], *MultiSpec* [45], *GIC* [46], *a Moffett field dataset* and *Chikusei* [125] as the test HS image, which are normalized its dynamic range into $[0, 1]$. In addition, the downsampling rate of $\mathbf{S}$ was set as $r = 4$, the kernel of $\mathbf{B}$ was a 9×9 Gaussian blur matrix, and $\mathbf{R}$ was a partial average matrix, which divides bands of an HS image into eight parts, and averages it in each group.

Second, we estimated an HR-HS image from the pair by each method. In this experiments, we utilized MTF-GLP [110], CNMF [116], HySure [115] and MAPSMM [120] as compared methods. Here, with respect to MTF-GLP and MAPSMM, all parameters were set to the recommended values in a MATLAB toolbox of HS and MS fusion [105]. In the case of HySure, we decided that its parameter regarding data fidelity $\lambda_\phi = 0.5(\sigma_h + \sigma_m)$, and for CNMF, the parameter was set to $\theta_h = \sigma_h$ and $\theta_m = \sigma_m$ for fair comparison. The other parameters in HySure and CNMF were set to the values of the same toolbox. For the proposed method, we decided that the parameters $\varepsilon = \|\mathbf{v}_H - \mathbf{S}\mathbf{B}\bar{\mathbf{u}}_H\|$, $\eta = \|\mathbf{v}_g - \mathbf{R}\bar{\mathbf{u}}_g\|$, $\omega = 0.02$, and $\lambda = 0.3$. Besides, for verification of the availability of HSSTV regarding an MS image denoising, we experimented by the method replacing the third term in Prob. (4.10) with HSSTV, i.e., $\|\mathbf{D}\mathbf{u}_g\|_{1,2}$ is replaced HSSTV($\mathbf{u}_g$) with $\omega = 0.1$.

Finally, we evaluated the estimated high HS images based on four standard quality measures: PSNR[dB], SAM, ERGAS, and $Q2^n$ [66]. Note that the higher value of PSNR and $Q2^n$ are, the more similar $\mathbf{u}_h$ and $\bar{\mathbf{u}}_h$, and the lower value of SAM and ERGAS are, the more similar both images. The settings of max iteration number and the stopping criterion of Alg. 5 were 5000 and $\|\mathbf{u}_h^{(n)} - \mathbf{u}_h^{(n+1)}\|/\|\mathbf{u}_h^{(n)}\| < 1.0 \times 10^{-4}$, respectively.

Tab. 4.4 shows PSNR[dB], SAM, ERGAS and $Q2^n$ of the estimated HS images by the existing and proposed methods for $(\sigma_H, \sigma_g) = (0.1,\ 0.04)$ and $(0.1,\ 0.06)$. At the time, its values are the average of the results for all HS images. In Tab. 4.4, one can see that for all the quality measures and for both noise intensity, the proposed method outperforms all the existing methods. By comparison between the proposed by HTV and HSSTV, in the almost PSNR, SAM and ERGAS cases, HTV is higher quality than HSSTV. We think that since an MS image has weaker spectral correlation than an HS image, it hardly necessary to evaluate the spatio-spectral piecewise smoothness of an MS image. The other hands, in $Q2^n$, the result of HSSTV and $p = 2$ is best. Since $Q2^n$ evaluates the structure information and spectral/spatial distortion, the result of HSSTV have more correct detail than that of HTV.

Fig. 4.9 is the estimated high HS images in the case of $(\sigma_H, \sigma_g) = (0.1, 0.04)$ and *DC*. They are depicted as RGB images, where R, G, and B bands were set to the 30th, 60th and 90th bands of them in the case of the HS images, and these three bands are set as (R, G, B) $= (2, 4, 6)$ bands in the MS image. One can see that the results by existing methods have artifacts and spectral distortion. Specifically, the results using MTF-GLP, MAPSMM, and CNMF have many artifacts, so that the spatial smoothness of them are lost. In the HySure case, the result almost does not have artifacts. However, since the color of the result changes compared with the original HS image, HySure produces the spectral distortion. In contrast, the proposed methods avoid artifacts and spectral distortion. In addition, HSSTV preserves more edge than HTV.

4.2.5 Compressed Hyperspecteral Pansharpening

HS images are usually captured by dispersing the incident light, HS imaging requires a 2D spectral sensor for 1D spatial information. This means that capturing an HS image requires much time, and it is impossible to acquire it in one shot. To tackle the above problem, the concept of CS plays a very essential role [49, 50], and one-shot HS imaging based on CS is actively studied [52, 53].

HS imaging has another dilemma: capturing an HR-HS image itself is a challenging task described in Sec. 4.2. HS image fusion resolves this dilemma, but existing HS image fusion techniques [114–116,126–130] do not consider CS-based one-shot imaging scenarios. Some MS image fusion methods involving the CS model have been proposed in [131–133]. However, since they assume that a given MS image only has 4 channel information (red, green, blue, and infrared radiation), utilizing the spectral information of MS images would be less important than that of HS images.

Based on the above discussion, we bridge the gap between the said two approaches for HS imaging. Specifically, we propose a novel HS imaging methodology, an HS pansharpening involving the CS model, named *compressed HS pansharpening* (CHPAN). The concept enables to generate an HR-HS image from a compressed LR-HS image with the help of a PAN image. For realistic setting, the concept assumes that both a CS observation and a PAN image are contaminated by noise. Then, an HR-HS and a clean PAN images are simultaneously estimated from the noisy pair. This process is formulated as an optimization problem involving an effective spatio-spectral regularization [10, 11]. After reformulation, the problem can be efficiently solved by a primal-dual splitting method [17], which is a proximal splitting algorithm applied to a variety of imaging problems [85, 97, 134, 135].

Proposed Framework

In this methodology, a compressed LR-HS image $\mathbf{v}_{CHS} \in \mathbb{R}^M$ is assumed to be given by $\mathbf{v}_{CHS} = \mathbf{\Phi S B}\bar{\mathbf{u}} + \mathbf{n}_{CHS}$, where $\mathbf{\Phi} \in M \times rNB (M \leq rNB)$ is a compressed sensing matrix and $\mathbf{n}_{CHS}$ is an additive white Gaussian noise with standard deviations σ_{CHS}. We assume a PAN observation $\mathbf{p} \in \mathbb{R}^N$ like (4.9) with $M = N$.

To estimate an HR-HS image $\mathbf{u}$ and a clear PAN image $\mathbf{q}$ from the above two observations $\mathbf{v}_{CHS}$ and $\mathbf{p}$, we formulate a CHPAN as the following optimization problem:

$$\begin{aligned} &\min_{\mathbf{u},\mathbf{q}} \mathrm{HSSTV}(\mathbf{u}) + \lambda \|\mathbf{Du} - \mathbf{DMq}\|_{1,2} + \|\mathbf{Dq}\|_{1,2} \\ &\text{s.t.} \quad \begin{bmatrix} \mathbf{\Phi SBu} \in \mathcal{B}_{2,\varepsilon}^{\mathbf{v}_{CHS}} := \{\mathbf{x} \in \mathbb{R}^M | \|\mathbf{x} - \mathbf{v}_{CHS}\| \leq \varepsilon\}, \\ \mathbf{q} \in \mathcal{B}_{2,\eta}^{\mathbf{p}} := \{\mathbf{x} \in \mathbb{R}^N | \|\mathbf{x} - \mathbf{p}\| \leq \eta\}, \\ \mathbf{u} \in [\underline{\mu_{\mathbf{u}}}, \overline{\mu_{\mathbf{u}}}]^{NB}, \\ \mathbf{q} \in [\underline{\mu_{\mathbf{q}}}, \overline{\mu_{\mathbf{q}}}]^{N}, \end{bmatrix} \end{aligned} \tag{4.12}$$

where $\mathbf{M} \in \mathbb{R}^{NB \times N}$ is a linear operator that replicates a PAN image B times along the spectral direction. This problem is equals to Prob. (4.10) replacing $\mathbf{SBu}$ with $\mathbf{\Phi SBu}$ in the first constraint. Therefore, the problem can be solved by Alg. 5 replacing $\mathbf{B}^\top\mathbf{S}^\top$ in the step 2 of with $\mathbf{B}^\top\mathbf{S}^\top\mathbf{\Phi}^\top$ and $\mathbf{SB}$ in the step 7 with $\mathbf{\Phi SB}$.

Table 4.5: Performance comparison with four quality measures (left: $m = 0.25$ (CHPAN case) and $r = 4$ (HS pansharpening case); right: $m = 0.0625$ (CHPAN case) and $r = 16$ (HS pansharpening case)).

quality measures / methods	$r = 4$ and $m = 0.25$				$r = 16$ and $m = 0.0625$			
	PSNR	SSIM	SAM	$Q2^n$	PSNR	SSIM	SAM	$Q2^n$
HS pansharpening (p = 1)	31.95	0.8526	8.038	0.8417	29.23	0.7606	10.22	0.7616
HS pansharpening (p = 2)	31.97	0.8528	**8.014**	0.8419	29.24	0.7608	**10.20**	0.7617
CHPAN (p = 1)	33.12	0.8817	8.284	0.8566	30.24	0.8008	10.77	0.7908
CHPAN (p = 2)	**33.14**	**0.8819**	8.259	**0.8568**	**30.25**	**0.8011**	10.75	**0.7910**

Experiments

We illustrate the utility of the proposed methodology and the estimation method. In the experiment, we generate a pair of a CS observation and a noisy PAN image from a true HR-HS image based on the observation model, and estimate an HR-HS image from the pair.

For the true HR-HS image, we used a Moffett field dataset, where we cropped a region of size $256 \times 128 \times 176$ and normalized its dynamic range into $[0, 1]$. The matrix $\mathbf{R}$ in (4.9) was set to an weighted-average matrix, whose weights w_i ($i = 1, \ldots, B$) were defined as $w_i = 1$ for $1 \leq i \leq 41$ and 0 otherwise. We set the standard deviations σ_{CHS} and σ_g of additive white Gaussian noises $\mathbf{n}_{CHS}$ and $\mathbf{n}_g$ as 0.1 and 0.04, respectively, and the sensing matrix $\mathbf{\Phi}$ is a direct random-sampling matrix, where we examined two sampling rates $m = 0.25$ and 0.0625.

We compared the results by CHPAN with that by HS pansharpening. We examined two downsampling rates of $\mathbf{S}$ of HS pansharpening in (4.8), which are $r = 4$ and 16, and then the HS pansharpening method with these rates were compared with the CHPAN method with $m = 0.25$ and $m = 0.0625$, respectively. By this setting, the amount of information in the observed HS image on the HS pansharpening experiment is equal to that on the CHPAN experiment. Then, $\mathbf{B}$ was set to 5×5 and 9×9 Gaussian blur matrixes in the case of $r = 4$ and 16.

The parameters ω in (3.6) and λ in (4.12) are set as 0.01 and 0.1, respectively. For our CHPAN method, the parameters in (4.12) were set to $\varepsilon = \|\mathbf{v}_{CHS} - \mathbf{\Phi}\bar{\mathbf{u}}\|$ and $\eta = \|\mathbf{p} - \bar{\mathbf{p}}\|$, where $\bar{\mathbf{p}}$ is a noise-less PAN image. We set the max iteration number and the stopping criterion of the primal-dual splitting method to 5000 and $\|\mathbf{u}^{(n)} - \mathbf{u}^{(n+1)}\|/\|\mathbf{u}^{(n)}\| < 1.0 \times 10^{-4}$, respectively. The parameters in HS pansharpening were also set in the same way.

We use four quality measures: PSNR[dB], SSIM, SAM, and $Q2^n$. The larger the values of PSNR, SSIM, and $Q2^n$ are, the more similar the estimated and true HS images are. Likewise, the smaller the values of SAM is, the closer the two images are.

Tab. 4.5 shows PSNR[dB], SSIM, SAM, and $Q2^n$ of the estimated HS images by HS pansharpening and CHPAN. For PSNR, SSIM, and $Q2^n$, one can see that the CHPAN method achieves to estimate better images than the HS pansharpening method. For SAM, we will discuss later with Fig. 4.11.

Fig. 4.10 depicts the estimated HR-HS images as RGB images, where R, G, and B

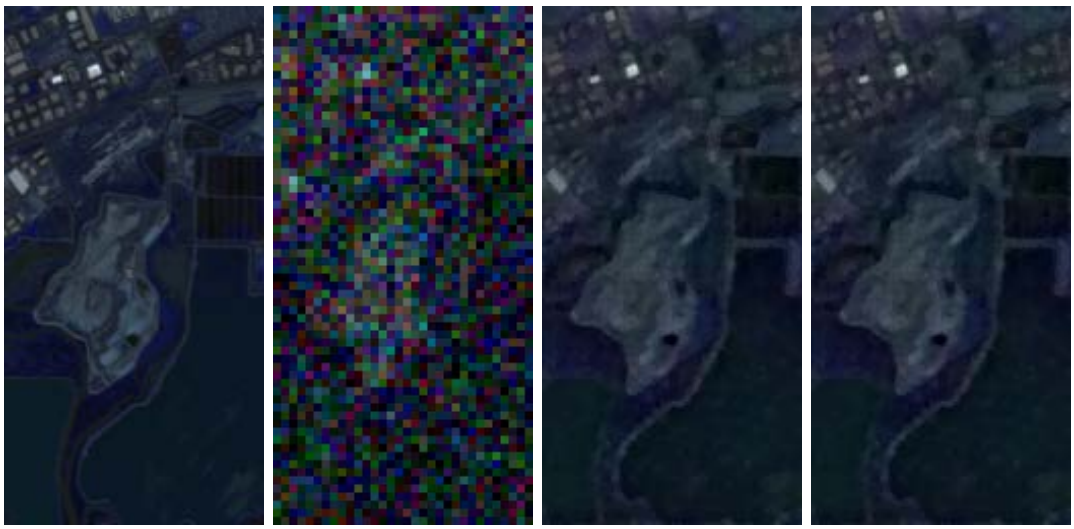

ground-truth | HS pansharpening observation | HS pansharpening ($p = 1$) | HS pansharpening ($p = 2$)

CHPAN observation | CHPAN ($p = 1$) | CHPAN ($p = 2$)

Figure 4.10: Resulting HS images ($m = 0.0625$ (CHPAN case) and $r = 16$ (HS pansharpening case)).

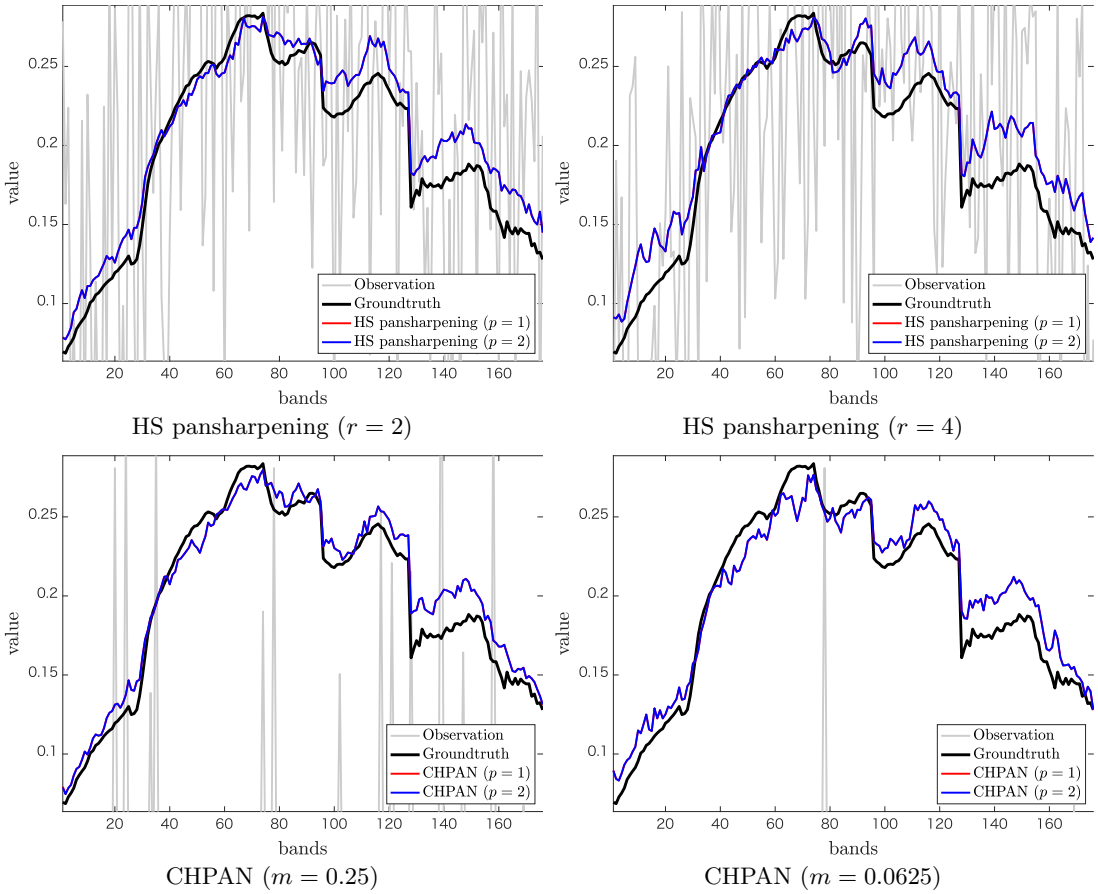

Figure 4.11: Spectral response of the results.

bands were set to the 8th, 16th and 32nd bands of them. The figure shows that the results of the CHPAN method are clearer and closer to the ground-truth than those by the HS pansharpening method.

In Fig. 4.11, we show the spectral responses of the results in Fig. 4.10. Specially, we picked the spectral vectors of 58th row of 78th col from the results. One can see that HS pansharpening changes the spectral variation between the 90 and 100 bands in the ground-truth. On the other hand, CHPAN results in spectral variation similar to the original one. As in Tab. 4.5, we found that the value of SAM of the result by CHPAN is slightly larger than that by HS pansharpening. Here, Tab. 4.5 shows that SAM value by the result on CHPAN is slightly larger than that on HS pansharpening. SAM evaluates the similarity of the spectral angles of two HS images. In other words, it ignores the error (distance) between the spectral values of the two images. This means that even if the error between two spectral responses is large, SAM is small (smaller is better) as long as the shapes of the spectral responses of two HS images are similar. As can be seen in Fig. 4.11, CHPAN estimates a more similar spectral response to the ground-truth than HS pansharpening, despite the fact that CHPAN is slightly inferior to HS pansharpening

in terms of SAM.

Chapter 5

Conclusion

In this paper, we have proposed new robust methods for image restoration and fusion via constrained convex optimization. In Chap. 1, we have explained the main technique, image restoration. Images are affected by many types of degradations and noises, so image restoration methods require robustness. Existing image restoration methods based on optimization achieve high-quality restoration, but the methods have several problems: not fully evaluating apriori knowledge on image and not considering outlier and/or modeling error. To resolve the issue, our proposed methods offer the following merits: (i) the full evaluation of apriori knowledge on an image by a new regularization technique, (ii) the evaluation of the sparsity of outlier, and (iii) the effective employment of multiple images with different characteristics.

In Chap. 2, we have introduced mathematical notation and abbreviation used in this paper, and then we have explained proximal tools and algorithms solving a convex optimization problem, e.g., ADMM and the primal-dual splitting method.

We have introduced our proposed image restoration and fusion methods in Chap. 3 and Chap. 4, respectively. In Chap. 3, we focus on HS images, because they are easily affected by degradations and noises. For robust restoration, at first, we have proposed a new regularization technique, named HSSTV. Our regularization evaluates spatial and spectral piecewise smoothness on HS images as apriori knowledge. Next, we have formulated constrained optimization problems using HSSTV for HS image denoising and CS reconstruction. The problems evaluate the sparsity of outliers, so the proposed methods achieve robust restoration for outliers. Besides, data-fidelity and the sparsity of outlier are evaluated by hard constraints, leading to intuitive parameter settings. Then, we have solved them with ADMM after reformulation. In the simulation experiments, we have illustrated the advantage of the proposed methods over existing methods for several image restoration problem: Gaussian noise removal, Gaussian-sparse mixed noise removal, and CS reconstruction. Besides, we have confirmed the performance of the proposed methods for real noise removal.

The approach (iii) is called image fusion, and we have proposed new robust image fusion methods for two situations: blur and noisy image fusion and image fusion for super-resolution. The former estimates a desirable image from a pair of observed blur and noisy images, and the latter estimates an HR-HS image from an observed LR-HS

image and a guide image. Our proposed methods assume that all observations have noise and estimate a desirable image by solving constrained optimization problems. Since our proposed methods fully utilize information in both observations by evaluating the data-fidelity and/or the edge similarity between them, the methods achieve high-quality robust image fusion. We have demonstrated the performance of the proposed methods for image fusion problems. Besides, the results show that the proposed methods are robust for modeling error because they can effectively utilize information in both observations.

In the above results and discussion, for image restoration and fusion, one can see that our proposed methods are robust for noises, degradations, and modeling error. In this work, we have mainly conducted simulation experiments, and the degradation and sensing operators are ideally set. Therefore, the performance of the methods should be verified for a real situation. In the future, we intend to confirm the performance using real datasets, real estimated operators, and a real imaging system.

Chapter 6

Acknowledgement

I would like to thank Professor Itsuo Kumazawa and Associate Professor Shunsuke Ono for kind supervision. I would like to express my heartfelt gratitude to all the people in Kumazawa laboratory, Mathematical Data Informatics Laboratory, and Augmented Vision Laboratory who spent time with me during my student life and gave me various supports. I would like also to deeply thank Professor Masahiro Yamaguchi, Professor Isao Yamada, and Associate Professor Takahiro Shinozaki, Tokyo Institute of Technology, Japan, for serving as members of the examining committee of this dissertation. I am grateful to my family and friends for mentally supporting me.

This work was supported by Japan Society for the Promotion of Science (JSPS), Research Fellow (DC1) grant.

References

[1] D. Gabay and B. Mercier, "A dual algorithm for the solution of nonlinear variational problems via finite elements approximations," *Comput. Math. Appl.*, vol. 2, pp. 17–40, 1976.

[2] J. Eckstein and D.P. Bertsekas, "On the Douglas-Rachford splitting method and proximal point algorithm for maximal monotone operators," *Math. Program.*, vol. 55, pp. 293–318, 1992.

[3] J. Eckstein and D. P. Bertsekas, "On the Douglas—Rachford splitting method and the proximal point algorithm for maximal monotone operators," *Math. Program.*, vol. 55, no. 1-3, pp. 293–318, 1992.

[4] S. Boyd, N. Parikh, E. Chu, B. Peleato, and J. Eckstein, "Distributed optimization and statistical learning via the alternating direction method of multipliers," *Foundations and Trends in Machine Learning*, vol. 3, no. 1, pp. 1–122, 2011.

[5] H. Zhang, W. He, L. Zhang, H. Shen, and Q. Yuan, "Hyperspectral image restoration using low-rank matrix recovery," *IEEE Trans. on Geosci. and Remote Sens.*, vol. 52, no. 8, pp. 4729–4743, 2014.

[6] Q. Yuan, L. Zhang, and H. Shen, "Hyperspectral image denoising employing a spectral–spatial adaptive total variation model," *IEEE Trans. on Geosci. and Remote Sens.*, vol. 50, no. 10, pp. 3660–3677, 2012.

[7] H. K. Aggarwal and A. Majumdar, "Hyperspectral image denoising using spatio-spectral total variation," *IEEE Geosci. and Remote Sens. Lett.*, vol. 13, no. 3, pp. 442–446, 2016.

[8] S. H. Chan, R. Khoshabeh, K. B. Gibson, P. E. Gill, and T. Q. Nguyen, "An augmented lagrangian method for total variation video restoration," *IEEE Trans. Image Process.*, vol. 20, no. 11, pp. 3097–3111, 2011.

[9] H. Liu, P. Sun, Q. Du, Z. Wu, and Z. Wei, "Hyperspectral image restoration based on low-rank recovery with a local neighborhood weighted spectral-spatial total variation model," *IEEE Trans. on Geosci. and Remote Sens.*, vol. 57, no. 3, pp. 1–14, 2018.

[10] S. Takeyama, S. Ono, and I. Kumazawa, "Hyperspectral image restoration by hybrid spatio-spectral total variation," *Proc. IEEE Int. Conf. Acoust., Speech, Signal Process. (ICASSP)*, pp. 4586–4590, 2017.

[11] S. Takeyama, S. Ono, and I. Kumazawa, "A constrained convex optimization approach to hyperspectral image restoration with hybrid spatio-spectral regularization," *Remote Sensing*, vol. 12, no. 21, pp. 3541, 2020.

[12] W. He, H. Zhang, L. Zhang, and H. Shen, "Total-variation-regularized low-rank matrix factorization for hyperspectral image restoration," *IEEE Trans. on Geosci. and Remote Sens.*, vol. 54, no. 1, pp. 178–188, 2016.

[13] Q. Wang, Z. Wu, J. Jin, T. Wang, and Y. Shen, "Low rank constraint and spatial spectral total variation for hyperspectral image mixed denoising," *Signal Processing*, vol. 142, pp. 11–26, 2018.

[14] F.A. Kruse, A.B. Lefkoff, J.W. Boardman, K.B. Heidebrecht, A.T. Shapiro, P.J. Barloon, and A.F.H. Goetz, "The spectral image processing system (SIPS)—interactive visualization and analysis of imaging spectrometer data," *Remote Sensing of Environment*, vol. 44, no. 2, pp. 145–163, 1993.

[15] L. Wald, "Quality of high resolution synthesised images: Is there a simple criterion?," in *Third conference" Fusion of Earth data: merging point measurements, raster maps and remotely sensed images"*, 2000, pp. 99–103.

[16] J. J. Moreau, "Fonctions convexes duales et points proximaux dans un espace hilbertien," *C. R. Acad. Sci. Paris Ser. A Math.*, vol. 255, pp. 2897–2899, 1962.

[17] A. Chambolle and T. Pock, "A first-order primal-dual algorithm for convex problems with applications to imaging," *J. Math. Imaging and Vision*, vol. 40, no. 1, pp. 120–145, 2010.

[18] P. L. Combettes and J.-C. Pesquet, "Proximal splitting methods in signal processing," in *Fixed-Point Algorithms for Inverse Problems in Science and Engineering*, pp. 185–212. Springer-Verlag, 2011.

[19] C. I. Chang, *Hyperspectral imaging: techniques for spectral detection and classification*, vol. 1, Springer Science & Business Media, 2003.

[20] A. Plaza et al., "Recent advances in techniques for hyperspectral image processing," *Remote sensing of environment*, vol. 113, pp. S110–S122, 2009.

[21] Behnood Rasti, Paul Scheunders, Pedram Ghamisi, Giorgio Licciardi, and Jocelyn Chanussot, "Noise reduction in hyperspectral imagery: Overview and application," *Remote Sens.*, vol. 10, no. 3, pp. 482, 2018.

[22] Y. Chang, L. Yan, H. Fang, and C. Luo, "Anisotropic spectral-spatial total variation model for multispectral remote sensing image destriping," *IEEE Trans. Image Process.*, vol. 24, no. 6, pp. 1852–1866, 2015.

[23] L. Sun, C. Ma, Y. Chen, Y. Zheng, H.J. Shim, Z. Wu, and B. Jeon, "Low rank component induced spatial-spectral kernel method for hyperspectral image classification," *IEEE Trans. Circuits Syst. Video Technol.*, pp. 4133–4148, 2019.

[24] H. Li, P. Sun, H. Liu, Z. Wu, and Z. Wei, "Non-convex low-rank approximation for hyperspectral image recovery with weighted total varaition regularization," in *Proc. IEEE Int. Geosci. and Remote Sens. Symposium (IGARSS)*, 07 2018, pp. 2733–2736.

[25] H. K. Aggarwal and A. Majumdar, "Hyperspectral unmixing in the presence of mixed noise using joint-sparsity and total variation," *IEEE Sel. Top. Appl. Earth Obs. Remote Sens.*, vol. 9, no. 9, pp. 4257–4266, 2016.

[26] L. Sun, F. Wu, T. Zhan, W. Liu, J. Wang, and B. Jeon, "Weighted nonlocal low-rank tensor decomposition method for sparse unmixing of hyperspectral images.," *IEEE Sel. Top. Appl. Earth Obs. Remote Sens.*, pp. 1174–1188, 2020.

[27] W. He, H. Zhang, H. Shen, and L. Zhang, "Hyperspectral image denoising using local low-rank matrix recovery and global spatial–spectral total variation," *IEEE Sel. Top. Appl. Earth Obs. Remote Sens.*, vol. 11, no. 3, pp. 713–729, 2018.

[28] W. Cao, K. Wang, G. Han, J. Yao, and A. Cichocki, "A robust pca approach with noise structure learning and spatial–spectral low-rank modeling for hyperspectral image restoration," *IEEE Sel. Top. Appl. Earth Obs. Remote Sens.*, vol. 11, no. 10, pp. 3863–3879, 2018.

[29] Y. Wang, J. Peng, Q. Zhao, Y. Leung, X. Zhao, and D. Meng, "Hyperspectral image restoration via total variation regularized low-rank tensor decomposition," *IEEE Sel. Top. Appl. Earth Obs. Remote Sens.*, vol. 11, no. 4, pp. 1227–1243, 2017.

[30] L. Sun, T. Zhan, Z. Wu, L. Xiao, and B. Jeon, "Hyperspectral mixed denoising via spectral difference-induced total variation and low-rank approximation," *Remote Sens.*, vol. 10, no. 12, pp. 1956, 2018.

[31] T. Ince, "Hyperspectral image denoising using group low-rank and spatial-spectral total variation," *IEEE Access*, vol. 7, pp. 52095–52109, 2019.

[32] X. Kong, Y. Zhao, J. Xue, J. CW. Chan, Z. Ren, HX. Huang, and J. Zang, "Hyperspectral image denoising based on nonlocal low-rank and tv regularization," *Remote Sensing*, vol. 12, no. 12, pp. 1956, 2020.

[33] X. Bresson and T. F. Chan, "Fast dual minimization of the vectorial total variation norm and applications to color image processing," *Inverse Probl. Imag.*, vol. 2, no. 4, pp. 455–484, 2008.

[34] L. Sun, C. He, Y. Zheng, and S. Tang, "Slrl4d: Joint restoration of subspace low-rank learning and non-local 4-d transform filtering for hyperspectral image.," *Remote Sens.*, p. 2979, 2020.

[35] M. Afonso, J. Bioucas-Dias, and M. Figueiredo, "An augmented Lagrangian approach to the constrained optimization formulation of imaging inverse problems," *IEEE Trans. Image Process.*, vol. 20, no. 3, pp. 681–695, 2011.

[36] G. Chierchia, N. Pustelnik, J.-C. Pesquet, and B. Pesquet-Popescu, "Epigraphical projection and proximal tools for solving constrained convex optimization problems," *Signal, Image and Video Process.*, pp. 1–13, 2014.

[37] S. Ono and I. Yamada, "Signal recovery with certain involved convex data-fidelity constraints," *IEEE Trans. Signal Process.*, vol. 63, no. 22, pp. 6149–6163, 2015.

[38] Y. Xie, Y. Qu, D. Tao, W. Wu, Q. Yuan, and W. Zhang, "Hyperspectral image restoration via iteratively regularized weighted schatten p-norm minimization," *IEEE Trans. on Geosci. and Remote Sens.*, vol. 54, no. 8, pp. 4642–4659, 2016.

[39] S. Ono, "L_0 gradient projection," *IEEE Trans. Image Process.*, vol. 26, no. 4, pp. 1554–1564, 2017.

[40] S. Takeyama, S. Ono, and I. Kumazawa, "Robust and effective hyperspectral pansharpening using spatio-spectral total variation," in *Proc. IEEE Int. Conf. Acoust., Speech, Signal Process. (ICASSP)*, 2018, pp. 1603–1607.

[41] S. Takeyama, S. Ono, and I. Kumazawa, "Hyperspectral pansharpening using noisy panchromatic image," in *Asia-Pacific Signal and Information Processing Association Annual Summit and Conference (APSIPA ASC)*, 2018, pp. 880–885.

[42] S. Takeyama, S. Ono, and I. Kumazawa, "Hyperspectral and multispectral data fusion by a regularization considering," in *Proc. IEEE Int. Conf. Acoust., Speech, Signal Process. (ICASSP)*, 2019, pp. 2152–2156.

[43] Z. Wang, A. C. Bovik, H. R. Sheikh, and E. P. Simoncelli, "Image quality assessment: from error visibility to structural similarity," *IEEE Trans. Image Process.*, vol. 13, no. 4, pp. 600–612, 2004.

[44] "Spectir," http://www.spectir.com/free-data-samples/.

[45] "Multispec," https://engineering.purdue.edu/ biehl/MultiSpec.

[46] "GIC," http://www.ehu.eus/ccwintco/index.php?title=Hyperspectral_Remote_Sensing_Scenes.

[47] M. Maggioni, V. Katkovnik, K. Egiazarian, and A. Foi, "Nonlocal transform-domain filter for volumetric data denoising and reconstruction," *IEEE Trans. Image Process.*, vol. 22, no. 1, pp. 119–133, 2013.

[48] W. Liu and J. Lee, "A 3-d atrous convolution neural network for hyperspectral image denoising," *IEEE Trans. on Geosci. and Remote Sens.*, 2019.

[49] D. L. Donoho, "Compressed sensing," *IEEE Trans. Inform. Theory*, vol. 52, no. 4, pp. 1289–1306, 2006.

[50] E. Candès, J. Romberg, and T. Tao, "Robust uncertainty principles: exact signal reconstruction from highly incomplete frequency information," *IEEE Trans. Inform. Theory*, vol. 52, no. 2, pp. 489–509, 2006.

[51] J. Romberg, "Imaging via compressive sampling," *IEEE Signal Process. Magazine*, vol. 25, no. 2, pp. 14–20, 2008.

[52] R. M. Willett, M. F. Duarte, M. A. Davenport, and R. G. Baraniuk, "Sparsity and structure in hyperspectral imaging: Sensing, reconstruction, and target detection," *IEEE Signal Process. Magazine*, vol. 31, no. 1, pp. 116–126, 2014.

[53] G. R. Arce, D. J. Brady, L. Carin, H. Arguello, and D. S. Kittle, "Compressive coded aperture spectral imaging: An introduction," *IEEE Signal Process. Magazine*, vol. 31, no. 1, pp. 105–115, 2014.

[54] M. Golbabaee and P. Vandergheynst, "Hyperspectral image compressed sensing via low-rank and joint-sparse matrix recovery," in *Proc. IEEE Int. Conf. Acoust., Speech, Signal Process. (ICASSP)*, 2012, pp. 2741–2744.

[55] S. Yang, M. Wang, P. Li, L. Jin, B. Wu, and L. Jiao, "Compressive hyperspectral imaging via sparse tensor and nonlinear compressed sensing," *IEEE Trans. on Geosci. and Remote Sens.*, vol. 53, no. 11, pp. 5943–5957, 2015.

[56] J. Wei, Y. Huang, K. Lu, and L. Wang, "Nonlocal low-rank-based compressed sensing for remote sensing image reconstruction," *IEEE Geosci. and Remote Sens. Lett.*, vol. 13, no. 10, pp. 1557–1561, 2016.

[57] H. Garcia, C. V. Correa, and H. Arguello, "Multi-resolution compressive spectral imaging reconstruction from single pixel measurements," *IEEE Trans. Image Process.*, vol. 27, no. 12, pp. 6174–6184, 2018.

[58] P. C. Hansen, J. G. Nagy, and D. P. O'Leary, *Deblurring Images: Matrices, Spectra, and Filtering*, SIAM, 2006.

[59] G. H. Golub and C. F. Van Loan, *Matrix Computations*, Johns Hopkins University Press, 4th edition, 2012.

[60] P. L. Combettes and J.-C. Pesquet, "Primal-dual splitting algorithm for solving inclusions with mixtures of composite, Lipschitzian, and parallel-sum type monotone operators," *Set-Valued and Variational Analysis*, vol. 20, no. 2, pp. 307–330, 2012.

[61] L. Condat, "A primal-dual splitting method for convex optimization involving Lipschitzian, proximable and linear composite terms," *J. Optimization Theory and Applications*, 2013.

[62] S. Ono, M. Yamagishi, T. Miyata, and I. Kumazawa, "Image restoration using a stochastic variant of the alternating direction method of multipliers," in *Proc. IEEE Int. Conf. Acoust., Speech, Signal Process. (ICASSP)*, 2016.

[63] A. Chambolle, M. J. Ehrhardt, P. Richtárik, and C.-B. Schonlieb, "Stochastic primal-dual hybrid gradient algorithm with arbitrary sampling and imaging applications," *SIAM J. Optim.*, vol. 28, no. 4, pp. 2783–2808, 2018.

[64] P. L. Combettes and J.-C. Pesquet, "Stochastic forward-backward and primal-dual approximation algorithms with application to online image restoration," in *Proc. Eur. Signal Process. Conf. (EUSIPCO)*, Aug 2016, pp. 1813–1817.

[65] S. Ono, "Efficient constrained signal reconstruction by randomized epigraphical projection," in *Proc. IEEE Int. Conf. Acoust., Speech, Signal Process. (ICASSP)*, 2019, pp. 4993–4997.

[66] A. Garzelli and F. Nencini, "Hypercomplex quality assessment of multi/hyperspectral images," *IEEE Geosci. and Remote Sens. Lett.*, vol. 6, no. 4, pp. 662–665, 2009.

[67] Qi Shan, Jiaya Jia, and Aseem Agarwala, "High-quality motion deblurring from a single image," *ACM Transactions on Graphics*, vol. 27, no. 3, pp. 73:1–73:10, 2008.

[68] Sunghyun Cho and Seungyong Lee, "Fast motion deblurring," *ACM Transactions on Graphics*, vol. 28, no. 5, pp. 145:1–145:8, 2009.

[69] Jian-Feng Cai, Hui Ji, Chaoqiang Liu, and Zuowei Shen, "Blind motion deblurring from a single image using sparse approximation," in *Proc. IEEE Conf. Comput. Vis. Pattern Recognit. (CVPR)*, 2009, pp. 104–111.

[70] Li Xu and Jiaya Jia, "Two-phase kernel estimation for robust motion deblurring," in *Proc. Eur. Conf. Comput. Vis. (ECCV)*, 2010, pp. 157–170.

[71] Dilip Krishnan, Terence Tay, and Rob Fergus, "Blind deconvolution using a normalized sparsity measure," in *Proc. IEEE Conf. Comput. Vis. Pattern Recognit. (CVPR)*, 2011, pp. 233–240.

[72] Jian-Feng Cai, Hui Ji, Chaoqiang Liu, and Zuowei Shen, "Framelet-based blind motion deblurring from a single image," *IEEE Trans. Image Process.*, vol. 21, no. 2, pp. 562–572, 2012.

[73] Lin Zhong, Sunghyun Cho, Dimitris Metaxas, Sylvain Paris, and Jue Wang, "Handling noise in single image deblurring using directional filters," in *Proc. IEEE Conf. Comput. Vis. Pattern Recognit. (CVPR)*, 2013, pp. 612–619.

[74] Tomer Michaeli and Michal Irani, "Blind deblurring using internal patch recurrence," in *Proc. Eur. Conf. Comput. Vis. (ECCV)*, 2014, pp. 783–798.

[75] Daniele Perrone and Paolo Favaro, "A clearer picture of total variation blind deconvolution," *IEEE Trans. Pattern Anal. Mach. Intell.*, vol. 38, no. 6, pp. 1041–1055, 2016.

[76] Wei-Sheng Lai, Jia-Bin Huang, Zhe Hu, Narendra Ahuja, and Ming-Hsuan Yang, "A comparative study for single image blind deblurring," in *Proc. IEEE Conf. Comput. Vis. Pattern Recognit. (CVPR)*, 2016, pp. 1701–1709.

[77] L. Yuan, J. Sun, L. Quan, and H. Y. Shum, "Image deblurring with blurred/noisy image pairs," *ACM Transactions on Graphics*, vol. 26, no. 3, pp. 1:1–1:10, 2007.

[78] S. Lee, H.M. Park, and S.Y. Hwang, "Motion deblurring using edge map with blurred/noisy image pairs," *Optics Communications*, vol. 285, no. 7, pp. 1777–1786, 2012.

[79] C. Je, H. S. Jeon, C.H. Son, and H.M Park, "Disparity-based space-variant image deblurring," *Signal Process.: Image Commun.*, vol. 28, no. 7, pp. 792–808, 2013.

[80] H. Li, Y. Zhang, J. Sun, and D. Gong, "Joint motion deblurring with blurred/noisy image pair," in *Proc. Int. Conf. Pattern Recognit. (ICPR)*, 2014, pp. 1020–1024.

[81] C. H. Son and X. P. Zhang, "Layer-based approach for image pair fusion," *IEEE Trans. Image Process.*, vol. 25, no. 6, pp. 2866–2881, 2016.

[82] L. Zhong, S. Cho, D. Metaxas, S. Paris, and J. Wang, "Handling noise in single image deblurring using directional filters," in *Proc. IEEE Conf. Comput. Vis. Pattern Recognit. (CVPR)*, 2013, pp. 612–619.

[83] L. I. Rudin, S. Osher, and E. Fatemi, "Nonlinear total variation based noise removal algorithms," *Phys. D*, vol. 60, no. 1-4, pp. 259–268, 1992.

[84] B. Goldluecke, E. Strekalovskiy, and D. Cremers, "The natural vectorial total variation which arises from geometric measure theory," *SIAM J. Imag. Sci.*, vol. 5, no. 2, pp. 537–563, 2012.

[85] S. Ono and I. Yamada, "Decorrelated vectorial total variation," in *Proc. IEEE Conf. Comput. Vis. Pattern Recognit. (CVPR)*, 2014.

[86] S. Lefkimmiatis and A. Roussos.and P. Maragos.and M. Unser, "Structure tensor total variation," *SIAM J. Imag. Sci.*, vol. 8, no. 2, pp. 1090–1122, 2015.

[87] S. Ono, K. Shirai, and M. Okuda, "Vectorial total variation based on arranged structure tensor for multichannel image restoration," in *Proc. IEEE Int. Conf. Acoust., Speech, Signal Process. (ICASSP)*, 2016.

[88] S. Ono, "Distributed convex optimization via proximal splitting: A survey on admm-based approaches," *Journal of The Society of Instrument and Control Engineers*, vol. 55, no. 11, pp. 954–959, 2016, (in Japanese).

[89] S. Mallat, *A wavelet tour of signal processing*, Academic Press, 2nd edition, 1999.

[90] E. Candès, L. Demanet, D. L. Donoho, and L. Ying, "Fast discrete curvelet transforms," *SIAM J. Multi. Model. Simul.*, vol. 5, no. 3, pp. 861–899, 2006.

[91] G. Gilboa and S. Osher, "Nonlocal linear image regularization and supervised segmentation," *Multiscale Model. Simul.*, vol. 6, no. 2, pp. 595–630, 2007.

[92] A. Danielyan, V. Katkovnik, and K. Egiazarian, "BM3D frames and variational image deblurring," *IEEE Trans. Image Process.*, vol. 21, no. 4, pp. 1715–1728, 2012.

[93] G. Chierchia, N. Pustelnik, B. Pesquet-Popescu, and J.-C. Pesquet, "A nonlocal structure tensor-based approach for multicomponent image recovery problems," *IEEE Trans. Image Process.*, vol. 23, no. 12, pp. 5531–5544, 2014.

[94] J. Mairal, F. Bach, J. Ponce, G. Sapiro, and A. Zisserman, "Non-local sparse models for image restoration," in *Proc. IEEE Int. Conf. Comput. Vis. (ICCV)*, 2009.

[95] D. Zoran and Y. Weiss, "From learning models of natural image patches to whole image restoration," in *Proc. IEEE Int. Conf. Comput. Vis. (ICCV)*, 2011.

[96] S. Sreehari, S. V. Venkatakrishnan, B. Wohlberg, G. T. Buzzard, L. F. Drummy, J. P. Simmons, and C. A. Bouman, "Plug-and-play priors for bright field electron tomography and sparse interpolation," *IEEE Trans. Comput. Imag.*, vol. 2, no. 4, pp. 408–423, 2016.

[97] S. Ono, "Primal-dual plug-and-play image restoration," *IEEE Signal Process. Lett.*, vol. 24, no. 8, pp. 1108–1112, 2017.

[98] M. V. Afonso, J. M. Bioucas-Dias, and M. AT. Figueiredo, "An augmented lagrangian approach to the constrained optimization formulation of imaging inverse problems," *IEEE Trans. Image Process.*, vol. 20, no. 3, pp. 681–695, 2011.

[99] M. Carlavan and L. Blanc-Fèraud, "Sparse Poisson noisy image deblurring," *IEEE Trans. Image Process.*, vol. 21, no. 4, pp. 1834–1846, 2012.

[100] T. Teuber, G. Steidl, and R. H. Chan, "Minimization and parameter estimation for seminorm regularization models with I-divergence constraints," *Inverse Problems*, vol. 29, no. 3, 2013.

[101] H. H. Bauschke and P. L. Combettes, *Convex analysis and monotone operator theory in Hilbert spaces*, Springer, New York, 2011.

[102] D. Martin, C. Fowlkes, D. Tal, and J. Malik, "A database of human segmented natural images and its application to evaluating segmentation algorithms and measuring ecological statistics," in *Proc. IEEE Int. Conf. Comput. Vis. (ICCV)*, 2001.

[103] L. Loncan, L. B. de Almeida, J. M. Bioucas-Dias, X. Briottet, J. Chanussot, N. Dobigeon, S. Fabre, W. Liao, G. A. Licciardi, M. Simoes, et al., "Hyperspectral pansharpening: A review," *IEEE Geoscience and remote sensing magazine*, vol. 3, no. 3, pp. 27–46, 2015.

[104] N. Yokoya, C. Grohnfeldt, and J. Chanussot, "Hyperspectral and multispectral data fusion: A comparative review of the recent literature," *IEEE Geoscience and Remote Sensing Magazine*, vol. 5, no. 2, pp. 29–56, 2017.

[105] N. Yokoya, C. Grohnfeldt, and J. Chanussot, "Hyperspectral and multispectral data fusion: A comparative review of the recent literature," *IEEE Geosci. and Remote Sens. Magazine*, vol. 5, no. 2, pp. 29–56, 2017.

[106] P. Chavez, S. C. Sides, J. A. Anderson, et al., "Comparison of three different methods to merge multiresolution and multispectral data- landsat tm and spot panchromatic," *Photogrammetric Engineering and remote sensing*, vol. 57, no. 3, pp. 295–303, 1991.

[107] W. Liao, X. Huang, F. Van Coillie, S. Gautama, et al., "Processing of multiresolution thermal hyperspectral and digital color data: Outcome of the 2014 ieee grss data fusion contest," *IEEE Journal of Selected Topics in Applied Earth Observations and Remote Sensing*, vol. 8, no. 6, pp. 2984–2996, 2015.

[108] C. A. Laben and B. V. Brower, "Process for enhancing the spatial resolution of multispectral imagery using pan-sharpening," Jan. 4 2000, US Patent 6,011,875.

[109] B. Aiazzi, S. Baronti, and M. Selva, "Improving component substitution pansharpening through multivariate regression of ms + pan data," *IEEE Trans. on Geosci. and Remote Sens.*, vol. 45, no. 10, pp. 3230–3239, 2007.

[110] B. Aiazzi, L. Alparone, S. Baronti, A. Garzelli, and M. Selva, "Mtf-tailored multiscale fusion of high-resolution ms and pan imagery," *Photogrammetric Engineering & Remote Sensing*, vol. 72, no. 5, pp. 591–596, 2006.

[111] G. Vivone, R. Restaino, M. Dalla Mura, G. Licciardi, and J. Chanussot, "Contrast and error-based fusion schemes for multispectral image pansharpening," *IEEE Geoscience and Remote Sensing Letters*, vol. 11, no. 5, pp. 930–934, 2014.

[112] J. G. Liu, "Smoothing filter-based intensity modulation: A spectral preserve image fusion technique for improving spatial details," *International Journal of Remote Sensing*, vol. 21, no. 18, pp. 3461–3472, 2000.

[113] R. C. Hardie, M. T. Eismann, and G. L. Wilson, "Map estimation for hyperspectral image resolution enhancement using an auxiliary sensor," *IEEE Trans. Image Process.*, vol. 13, no. 9, pp. 1174 – 1184, 2004.

[114] Q. Wei, J. Bioucas-Dias, N. Dobigeon, and J. Y. Tourneret, "Hyperspectral and multispectral image fusion based on a sparse representation," *IEEE Trans. on Geosci. and Remote Sens.*, vol. 53, no. 7, pp. 3658 – 3668, 2015.

[115] M. Simões, J. Bioucas-Dias, L. B. Almeida, and J. Chanussot, "A convex formulation for hyperspectral image superresolution via subspace-based regularization," *IEEE Trans. on Geosci. and Remote Sens.*, vol. 53, no. 6, pp. 3373–3388, 2015.

[116] N. Yokoya, T. Yairi, and A. Iwasaki, "Coupled nonnegative matrix factorization unmixing for hyperspectral and multispectral data fusion," *IEEE Trans. on Geosci. and Remote Sens.*, vol. 50, no. 2, pp. 528–537, 2012.

[117] H. N. Gross and J. R. Schott, "Application of spectral mixture analysis and image fusion techniques for image sharpening," *Remote Sensing of Environment*, vol. 63, no. 2, pp. 85–94, 1998.

[118] C. Lanaras, E. Baltsavias, and K. Schindler, "Hyperspectral super-resolution by coupled spectral unmixing," in *Proceedings of the IEEE International Conference on Computer Vision*, 2015, pp. 3586–3594.

[119] Y. Zhang, Y. Gao, Y. Liu, and M. He, "Hyperspectral and multispectral image fusion based on constrained cnmf unmixing," in *2015 7th Workshop on Hyperspectral Image and Signal Processing: Evolution in Remote Sensing (WHISPERS)*, 2015, pp. 1–4.

[120] M. T. Eismann, *Resolution enhancement of hyperspectral imagery using maximum a posteriori estimation with a stochastic mixing model*, Ph.D. dissertation, Dept. Electrical and Computer Engineering, Univ. Dayton, OH, 2004.

[121] Q. Wei, N. Dobigeon, and J. Y. Tourneret, "Fast fusion of multi-band images based on solving a sylvester equation," *IEEE Transactions on Image Processing*, vol. 24, no. 11, pp. 4109–4121, 2015.

[122] C. Chen, Y. Li, W. Liu, and J. Huang, "Image fusion with local spectral consistency and dynamic gradient sparsity," in *Proc. IEEE Conf. Comput. Vis. Pattern Recognit. (CVPR)*, 2014, pp. 2760–2765.

[123] C.I. Chang and Q. Du, "Interference and noise-adjusted principal components analysis," *IEEE Trans. on Geosci. and Remote Sens.*, vol. 37, no. 5, pp. 2387–2396, 1999.

[124] L. Wald, T. Ranchin, and M. Mangolini, "Fusion of satellite images of different spatial resolutions: Assessing the quality of resulting images," *Photogrammetric Engineering & Remote Sensing*, vol. 63, no. 6, pp. 691–699, 1997.

[125] N. Yokoya and A. Iwasaki, "Airborne hyperspectral data over chikusei," Tech. Rep., Space Application Laboratory, University of Tokyo, Japan, May 2016.

[126] G. Scarpa, S. Vitale, and D. Cozzolino, "Target-adaptive cnn-based pansharpening," *IEEE Trans. on Geosci. and Remote Sens.*, vol. 56, no. 9, pp. 5443–5457, 2018.

[127] C. Kwan, J. H. Choi, S. H. Chan, J. Zhou, and B. Budavari, "A super-resolution and fusion approach to enhancing hyperspectral images," *Remote Sensing*, vol. 10, no. 9, pp. 1416, 2018.

[128] P. Liu and L. Xiao, "Multicomponent driven consistency priors for simultaneous decomposition and pansharpening," *IEEE Sel. Top. Appl. Earth Obs. Remote Sens.*, vol. 12, no. 11, pp. 4589–4605, 2019.

[129] X. Luo, J. Yin, X. Luo, and X. Jia, "A novel adversarial based hyperspectral and multispectral image fusion," *Remote Sensing*, vol. 11, no. 5, pp. 492, 2019.

[130] W. Xie, J. Lei, Y. Cui, Y. Li, and Q. Du, "Hyperspectral pansharpening with deep priors," *IEEE Trans. Neural Netw. Learn. Syst.*, 2019.

[131] S. Li and B. Yang, "A new pan-sharpening method using a compressed sensing technique," *IEEE Trans. on Geosci. and Remote Sens.*, vol. 49, no. 2, pp. 738–746, 2010.

[132] C. Jiang, H. Zhang, H. Shen, and L. Zhang, "A practical compressed sensing-based pan-sharpening method," *IEEE Geosci. Remote Sensing Lett.*, vol. 9, no. 4, pp. 629–633, 2011.

[133] W. Wang, L. Jiao, S. Yang, and K. Rong, "Distributed compressed sensing-based pan-sharpening with hybrid dictionary," *Neurocomputing*, vol. 155, pp. 320–333, 2015.

[134] E. Y. Sidky, J. H. Jørgensen, and X. Pan, "Convex optimization problem prototyping for image reconstruction in computed tomography with the chambolle–pock algorithm," *Physics in medicine and biology*, vol. 57, no. 10, pp. 3065, 2012.

[135] C. Sutour, C.-A. Deledalle, and J.-F. Aujol, "Adaptive regularization of the nl-means: Application to image and video denoising," *IEEE Trans. Image Process.*, vol. 23, no. 8, pp. 3506–3521, 2014.

Publications related to this dissertation

Article in Journal Papers

[J1] S. Takeyama, S. Ono, and I. Kumazawa, "Image restoration with multiple hard constraints on data-fidelity to blurred/noisy image pair," IEICE Transactions on Information and Systems, vol. E100-D, no.9, pp. 1953-1961, Sep. 2017.

[J2] S. Takeyama, S. Ono, and I. Kumazawa, "A constrained convex optimization approach to hyperspectral image restoration with hybrid spatio-spectral regularization," Remote Sensing, vol. 12, pp. 3541, 2020.

Peer-Reviewed Articles in International Conference

[C1] S. Takeyama, S. Ono, and I. Kumazawa, "Hyperspectral image restoration by hybrid spatio-spectral total variation," IEEE International Conference on Acoustics, Speech, and Signal Processing (ICASSP), New Orleans, LA, pp. 4586-4590, Mar. 2017.

[C2] S. Takeyama, S. Ono, and I. Kumazawa, "Robust and effective hyperspectral pansharpening using spatio-spectral total variation," IEEE International Conference on Acoustics, Speech, and Signal Processing (ICASSP), Calgary, Canada, pp. 1603-1607, Apr. 2018.

[C3] S. Takeyama, S. Ono, and I. Kumazawa, "Hyperspectral image restoration and pansharpening," APSIPA Annual Summit and Conference (APSIPA ASC), Honolulu, Hawaii, 1 pages, Nov. 2018.

[C4] S. Takeyama, S. Ono, and I. Kumazawa, "Hyperspectral pansharpening using noisy panchromatic image," APSIPA Annual Summit and Conference (APSIPA ASC), Honolulu, Hawaii, 6 pages, Nov. 2018.

[C5] S. Takeyama, S. Ono, and I. Kumazawa, "Hyperspectral and multispectral data fusion by a regularization considering," IEEE International Conference on Acoustics, Speech, and Signal Processing (ICASSP), Brighton, UK, pp. 2152-2156, May 2019.

[C6] S. Takeyama, S. Ono, and I. Kumazawa, "Mixed noise removal for hyperspectral images using hybrid spatio-spectral total variation," IEEE International Conference

on Image Processing (ICIP), virtual conference, pp. 3128-3132, Sep. 2019.

[C7] S. Takeyama and S. Ono, "Joint mixed-noise removal and compressed sensing reconstruction of hyperspectral image via convex optimization," IEEE International Geoscience and Remote Sensing Symposium (IGARSS), virtual symposium, Sep. 2020.

[C8] S. Takeyama and S. Ono, "Compressed hyperspectral pansharpening," IEEE International Conference on Image Processing (ICIP), virtual conference, pp. 2855-2859, Oct. 2020.